PLANETS AND PLANETARY NEBULAE: DIFFERENT EVOLUTIONARY PATHWAYS IN THE STELLAR LIFE CYCLE

By

George Vejar

Dissertation

Submitted to the Faculty of the

Graduate School of Vanderbilt University

in partial fulfillment of the requirements

for the degree of

DOCTOR OF PHILOSOPHY

in

ASTROPHYSICS

May 13, 2022

Nashville, Tennessee

Approved:

Keivan G. Stassun, Ph.D.

Simon C. Schuler, Ph.D.

Rodolfo Montez Jr., Ph.D.

Andreas Berlind, Ph.D.

David A. Weintraub, Ph.D.

This work is dedicated to my mother and father,
whose sacrifices allowed me the opportunity to live my dreams,

and

to my wife,
for her continuous support and love through infinity and beyond.

TABLE OF CONTENTS

LIST OF TABLES

LIST OF FIGURES

CHAPTER 1

Introduction

The life cycle of stars throughout the universe is one of creation, transmutation, metamorphosis, death, and replenishment; stars take in material as they are born, change that material, and give back new material when they die. Stars take some of the most basic particles of the universe (protons and neutrons) and create larger elements and situations that allow planets and life to form through various stages of stellar evolution. In this work, I will explore two different stages of a star's life - one of which allowed for multicellular life to develop - and the other is the eventual future of our own Sun.

Not all stars are created equal, as far as we know, groups of stars are born from a distribution of masses given by an initial mass function (Salpeter, 1955; Kroupa, 2001; Chabrier, 2003; Weisz et al., 2015), meaning most newborn stars will have masses similar to or less than that of the Sun while stars with 10 to 100 times the mass of the Sun will come in exponentially fewer numbers. The most massive stars in the universe live the flashiest lives; they are the largest in size, the brightest in luminosity, the hottest in temperature, and have the shortest lifetimes. A star's mass is also a star's fuel, but gravity is the great equalizer. Though massive stars may have more fuel, they also produce stronger gravitational pressure that burns through this fuel at a faster rate producing a brighter star with a shorter lifetime. Most of a star's life is spent in a balance between the crush of gravity and the explosive fusion at its core fueled by the light elements ($Z<26$) the star can fuse. As a star runs out of light elements in the core, fusion stops and gravity attempts to bring all of the matter in the star to a central point. In massive stars, this causes a supernova as the star's outer layers crash and rebound against its core with tremendous force, expelling much of the star's mass back out into space, creating even heavier elements (like gold and uranium), and leaving behind an extremely dense core called a neutron star (the mass of the Sun in a star the size of a city). If the star is massive enough, gravity wins and squeezes the mass into a small enough space that leaves behind a literal hole in space-time: a black hole. This is the life of a massive star; life lasts for tens of millions of years (Corgan et al., 2022) and in the end, it expels most of the fused material back into space which is used to form new stars.

Stars with very little mass run a different course through time. The force of gravity is not strong with these stars so fuel is burned slowly. Light elements are still fused over the course of the star's life, but this life is extended from millions to billions of years. A star with the mass of the Sun will live for 10 billion years (Gustafsson, 1998). Anything with less mass will have an even longer lifetime to the point at which some stars can outlive the current age of the universe itself. These stars, effectively, will never die and never shed their mass like more massive stars. They will continue to fill the expanding void of the universe with dim

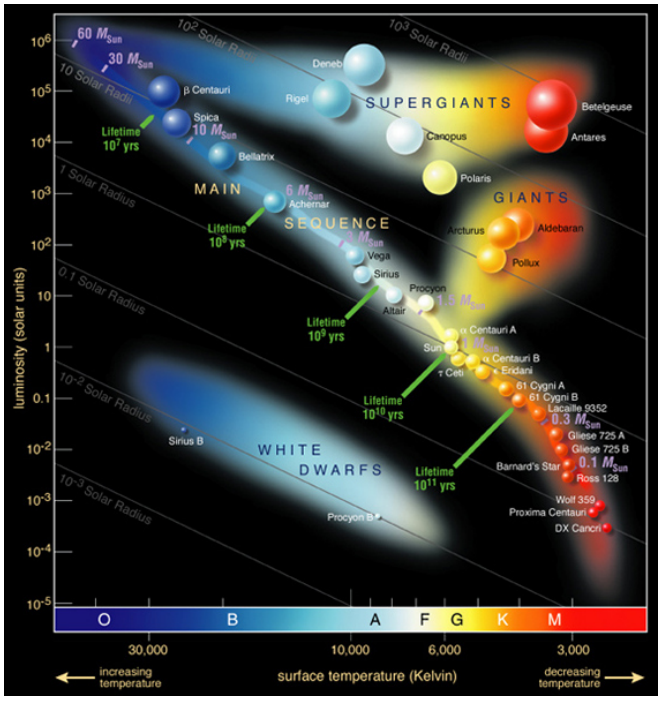

Figure 1.1: The Hertzsprung-Russell (HR) Diagram displays the relationship between luminosity (y-axis) and surface temperature (x-axis) for stars of all masses throughout their life and evolution. Stars are born and live most of their existence fusing hydrogen on the diagonal Main Sequence (MS). Massive stars appear bluer in color and higher up the MS being larger in size, brighter, and hotter. Low mass stars appear redder in color and lower on the MS being smaller in size, dimmer, and cooler. During evolution/death, all stars change their luminosity and temperatures similarly in that they get cooler and brighter moving toward the top right corner of the diagram. Stars with similar masses to the Sun will eventually loop back around to the lower left part of the diagram where they stay as white dwarfs. This image was take from cosmos.esa.int.

reddish light until they are too far away from everything for anyone to detect.

Death is not all dim red light and darkness for Sun-like stars. The Sun falls in a mass range that will go through a full stellar life cycle within the age of the universe, spending most of that time burning hydrogen in its core. During this time, a star is considered to be ”on the Main Sequence,” Main Sequence (MS) referring to the diagonal mass sequence stars fall onto that are born at the same time but with different masses, visible in an HR-diagram (Fig. 2.1). A star burning through the lightest of elements (hydrogen) will remain on the MS until it runs out of hydrogen signaling a change in the stellar interior and the beginning of the end for the star. While on the MS, a star is in equilibrium with gravity - Hydrostatic equilibrium. A delicate balance of hydrogen fusion at the core pushes out against gravity pulling everything in (this is also the case for massive stars) and while the star isn't perturbed or doesn't run out of fuel, the balance remains.

A star's interior from the core to the surface goes from being a very dense, hot, and high pressure plasma to a low density, relatively cool, and low pressure partially ionized gas. The core of the Sun is about 15 million degrees K, whereas the surface is only about 6000 degrees K, a difference of about four orders of

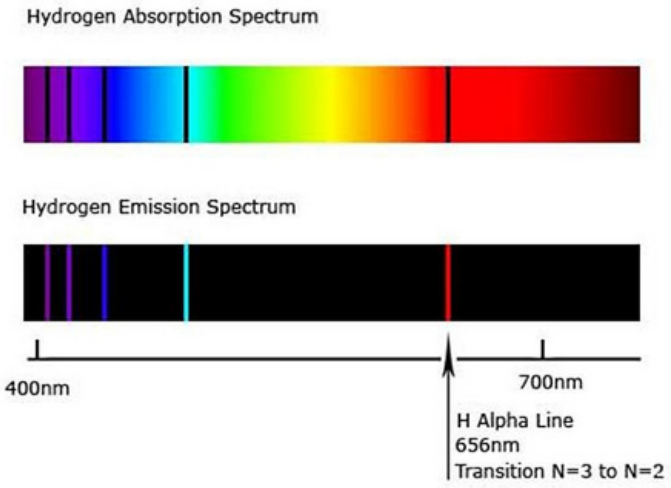

Figure 1.2: An absorption and emission spectrum from the same element; hydrogen. Top: Bright areas show where photons are collected (forming a rainbow in the visible region of the electromagnetic spectrum) and dark lines appear where photons are absorbed by a cool gas. Bottom: Bright lines show which electron transitions (Hα noted) are detected from a hot gas and at what wavelengths, notice the dark background as opposed to the bright background of the absorption spectrum (no photons detected here). This image was taken from khanacademy.org.

magnitude (that's about 10,000 times hotter at the core than the surface). At its core, the star fuses lighter elements into heavier elements producing tremendous amounts of energy which heats and ionizes the star from the inside out. Since the surface is much cooler than the core, this creates a situation where the interior of the star produces a continuous distribution of photon energies (photons of all energies) and the atmosphere (being only partially ionized) of the star is cool enough to absorb some of these photons giving us an absorption spectrum that holds information on the elements present in the stellar atmosphere as seen in Fig. 1.2 with hydrogen. This is because atoms of elements that are not ionized still have their electrons which are considered bound to the atom. These electrons have discrete energy levels where they can exist around the atom which depend on the structure of the nucleus (how many protons and neutrons are present). Different elements, which have their own nuclear structure, have their own energy levels where bound electrons can exist. Each bound electron has a ground state (the lowest energy possible for its nucleus), many possible excited states (specific amounts of energy that the electron can have and still be bound to the nucleus), and some amount of energy that will release the electron from the atom becoming a free electron (when the atom is ionized). A bound electron can jump to an excited state if it absorbs a photon with the exact amount of energy required for the transition (if a bound electron has energy 2eV and can exist in an excited state at 5eV, it can absorb a photon with exactly 3eV of energy to make the transition or it can absorb enough energy to become free but not any energy leaving it between energy levels of its atom). Conversely, an electron in an

excited state can drop down to a lower state or the ground state by giving up energy equal to the difference between the energy states in the form of a photon with that same energy. Because the difference between excited states depends on the structure of the atomic nucleus and each element has a different number of protons (or neutrons), each element can have absorption lines unique to it, like a fingerprint. If an observer knows which lines correspond to which elements, then detecting these lines gives the observer information on the elements present in the star. A deeper analysis can reveal more information about the star such as the amount of an element present or the kinematics of the star's atmosphere.

Stars like the Sun, living for so long in hydrostatic equilibrium, are great environments for multicellular life to have a chance at developing, not on the star itself but on the worlds orbiting the star. Planets will form a few million years after the star forms from the remaining surrounding circumstellar material (Schiller et al., 2015). Gas planets will form out of material in the disk, but rocky-type planets (like the inner planets of our solar system) will mostly form out of heavier elements (refractory elements), diluting these elements in the disk and leaving mostly lighter elements (volatile elements) orbiting the star. The leftover disk gas and dust is cleared out by the planets or falls onto the star, remarkably, leaving behind a measurable difference between refractory and volatile elements in the star's atmosphere. This effect has been found in the Sun when compared to other nearby Sun-like stars without planets (Ramírez et al., 2009; Meléndez et al., 2009). As the planets orbit, they will interact by pulling on one another and on the star itself. Larger planets will have more pull on others than smaller planets and smaller planets will be more susceptible to being pulled, which means larger planets are more likely to survive the early planetary mosh pit. A system with multiple planets can undergo Kozai-Lidov orbital effects (Naoz, 2016), an exchange of orbital angular momentum between orbiting bodies over large timescales that lead to eccentricity and inclination oscillations, causing a planet to be flung out of the system or to fall onto the star. An engulfed rocky planet will also leave a chemical signature on the star as it is preferentially made of refractory elements, increasing the abundances of only those elements found in rocky planets (Schuler et al., 2011c,a; Mack et al., 2014; Mack III et al., 2016; Galarza et al., 2021). Other planets will be shifted around in their orbits ending up either closer or further from the star, a process called orbital migration (Mayor and Queloz, 1995; Lin et al., 1996). All of these planets pull on the star itself in the opposite direction that the star pulls on them, so the star also moves because of each planet (even if only by small amounts). This pull on the star results in a slight Doppler shifting (blue and red shifting) of the star light in the direction of the motion; the radial direction (blue shifted as it moves toward an observer and red shifted as it moves away) called the radial velocity (RV) of the star and can be detected by measuring the shifting of known absorption lines in the stellar absorption spectrum. The RV of a star is directly proportional to the mass of the object (in this case planet) pulling on it, which, if the planet is large enough, is just one way to detect and verify the existence of a planet around another

star. This effect is easiest to detect when the system is observed edge on (the plane of orbit of the planet is in a flat disk where we observe the edge and not the face of the disk). In this configuration, the planet passes directly in front of the star as it orbits, blocking out some tiny fraction of light from the star. The amount of light blocked by the planet is proportional to the size of the planet and by measuring the periodic dip in brightness of the star, an observer can also detect the presence of a planet and measure important properties like the period and size of the planet; this is called the transit method. RVs can give us information on the mass of a planet while transits can tell us the size, two parameters we need to determine the density of the planet which can give us information on the likelihood of a planet to be able to support life. Since planetary systems can be oriented in random directions, not all planets would be detectable using these methods. Other necessary methods include direct imaging (Chauvin et al., 2004; Konopacky et al., 2010; Macintosh et al., 2015; Bohn et al., 2020), microlensing (Bond et al., 2004; Bennett et al., 2006; Bachelet et al., 2012; Gould et al., 2020), astrometry (Sahlmann et al., 2013), transit timing variations (Ballard et al., 2011), and orbital brightness modulation (Charpinet et al., 2011) all of which have their strengths and weaknesses when it comes to detecting planets. And finally, an astute observer can study the chemical signatures on the star possibly left behind by this planetary dance to infer the evolutionary history or presence of planets that may have formed but have not been detected; a method requiring a detailed chemical abundance analysis.

Life, if formed on one of these planets, may persevere for 10 billion years, but it may all be for nought if life does not discover a way to leave its planetary system. A star like the Sun will not go out with a bang, instead its inner layers will contract and heat up as the outer layers swell to an enormous size when hydrogen fusion stops at the core and heavier elements begin to fuse. Layers of larger elements like helium, carbon, oxygen, etc...fuse releasing more and more energy, causing the star to grow tremendously in size and cool in its surface temperature becoming a Red Giant and then an Asymptotic Giant Branch (AGB) star. The asymptotic giant branch is the bright and cool corner of the HR-diagram (Fig. 2.1) where dying stars undergo heavy mass loss of their outer layers ultimately leaving behind a carbon-oxygen degenerate core known as a white dwarf. High stellar winds and ionizing high-energy photons push the outer layers of material away in all directions further expanding the star's material to a size greater than that of the original planetary system. By this time, any planets present would have been engulfed by the outer layers of the expanding star. The star may be technically dead as it is no longer producing energy through fusion but a new celestial object has been born, a Planetary Nebula (PN). This object is characterized by a cloud of low-density material surrounding an extremely hot central star. In the cloud around the star, which is made up of many different elements produced by the star throughout its life and evolution, there are atoms and electrons of those elements moving about. The electrons bound to these atoms will largely be in excited states or be freed by ionizing photons. The cloud will collectively emit photons corresponding to the energy between the excited states of its atoms as

Figure 1.3: The Helix Nebula seen as the composition of several images taken by the Hubble Space Telescope and the Mosaic Camera at Kitt Peak National Observatory. The bright cloud emits photons due to being ionized by the hot (visible) white dwarf at the center. False colors in this image represent emission from different elements found in the cloud; oxygen in blue, hydrogen and nitrogen in red. While the shape appears generally round, the cloud is actually in the shape of a cylinder or tube with the opening pointed directly at the Earth. This image was taken from jpl.nasa.gov.

bound electrons drop in energy or free electrons recombine with ionized atoms creating an emission line spectrum (only specific wavelengths or energies will be released as photons, producing bright emission lines at these wavelengths). This is the opposite of an absorption spectrum, instead of detecting everything but the photons absorbed by the atoms in a gas, those photons that were missing now are the only ones detected. In an absorption spectrum these photons show up as dark lines, because they have been absorbed, but in an emission spectrum they show up as bright lines amongst a dark background and can also be used to determine which elements are present and in what quantities among many other properties. Some of the most prominent emission lines present in PNe are Hα from hydrogen and [OIII], a rare transition from doubly ionized oxygen which are commonly used to identify PNe. Emission lines can make a planetary nebula (PN) about 10,000 times brighter than the star it originated from, making it visible to us even in other galaxies. This can be very useful to determine distances to other galaxies (Ciardullo, 2003; Frew et al., 2016; Gesicki et al., 2018), measuring the kinematics of galaxies (Hurley-Keller and Morrison, 2004; Peng et al., 2004; Merrett et al., 2006; Coccato and Coccato, 2016), and used as tracers of chemical evolution in the Milky Way and other galaxies (Walsh et al., 1997; Richer et al., 1998; Kniazev et al., 2008; Saviane et al., 2009; Magrini and Gonçalves, 2009; Kwitter et al., 2012; Sanders et al., 2012; Cavichia et al., 2017). Unfortunately, PNe are short-lived compared to their lives as a MS star. PNe tend to fade in only 10,000 years (which can still give you such a crick in the neck[1]) as the cloud of material continues to expand away from the white dwarf, ionization becomes less frequent and the atoms stop emitting brightly (Iben, 1995; Jacob et al., 2013). The white dwarf at the center is left to cool for the remainder of time, like a hot potato. These objects are a blink of an eye to the universe, luckily most of the stars in the universe may be Sun-like so finding and studying many of these objects is still a worthy endeavor.

The following chapters in this work cover two different stages of the stellar life cycle. In Chapter 2, I detail theoretical research on the final stages of a Sun-like star's evolution in current and upcoming broad-band surveys. The end of one star is only the beginning of another though as Chapter 3 presents a detailed chemical abundance analysis on stars in the Praesepe Open Cluster in search of evidence of rocky planet formation. Chapter 4 expands on work from Chapter 3 which gives an update to the code, XSpect-EW, used in the chemical abundance analysis. Finally, Chapter 5 takes a look at future prospects for detailed chemical abundance analyses in other Open Clusters.

[1] see the film Aladdin (1992)

CHAPTER 2

Planetary Nebulae and How to Find Them: Color Identification in Big Broadband Surveys

This chapter is based on work published in The Astrophysical Journal, 2019, Volume 879, Article ID 38.

2.1 Abstract

Planetary nebulae (PNe) provide tests of stellar evolution, can serve as tracers of chemical evolution in the Milky Way and other galaxies, and are also used as a calibrator of the cosmological distance ladder. Current and upcoming large scale photometric surveys have the potential to complete the census of PNe in our galaxy and beyond, but it is a challenge to disambiguate partially or fully unresolved PNe from the myriad other sources observed in these surveys. Here we carry out synthetic observations of nebular models to determine *ugrizy* color-color spaces that can successfully identify PNe among billions of other sources. As a primary result we present a grid of synthetic absolute magnitudes for PNe at various stages of their evolution, and we make comparisons with real PNe colors from the Sloan Digital Sky Survey. We find that the $r-i$ versus $g-r$, and the $r-i$ versus $u-g$, color-color diagrams show the greatest promise for cleanly separating PNe from stars, background galaxies, and quasars. Finally, we consider the potential harvest of PNe from upcoming large surveys. For example, for typical progenitor host star masses of $\sim$3 $M_{\odot}$, we find that the Vera Rubin Observatory (VRO) should be sensitive to virtually all PNe in the Magellanic Clouds with extinction up to A_V of $\sim$5 mag; out to the distance of Andromeda, VRO would be sensitive to the youngest PNe (age less than $\sim$6800 yr) and with A_V up to 1 mag.

2.1.1 Introduction

Planetary Nebulae (PNe) are the shells of gas ionized by hot central stars. The PN forms from previously ejected material lost during the asymptotic giant branch (AGB) phase of a low-to-intermediate mass star ($1-8$ $M_{\odot}$). The central star of a planetary nebula (CSPN) plays a key role in the PN characteristics since its fast stellar wind plows into the AGB wind to form the nebula while the CSPN's high surface temperature photoionizes the gas in the newly-formed nebula. A PN will expand and fade over time, while the CSPN rises in temperature, until it eventually cools towards the white dwarf (WD) cooling track (Kwok et al., 1978; Vassiliadis and Wood, 1994; Bloecker, 1995; Miller Bertolami, 2016). Compared to the lifetime of the star, the PN phase is short-lived, remaining visible for only $\sim 10^4$ years (Iben, 1995; Jacob et al., 2013).

For over 60 years the formation process of PNe has been questioned favoring two contending processes. The first consists of a single star in which heavy mass loss occurs during the AGB phase while stellar rotation

and magnetic fields shape the expanding nebula (Gurzadian, 1962; Garcia-Segura et al., 1999; Garcia-Segura et al., 2005; Matt et al., 2004; Blackman, 2004). The second process favors a wide range of interactions between the evolving star and a binary companion for shaping the nebula (Fabian and Hansen, 1979; Soker, 1997; De Marco, 2009). Theoretical and observational considerations suggest that a single AGB star is unlikely to produce a strong enough magnetic field to dramatically shape the nebula, favoring the possibility of binary interactions being mainly responsible for the formation and shaping of non-spherical PN (Soker, 2006; Nordhaus et al., 2007). It is likely that there are still many PNe left undiscovered, as our best estimates place the total number of Galactic PNe anywhere between ~ 6600 and $4.6 \pm 1.3 \times 10^4$, depending on the formation process (De Marco, 2005; Moe and De Marco, 2006).

Naturally, because they represent a specific and short-lived phase of stellar evolution, PNe can be difficult to study but they are important for improving our understanding of late-stage low- to intermediate-mass stars (Iben, 1995; Frew, 2008). PNe that have been found in the Milky Way and in neighboring galaxies have been extremely valuable for a variety of studies. Because of their bright emission lines, PNe are identifiable across the Galaxy and in nearby stellar systems. PNe can be used as tracers of Galaxy kinematics (Hurley-Keller and Morrison, 2004; Peng et al., 2004; Merrett et al., 2006; Coccato and Coccato, 2016); as a rung on the distance ladder via the PN luminosity function (Ciardullo, 2003; Gesicki et al., 2018); and as potential tracers of the chemical evolution of the Milky Way and other galaxies (Walsh et al., 1997; Richer et al., 1998; Kniazev et al., 2008; Saviane et al., 2009; Magrini and Gonçalves, 2009; Kwitter et al., 2012; Sanders et al., 2012; Cavichia et al., 2017).

There is ongoing interest in techniques for readily identifying more PNe efficiently and reliably. A large number of PNe have been discovered through techniques that take advantage of their bright nebular emission lines. Hα surveys such as the SuperCOSMOS Hα Survey (SHS) (Parker et al., 2005; Frew et al., 2014), the INT Photometric Hα Survey (IPHAS) (Drew et al., 2005), and the VST Photometric Hα Survey (VPHAS+) (Drew et al., 2014) have been very successful in identifying Galactic PNe and are cataloged in the Hong Kong/AAO/Strasbourg/Hα (HASH) (Parker et al., 2016) database which contains ~ 3500 objects. Integral field spectroscopy of [OIII] λ5007 has been used to find PNe in crowded areas (Pastorello et al., 2013). Dust can make it difficult for optical surveys to detect PNe but they have also been found in the UKIRT Wide-field Imaging Survey for H_2 survey (UWISH2) through their H_2 emission (Gledhill et al., 2018). More Galactic PNe have recently been discovered through their multi-wavelength characteristics ranging from optical to radio emission (Fragkou et al., 2018).

Large, all-sky surveys, like the Sloan Digital Sky Survey (SDSS) and, in the future, the Vera Rubin Observatory (VRO), can be used to potentially identify thousands of new PN based on broadband photometry where PNe are poorly characterized. Although the observed broadband colors of PNe have been studied

(e.g., in 2MASS and WISE colors Schmeja and Kimeswenger, 2001; Frew and Parker, 2010; Ilkiewicz and Mikołajewska, 2017), and although the theoretically expected broadband colors of PN central stars have previously been calculated (e.g., Weston et al., 2009; Morris and Montez, 2015), the theoretically expected broadband colors of PN nebular emission have yet to be characterized and compared with observations. Existing PNe catalogs are far from complete, and upcoming all-sky photometric surveys have great potential to uncover troves of additional PNe, assuming that it will be possible to efficiently distinguish true PNe from the large numbers of false positives.

We focus on the optical region of the PN spectrum because of the prominent nebular emission lines at these wavelengths. A vast amount of *ugriz*(y) survey data is or will become available through SDSS and VRO, therefore we attempt to characterize PNe in this photometric system. We consider the broadband *ugrizy* characteristics of a synthetic PN as a function of evolutionary age, for both resolved and unresolved PNe. Our methodology for creating our synthetic PN models and calculating the synthesized *ugrizy* observations are presented in §2.2. A grid of broadband absolute magnitudes and the efficacy of different color-color diagrams to reliably identify PNe are provided in §2.3. In §2.4 we compare our results to existing observational SDSS studies and consider future applications with VRO. Finally, §2.5 presents a summary of our conclusions.

2.2 Methodology

In this section, we describe our methodology for creating synthetic broadband *ugrizy* observations of PNe as functions of evolutionary age for both resolved and unresolved PNe. We begin by describing the physical ingredients and assumptions adopted. Because we seek to undertake a more comprehensive study of the broadband behavior of PNe than previously attempted, we intentionally construct our methodology to fully and self-consistently include the effects of both the central star and the nebular evolution. Next we describe the production of the nebular spectra followed by the synthetic *ugrizy* magnitudes and colors from these spectra, and we discuss our treatment of resolved and unresolved PNe. Finally, we include the effects of interstellar reddening for resolved and unresolved spectra.

2.2.1 Planetary Nebula Ingredients

To build our synthetic PN we start with the central star and nebular properties. In particular, throughout this study we work with a 3 $M_{\odot}$ progenitor star, because it is for such a star that nebular evolution models exist to which we can self-consistently couple the evolution of the central star and thereby produce synthetic spectra and colors over the course of the evolution of the star+PN. Figure 2.1 depicts the HR diagram for a 3 $M_{\odot}$ central star evolutionary track from the models of Vassiliadis and Wood (1994); Bloecker (1995), along with 1 $M_{\odot}$ and 5 $M_{\odot}$ progenitor masses for context. The final mass of the white dwarf in this model is 0.605 $M_{\odot}$,

similar to the $\sim$ 0.6 $M_\odot$ mass that is often assumed as a fiducial mass for PN central stars (Perinotto et al., 2004). Thirteen specific age positions on the evolutionary track are indicated, representing the discrete ages that we have chosen to include in our study, spanning the evolution of the system from emergence of the PN to exposing the white dwarf. Figure 2.2 (top panel) indicates the temporal behavior of the CSPN luminosity (L) and temperature ($T_{\rm eff}$) corresponding to these 13 ages.

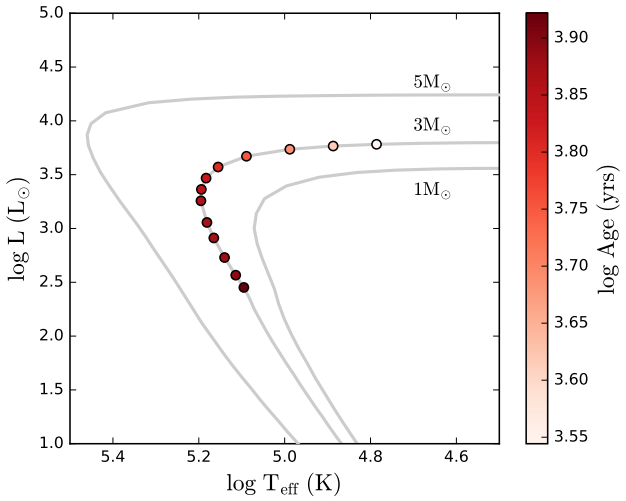

Figure 2.1: Hertzsprung-Russell diagram showing the evolution of the central star for various planetary nebula progenitor masses (gray lines). The points represent luminosity and temperature parameters used for our 13 Cloudy models for a $3M_\odot$ progenitor star. The shading of the color represents the age of the model, refer to Table 2.1 for parameter values.

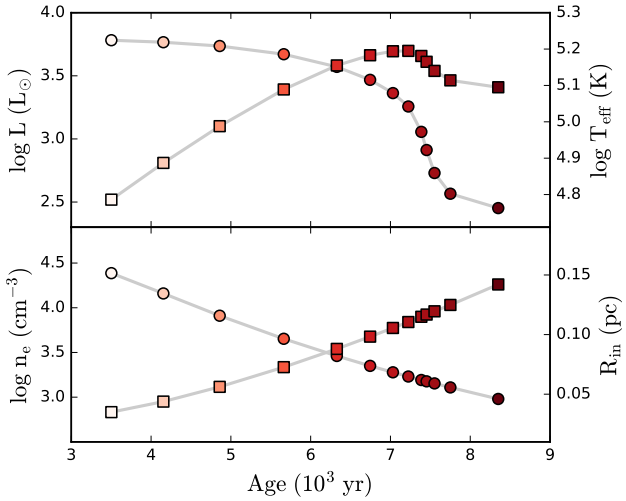

Figure 2.2: (Top panel): Evolution of central star over time; squares correspond to temperature and circles correspond to luminosity. (Bottom panel): Evolution of the nebula over time; squares correspond to the inner radius of the nebula and circles correspond to the electron density. The shading of the color represents the age of the model, refer to Table 2.1 for parameter values.

For every age position on the central star's evolutionary track (Figure 2.1) we require a nebular emission model corresponding to that evolutionary age and with the appropriate central star mass. Fortunately, 1D radiation-hydrodynamics simulations of a PN have been performed by Perinotto et al. (2004); Schönberner et al. (2005). Because those simulations were done for the expansion of a PN illuminated by a central remnant of 0.595 $M_{\odot}$, it is essential to use a central-star evolutionary model that produces a remnant as close to this same final mass as possible. That is why our choice above is of a central star whose final mass is most similar to this value[1], corresponding to a progenitor mass of 3 $M_{\odot}$.

We calculate the nebular size at each time step using a simple approximation based on the Perinotto et al. (2004); Schönberner et al. (2005) nebular model. Based on the radiation-hydrodynamic simulations, the densest part of the nebula is coincident with the inner radius (or rim), $R_{\rm in}$, which follows the relationship $R = R_0 + c(t - t_0)^b$, where $R_0 = 0.031$ pc, $t_0 = 3016$ yrs, $c = 6.7 \times 10^{-7}$ pc yr^{-1}, and $b = 1.4$. For each time step in the evolutionary track, we determine the inner radius ($R_{\rm in}$) based on this prescription. Since the prescription is only applicable for $3016 < t < 10000$ yrs, we only considered the evolutionary track between these ages. As a result, the radii of our synthetic nebula model expands from 0.035 pc to 0.142 pc.

The outer radius $R_{\rm out}$ of the nebula is determined by Cloudy calculations (see next section), specifically by a mass stopping criteria for each model. Phillips (2007) describe an empirical relationship to the total ionized mass, $M_{\rm ionized}$. $M_{\rm ionized}$ increases linearly for $R \leq 0.1$ pc according to $M_{\rm ionized} = M_0(R/0.1\ {\rm pc})$ until reaching a constant total mass, M_0, for $R > 0.1$ pc. In our radiative transfer calculations, we restrict the total ionized mass of the nebula according to this empirical relationship using $M_0 \approx 0.2\ M_{\odot}$. As a result the final mass of our synthetic nebula are designed to closely match the final masses of the ionized nebula described in Phillips (2007). Also as a consequence of this stopping mass criteria the thickness of the nebular shell remains thin, specifically, $(R_{\rm out} - R_{\rm in})/R_{\rm in}$ is always < 0.25.

In addition to the inner radius, for each considered position on the evolutionary track we must calculate the electron density, n_e, of the nebula. Based on the behavior of ~ 240 Galactic and Magellanic PNe, Frew (2008) derived a nebular density relation with nebular radius of $\log n_e = -2.31(\pm 0.04) \log R + 1.02(\pm 0.04)$, where n_e is the electron density of the nebula and R is the nebular radius, in our case $R_{\rm in}$. Figure 2.2 (bottom panel) shows the evolution of n_e and $R_{\rm in}$ over all ages of the nebula.

2.2.2 Cloudy, With a Chance of Photons

The central star and nebular properties described in the previous section are used as input to Cloudy radiative transfer calculations. Cloudy is a plasma simulation software that simulates non-equilibrium gas conditions

[1]The slight discrepancy between the central star final masses of 0.595 $M_{\odot}$ versus 0.605 $M_{\odot}$ in the nebular versus central star evolutionary tracks, respectively, is negligible for compact nebula with radii < 1 pc (Jacob et al., 2013).

to predict an observable spectrum(version 13.03; Ferland et al. (2013)).

In Table 2.1, we list the stellar and nebular ingredients needed to run our Cloudy radiative transfer models. For the nebular composition we use chemical abundances typical of a planetary nebula (see Table 2.2 Ferland et al., 2013; Aller and Czyzak, 1983; Khromov, 1989). We assume spherical geometry for the nebula, a uniform filling factor of unity, and no stopping temperature criteria. Distance between the observer and the nebula is assumed to be 1 kpc. The resulting coarse (R = 200) and high-resolution (R = 2000) spectra at the youngest nebular age considered (3502 yrs, 61,094 K, 6053 $L_{\odot}$) are shown in Figure 2.3 for our region of interest (300 to 1100 nm). The high-resolution spectrum is used for display purposes. Since the high-resolution spectrum does not preserve flux, we use the coarse spectrum for our photometric calculations.

Age (yrs)	log $T_{\star}$ (K)	log $\frac{L_{\star}}{L_{\odot}}$ ($L_{\odot}$)	R_{in} (pc)	log n_e (cm^{-3})	M_{stop} ($M_{\odot}$)
3502	4.786	3.782	0.035	4.386	0.071
4154	4.887	3.766	0.044	4.159	0.088
4860	4.988	3.736	0.056	3.911	0.113
5663	5.089	3.671	0.073	3.652	0.146
6328	5.155	3.571	0.088	3.460	0.178
6745	5.183	3.468	0.098	3.349	0.199
7031	5.194	3.363	0.106	3.277	0.201
7224	5.195	3.257	0.111	3.230	0.201
7387	5.181	3.056	0.115	3.192	0.202
7453	5.165	2.912	0.117	3.176	0.202
7552	5.140	2.73	0.119	3.153	0.203
7751	5.114	2.566	0.125	3.108	0.202
8351	5.095	2.452	0.142	2.980	0.202

Table 2.1: Parameters used for the 13 Cloudy models that change from model to model. These parameters represent the evolution of the central star ($T_{\star}$, $L_{\star}$) and nebula (R_{in}, n_e) while M_{stop} is used to stop the simulation once the nebula has accumulated enough mass.

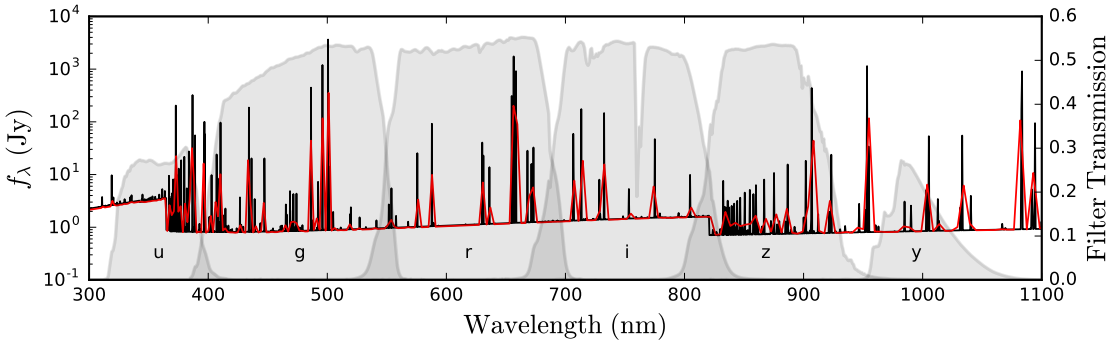

Figure 2.3: Coarse (standard) resolution spectrum of the youngest model age = 3502 yrs as output by Cloudy ($T_{\star} = 61,094$ K, $L_{\star} = 6053\ L_{\odot}$) (red) along with the high resolution spectrum for the same model (black). The coarse spectrum is used for calculating the magnitudes in each filter. Overlaid in gray is a representative *ugrizy* VRO filter set (described in the text). Note that the *y* filter is not used in this study.

Atom	[X/H] (dex)
H	0.0000
He	-1.0000
C	-3.1079
N	-3.7447
O	-3.3565
F	-6.5229
Ne	-3.9586
Na	-5.7212
Mg	-5.7959
Al	-6.5686
Si	-5.0000
P	-6.6990
S	-5.0000
Cl	-6.7696
Ar	-5.5686
K	-6.9208
Ca	-7.9208
Fe	-6.3010
Ni	-7.7447

Table 2.2: Abundances used for PN models within Cloudy (Aller and Czyzak, 1983; Khromov, 1989). Values are relative to solar values from Grevesse and Sauval (1998), Holweger (2001), Allende Prieto et al. (2001, 2002). Elements not mentioned are assumed to be depleted enough to be of no consequence. For more information on available abundances within Cloudy refer to *"Hazy"* the Cloudy manual (Ferland et al., 2013).

2.2.3 Synthesizing Broadband Photometric Observations

We consider observations of our synthetic nebulae performed with a standard *ugrizy* photometric system[2]. The set of photometric filters cover wavelengths between 320 nm and 1080 nm and their properties are provided in Table 2.3 with their transmission curves shown in Figure 2.3. The filter transmission curve is interpolated onto the wavelength grid of the coarse resolution Cloudy spectra described in §2.2.2. For each age of our synthetic nebula we convolved the nebular and central star flux spectra with the filter transmission curves. Then we normalized the resulting flux to the AB magnitude system to determine the *ugrizy* magnitudes. We scaled these magnitudes to 10 pc to determine the absolute magnitudes, which are presented in Table 2.4.

2.2.4 Accounting for Spatially Resolved Extended Emission

The extended nature of a PN requires additional consideration. For aperature photometry, when the nebula and central star are resolved only a fraction of the nebular flux will be measured. To understand the impact of resolved nebula and central stars, we constructed a toy model of the synthetic nebulae. For each stage,

[2]We used the VRO filters as defined on 2016-12-07 obtained from the Spanish Virtual Observatory (SVO) Filter Profile Service. The *y* filter is shown for completeness but is not used in this study.

Filter	Range (nm)	$\lambda_{\rm eff}$ (nm)	$W_{\rm eff}$ (nm)	m_{sat} (mags)	$m_{5\sigma}$ (mags)
u	320–400	373.2	54.6	14.7	23.9
g	400–552	473.0	133.2	15.7	25.0
r	552–691	613.8	133.7	15.8	24.7
i	691–818	748.7	832.5	15.8	24.0
z	818–922	866.8	937.5	15.3	23.3
y^a	950–1080	967.6	81.0	13.9	22.1

Table 2.3: Properties of the *ugrizy* filter set used in our analysis. All magnitudes are normalized to the AB magnitude system (Oke and Gunn, 1983).

[a]Not used in this study

we assumed a three-dimensional spherical shell with the radius, thickness, and density used in our synthetic nebulae. We projected this shell onto the plane of the sky. Assuming aperture photometry, we considered a range of aperture diameters on the sky, $\Omega_{\rm aperture}$, and nebular diameter on the sky, $\Omega_{\rm neb}$. For a range of aperture to nebular diameter ratios, $\Omega_{\rm aperture}/\Omega_{\rm neb}$, we calculated the fraction of nebular emission, $f_{\rm neb}$, that is measured by the aperture. We recalculated the magnitudes after scaling the nebular flux by this fraction and adding it to the central star flux. We consider models with the same nebular fraction as a fractional variant and label them with roman numerals in increasing order as $f_{\rm neb}$ decreases.

This method of estimating resolved nebular magnitudes provides the most flexibility with regards to survey resolution characteristics. Note that because in reality a given PN, at a given distance, will evolve in its apparent angular size, it will not in general evolve along a single variant "track". Rather, the collection of variant tracks represent the overall parameter space through which individual PNe may evolve, for a range of distances, photometric apertures, and states of evolution.

2.2.5 Reddening

Intervening dust poses a serious problem for observing and identifying objects with photometric colors. The dust will dim (extinction) and redden an object which can limit the distance at which an object can be detected and change its position in a color-color diagram. To determine the reddening vector in the ugrizy system, we applied the reddening curve of Cardelli et al. (1989) to all ages of the synthetic nebular spectra then calculated the reddened magnitudes. Figure 2.4 shows how varying levels of extinction (A_V) can affect the spectrum of a PN. Figures 2.5 and 2.6 show the reddening vector that all 13 models would follow with $A_V = 1$ mag.

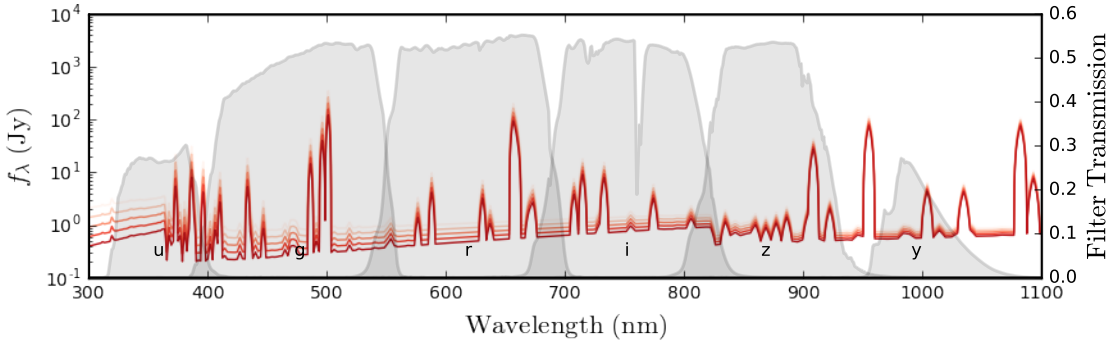

Figure 2.4: Youngest model age = 3502 yrs ($T_\star = 61,094$ K, $L_\star = 6053\ L_\odot$) spectrum shown with varying levels of extinction (A_V) along with the VRO filter set. Lines are shaded lightest to darkest for $A_V = 0,\ 0.25,\ 0.5,\ 0.75,\ 1.0$.

2.3 Results

In this section, we present the main results of our study. First, we provide a grid of synthetic *ugrizy* photometry representing our model PN at different evolutionary ages and different observed angular sizes. Second, we describe the evolution of prominent emission lines in each filter and their effect on the calculated magnitudes. We then identify the *ugrizy* color-color spaces that are most effective at differentiating PNe from other celestial objects.

2.3.1 Synthesized Nebula Absolute Magnitudes

A key result of this study is the collection of the absolute magnitudes for our synthetic nebulae in the *ugrizy* photometric system (see Table 2.4, Table 2.5 and Figure 2.5 for all variants). These absolute magnitudes span $\sim$ 4800 years of PN evolution for a 3 $M_\odot$ progenitor star evolving into a 0.605 $M_\odot$ white dwarf. The contributions from continuum and line emission dictate the behavior of the broad band magnitudes as a function of age. In each band, the continuum drops by about an order of magnitude as the models approach older stages resulting in the overall decline in the broadband magnitudes as the nebula evolves. We do not display variants beyond VII, as variants VIII–X become too faint to be practical.

The line emission as a function of age in each band is often dictated by one or two species that dominate a given bandpass. In the *u* band, the prominent emission lines are: [Ne III] (λ3869, λ3968), [O II] (λ3726, λ3729), H II (λ3835, λ3889, λ3970), and H III (λ3203). In the *g* band, the prominent emission lines are: [O III] (λ5007, λ4959), H I (H_β λ4861, H_γ λ4340, H_δ λ4102), H II (λ4686), He I (λ4471), [S II] (λ4074, λ4070, λ4078), and N I (λ5200, λ5198). In the *r* band, the prominent emission lines are: H I (H_α λ6563), [N II] (λ6584, λ6548), He I (λ5876), [S II] (λ6720, λ6731, λ6716), S III (λ6312), [Cl III] (λ5538) and [O I] (λ6300). In the *i* band, the prominent emission lines are: [Ar III] (λ7135, λ7751), [O II] (λ7323, λ7332),

Variant I:	$\Omega_{\rm aperture}/\Omega_{\rm neb} = 1.3$				f_{neb} = 1	
Age (yrs)	*u* (mags)	*g* (mags)	*r* (mags)	*i* (mags)	*z* (mags)	*y* (mags)
3502	-2.59	-3.63	-3.38	-2.20	-2.18	-2.09
4154	-2.70	-3.91	-3.47	-2.21	-2.20	-2.15
4860	-2.46	-3.94	-2.98	-1.87	-1.98	-1.94
5663	-2.11	-3.66	-2.53	-1.44	-1.62	-1.66
6328	-1.93	-3.41	-2.36	-1.21	-1.40	-1.49
6745	-1.95	-3.23	-2.43	-1.14	-1.29	-1.39
7031	-1.98	-3.00	-2.53	-1.06	-1.13	-1.28
7224	-2.00	-2.72	-2.64	-0.98	-0.98	-1.21
7387	-1.71	-2.10	-2.49	-0.63	-0.54	-0.95
7453	-1.44	-1.60	-2.27	-0.33	-0.18	-0.72
7552	-1.09	-0.90	-1.98	0.08	0.28	-0.45
7751	-0.75	-0.22	-1.68	0.45	0.71	-0.24
8351	-0.51	0.24	-1.46	0.73	1.00	-0.11

Table 2.4: Predicted absolute magnitudes of our synthetic nebular spectra for the *ugrizy* filter set. No extinction is applied. Models are fully unresolved with $\Omega_{\rm aperture}/\Omega_{\rm neb} = 1.3$ and $f_{neb} = 1$. For varying $\Omega_{\rm aperture}/\Omega_{\rm neb}$ and f_{neb} values see Table 2.5.

He I (λ7065), and Cl IV (λ8047). Fluxes from the aforementioned lines exhibit three common behaviors: (1) *decreasing* throughout the evolution, (2) *double-peaked* with an initial rise, a decrease, then another rise as the CSPN $T_{\rm eff}$ approaches its hottest temperature before decreasing again as $T_{\rm eff}$ cools, and, (3) *single-peak* with a steady increase in flux as the as CSPN $T_{\rm eff}$ approaches its hottest temperature before decreasing as $T_{\rm eff}$ cools. Lines with decreasing behavior are: [Ne III], H I, [O III], He I, S III, [Cl III], Cl IV, [Ar III]. Lines with a double peak behavior are: [O II], [S II], N I, [N II], [O I]. Only H II lines show a single peak behavior. These behaviors of the line emission are due to the ionization and physical parameters (radius and density) of the modeled nebula.

When convolved with the bandpass transmission curves the broadband magnitudes can mimic the age-related behavior of the strongest emission lines. The *u* band magnitude behavior is double-peaked with a steady decrease largely influenced by the [O II] emission and the overall decreasing flux from the other lines in this bandpass. The [Ne III] lines are very close to the edge of the *u* filter bandpass, where the transmission is reduced, therefore, despite being the most prominent line in the *u* band, [Ne III] does not contribute as much flux as the [O II] lines. The *g* band magnitude exhibits decreasing behavior and is largely influenced by [O III]. The *r* band magnitude is double-peaked, which is the result of the H I emission dominating at earlier ages ($t_{\rm age} < 7000$ yr) until [N II] begins to dominate. The *i* band magnitude decreases according to the evolution of [Ar III] with some influence from [O II].

In the CMDs (Figure 2.5) there exists a hook feature before the eighth model ($t_{\rm age} \leq 7224$ yrs) (also somewhat visible in the CCDs) due to the evolution of these lines. Once the models have reached the empirically

observed maximum mass we imposed (at the eighth model $t_{\rm age} = 7224$ yrs) they become matter bounded and transparent to ionizing radiation resulting in a somewhat steady decline in brightness and color evolution.

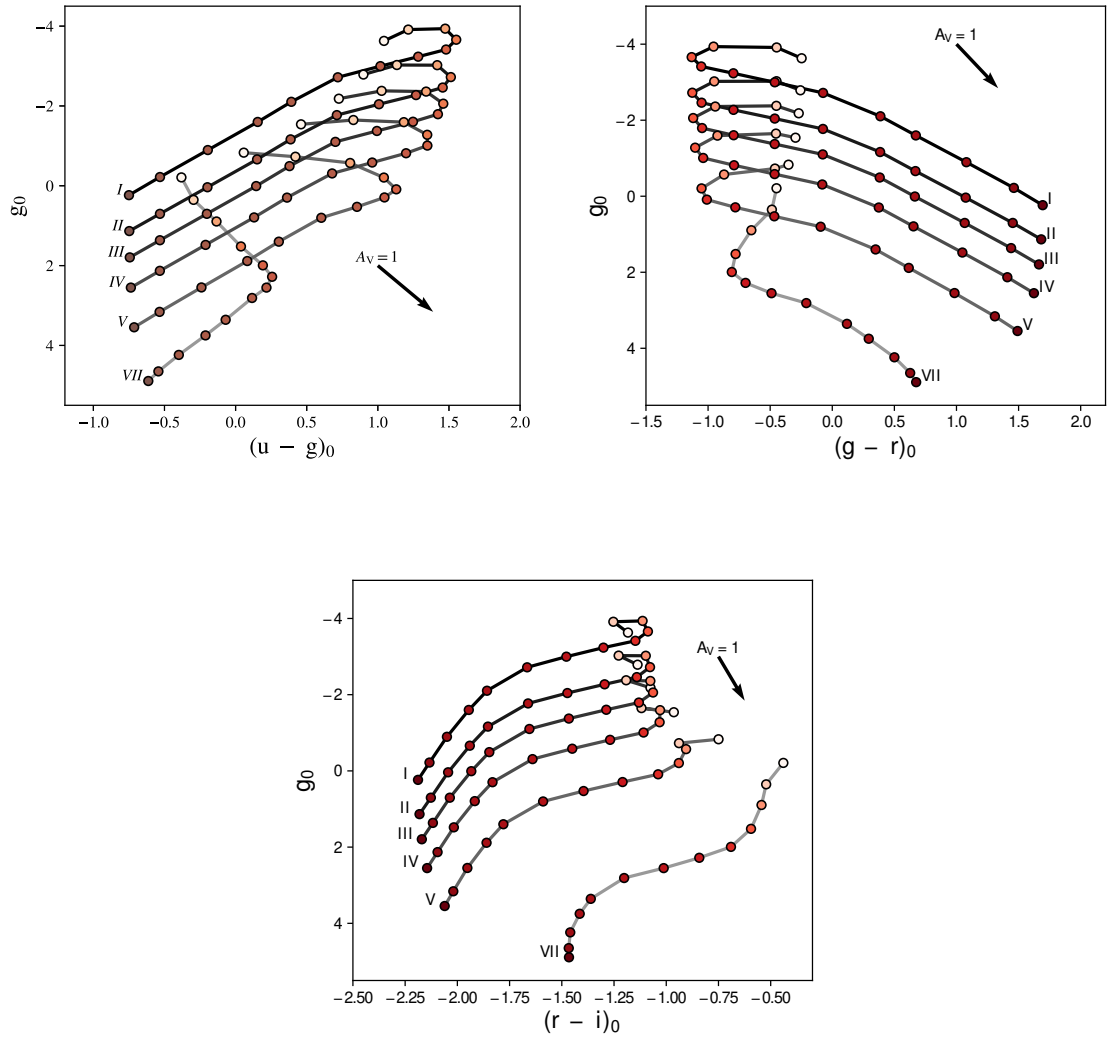

Figure 2.5: Selected color-magnitude diagrams for PN models. Points are colored similarly to Figure 2.1. Grey-scaled shaded lines connect models of the same $f_{\rm neb}$ as indicated by the Roman numeral variant labels. A black line connects unresolved models, the shade lightens as $f_{\rm neb}$ decreases (see Table 2.5 for values of each variant).

The absolute magnitudes given in Table 2.4 are only valid for the total integrated flux from a PN. When a PN is resolved, only a fraction of the nebula will be observed, thus reducing the nebular contribution. This effect changes the measured flux in each filter and the measured color for any two filters. Figures 2.5, 2.6, and 2.8 show how magnitudes and colors change as the aperture encloses less of the nebula.

2.3.2 Identifying PNe in *ugrizy* Color-Color Diagrams

We compare our PN models and variants to SDSS objects in Figure 2.6. Contours of stars, galaxies, and quasars are used to illustrate their locations in the various diagrams. Data for these object types come from SDSS DR7 (Abazajian et al., 2009) and were queried using the SDSS SkyServer. We only included objects with SDSS spectroscopic observations to allow for further filtering on z for the star, galaxy, and quasar object types.

The top left panel of Figure 2.6 shows the $r-i$ vs $g-r$ color-color diagram. Here, models occupy a separated space from the SDSS data with $r-i$ between 0 and -2.5 and $g-r$ between $\sim$1.75 and -1.5. The unresolved synthetic nebular models (variant I), as well as the oldest resolved models (variants VI through IX) remain separated from stars, quasars, and galaxies through out all or most stages of evolution in this diagram for $r-i<-0.75$. (We do not show variants II–V as these are effectively equivalent to variant I.) As the central star and nebula are resolved, the colors converge towards the locus of blue evolved stars, as expected. Similarly, the bottom panel of Figure 2.6 shows that our models are also separated from most of the SDSS data in the $r-i$ vs $u-g$ color-color diagram for $r-i<-0.75$. These two diagrams will be essential in identifying new PN candidates of all ages.

In the top right panel of Figure 2.6, the PN models occupy the left region of the diagram. They fall between values of $\sim$1.75 to -1.5 in $g-r$ and $\sim$1.6 to -1.0 in $u-g$. Our synthetic nebulae cross through the loci of early-type MS stars, quasars, and blue evolved stars in this diagram. The youngest ($t_{\rm age}<7000$ yrs) and oldest ($t_{\rm age}>7500$ yrs) stages in our fully unresolved models (variant I) are somewhat separated from these loci making these areas good places to look for young and old unresolved PN candidates. The change in color values for all CCDs is a result of the nebular emission as seen in Figure 2.5 and is described in the previous section.

2.4 Discussion

2.4.1 Comparison to Prior Work

A number of studies have shown that emission line objects like PNe can be identified or characterized by broadband filters. In the UV, optical, and near-infrared (NIR) Veyette et al. (2014) used Hubble Space Telescope (HST) Advanced Camera for Surveys and the Panchromatic Hubble Andromeda Treasury (PHAT) survey data to identify broadband detections of known PNe and were able to roughly estimate the excitation classifications of groups of PNe with the addition of archival $m5007$ narrow-band magnitudes. In the optical, Kniazev et al. (2014) used the Sloan Digital Sky Survey (SDSS) colors to separate PNe from other point sources in the outskirts of M31. Parker et al. (2016) developed a method using mid-infrared colors to identify Galactic PN candidates using available data in the Galactic Legacy Infrared Mid-Plane Survey

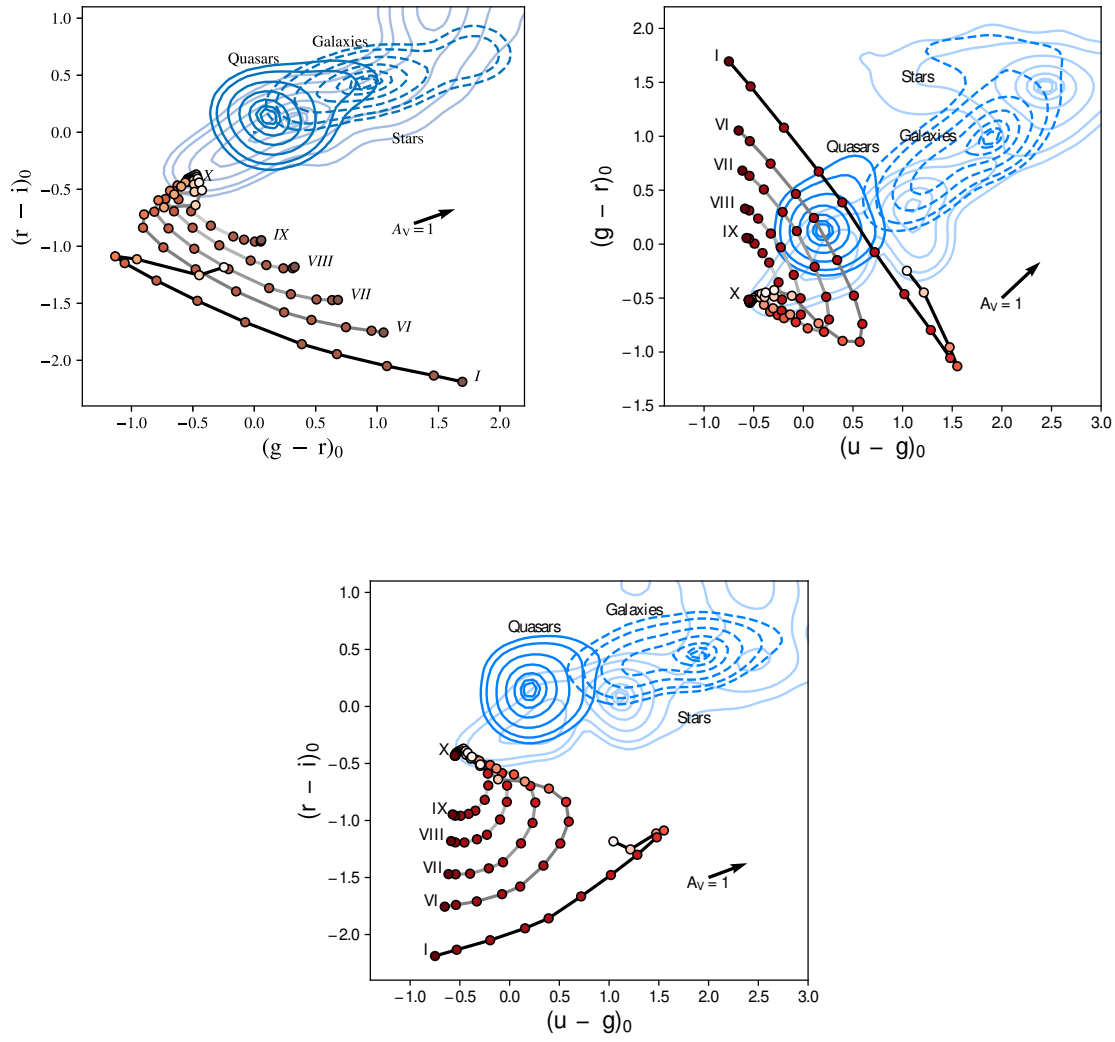

Figure 2.6: Selected color-color diagrams for PN models along with distributions of point sources from SDSS. Points and grey-scaled lines are described in Figure 2.5. Distributions of SDSS objects have been smoothed with a Gaussian filter with a $\sigma = 0.13$ mag. The contour levels indicate 5, 10, 25, 50, 75, 90, and 95% of the maximum value of the smoothed distributions.

Extraordinaire I (GLIMPSE I) point source archive. Data from the Infrared Astronomical Satellite (IRAS) was used to inform optical spectroscopic follow-up by Suárez et al. (2006) to confirm PNe candidates along with post-AGB stars and sources transitioning from AGB to PN stages of evolution. Corradi et al. (2008) and following papers in the series (Corradi et al., 2010; Rodríguez-Flores et al., 2014) describe a similar method for selecting symbiotic star candidates using the INT Photometric Hα Survey (IPHAS) and the Two Micron All Sky Survey (2MASS) colors showing that symbiotic stars can be distinguished from PNe through colors but ultimately spectroscopic follow-up is necessary for verification.

We compare our predicted PNe colors and magnitudes (for variant I) to confirmed PNe in M31 (Kniazev et al., 2014). Kniazev et al. (2014) used 29 known PNe in M31 (Jacoby and Ford, 1986; Nolthenius and Ford, 1987) to construct magnitude and color criteria to identify additional PNe with SDSS photometry. 70 were confirmed to be PNe through follow-up spectroscopy (Kniazev et al., 2014). In Figure 2.7 the color-magnitude and color-color diagrams presented in Kniazev et al. (2014) are reproduced along with some of their selection criteria. We queried SDSS (DR14; Abolfathi et al., 2018) for clean sources within 1 degree of M31 and with point source criteria outlined in Kniazev et al. (2014). The spectroscopically verified PNe from Nolthenius and Ford (1987) along with our 3 $M_{\odot}$ PN evolutionary models scaled to the distance of M31 (760 kpc; van den Bergh, 1999) are overlaid onto the CMD and CCD. At such a distance, all of our nebular models are unresolved. In the CMD, the sample identified by Kniazev et al. (2014) is consistent with the youngest stages of our PN models ($t_{\rm age} < 7300$ years). We find similar consistency in the CCD, except for youngest stage ($t_{\rm age} \sim 4200$ years), which is outside of the $(g - r \geq -0.4)$ color cut used by Kniazev et al. (2014) to reduce contamination from high redshift objects. As suggested by our PN models, this color cut will limit the identification of the youngest and oldest PNe in M31, however, these PNe might be present and identifiable using the CCD.

We also compared our results for resolved and unresolved colors and magnitudes to six faint PNe (PN G094.0+27.4, PN G211.4+18.4, PN G049.3+88.1, PN G025.3+40.8, PN G047.0+42.4, and PN G158.8+37.1) recovered by Yuan and Liu (2013) through identification of excess [OIII] λ5007 or [OIII] λ4959 emission in the SDSS spectra of objects who's photometry was affected by the nebula. For each PN, we used the object's coordinates to obtain an SDSS g band image of the region (DR14; Abolfathi et al., 2018) and visually identified the PN in the image (using ds9). We then visually located the closest object to the CS position of the PN and obtained the SDSS ugriz magnitudes of that source. In Figure 2.8 we compare the colors of these six sources in relation to our models. The colors for PN G094.0+27.4, PN G211.4+18.4, PN G047.0+42.4, and PN G158.8+37.1 are consistent with that expected from a central star with very little nebular emission as they appear close to our model variants VIII-X (marked as stars in Figure 2.8). The nebular radii of these three objects are $> 90''$, which is much larger than the typical $\sim 1''$ seeing resolution limit of SDSS, hence only a small fraction of the nebular emission is detected in these objects. PN G025.3+40.8 (marked as a triangle in Figure 2.8), with a nebular radius of $13''$, is consistent with a higher fraction of nebular flux detected as it appears near our variant VI models indicating a fractional nebular flux of $\sim 9 \times 10^{-3}$ was observed with the CS. PN G049.3+88.1 (marked as a circle in Figure 2.8), with a nebular radius of $2\farcs7$, is consistent with nearly all of the nebular flux detected as it appears near our variant I models. While this is not a rigorous comparison of these sources to our models, generally, we see that CSPNe with a larger sized nebula contain less nebular flux than CSPNe with a smaller sized nebula as predicted by our models.

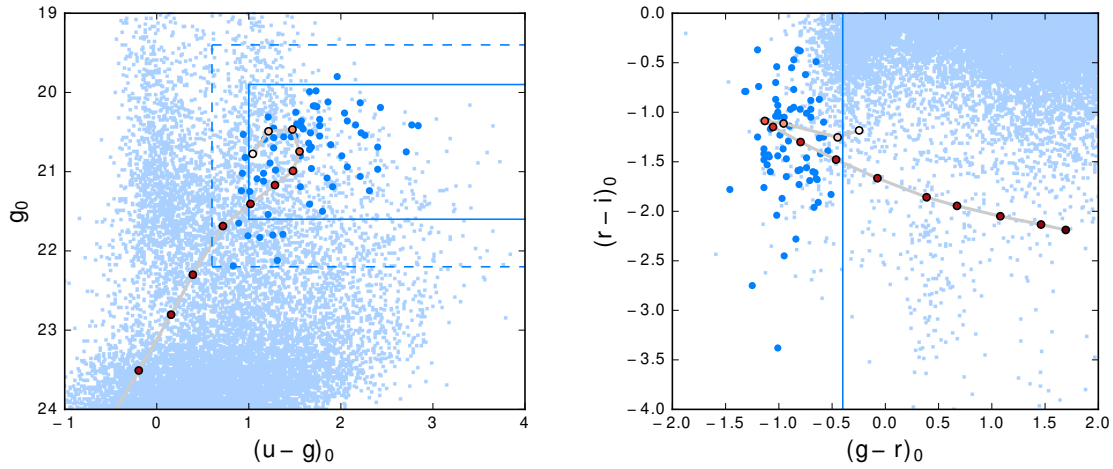

Figure 2.7: 70 confirmed PNe, in dark blue, detected at the outskirts of the Andromeda galaxy (M31) as point sources by SDSS (Kniazev et al., 2014). PNe models are colored similarly to Figure 2.1. Left panel shows some of the color cuts used by Kniazev et al. (2014) as solid and dashed lines at $(u-g)_0 \geq 1.0$ mags and 0.6 mags, $19.9 \geq g_0 \leq 21.6$ mags and $19.4 \geq g_0 \leq 22.4$ mags. Right panel shows a color-magnitude diagram of the same objects with solid line showing the $(g-r \geq -0.4)$ color cut. SDSS stars near M31 are shown in light blue.

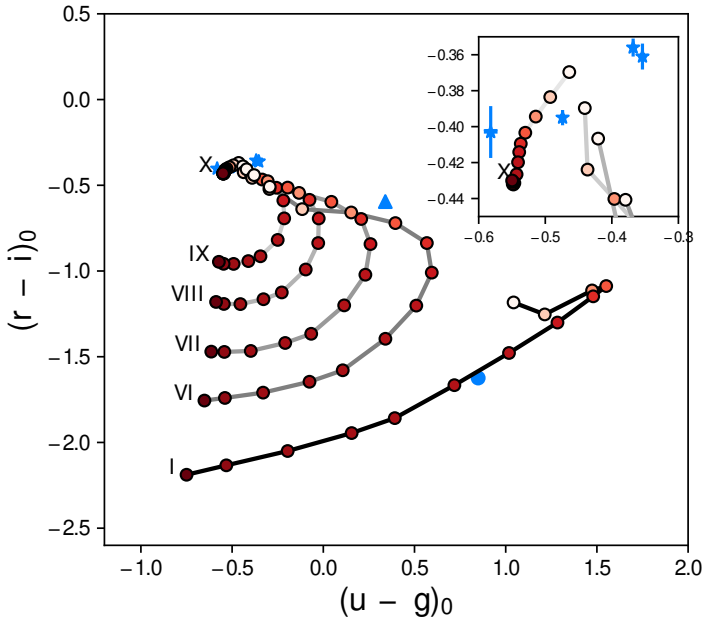

Figure 2.8: Color-color diagram showing PNe models and relevant variants. Red points connected with grey-scaled lines are described in Figure 2.5. Blue points of different marker types are faint PNe from Yuan and Liu (2013), color values are from SDSS and include error bars. Blue marker's correspond to different PNe sizes; circle $\leq 3\farcs0$, $3\farcs0 <$ triangle $< 20\farcs0$, stars $\geq 20\farcs0$. Variants labeled with higher numerals contain less nebular emission, representing resolved PNe. Inset plot shows region near variant X for clarity.

2.4.2 Applications to Upcoming Surveys

Upcoming surveys such as VRO can potentially greatly expand the number of known PNe at different stages of evolution, both within the Milky Way and in other nearby galaxies. As an example, other authors have estimated VRO's distance limit for RR Lyrae variables to be 400 kpc (LSST Science Collaboration et al., 2009); VRO's potential reach for PNe may also be similarly impressive. VRO will commence operations in 2023 and is scheduled to be a 10-year long survey of the southern sky aiming at addressing questions from scales of the solar system to dark energy. The telescope harbors an 8.4 meter mirror and a 3200 megapixel camera that will image 37 billion stars and galaxies. The camera is equipped with the *ugrizy* filter set with sensitivity information detailed in Table 2.3.

The first consideration for VRO's reach of PNe is spatial resolution of PNe flux. The optimal seeing limit for VRO is projected to be $\sim 0\farcs7$ (LSST Science Collaboration et al., 2009), if we take this as an estimate of the size of aperture ($\Omega_{\rm VRO}$), then for any $\Omega_{\rm neb} > \Omega_{\rm VRO}$ the nebula will potentially be resolved. In Figure 2.9, we calculate the ratio $\Omega_{\rm VRO}/\Omega_{\rm neb}$ for a range of distances and include the locations of our synthetic nebular models shown in Figures 2.5 and 2.6. At a distance to the Magellanic Clouds (49.97 and 62.1 kpc; Pietrzyński et al., 2013; Graczyk et al., 2014) young models ($t_{\rm age} < 6300$ yrs) are unresolved while older models are marginally resolved. For our oldest models ($t_{\rm age} > 6300$ yrs) the nebular diameters are $\sim 1\farcs0$. With worse seeing or by utilizing a slightly adjustable aperture in the imaging analysis, it is possible to observe all the nebular flux for marginally-resolved cases.

The reach for a given survey is also dependent on the survey saturation and limiting magnitudes (see Table 2.3; LSST Science Collaboration et al., 2009), as well as extinction to the source. Using Table 2.4, it is possible to study unresolved nebular fluxes for specific combinations of distance and extinction to determine the reach for VRO. Because the identification of potential PNe requires detection in at least three filters (*g*, *r*, and *i*) we considered the saturation and 5σ limiting magnitudes, $m_{\rm sat}$ and $m_{5\sigma}$, respectively, for these three filters. In Figure 2.10, we determined the VRO detection limit for our unresolved nebular models as a function of distance and extinction. For modest extinction values ($A_{\rm V} < 5$ mag) at the LMC/SMC, all of our nebular models predict detectable emission in *g*, *r*, and *i*, however, we potentially reach the saturation limit in *g* and *r*, for our youngest models when extinction drops below 1 mag (see Figure 2.10). For another example, if VRO observed a system like Andromeda (M31) at a distance of 760 kpc (van den Bergh, 1999), in the areas of low extinction ($A_{\rm V} \lesssim 2$ mag), similar to those found in the outskirts of that galaxy (Kniazev et al., 2014; Dalcanton et al., 2015), the youngest nebular models can be detected in these three bands, but fewer of the older nebular models would be detected in *i* ($t_{\rm age} > 7300$ yrs). Hence, surveys like VRO can be used to discover many new potential PNe beyond our galaxy.

We can also consider VRO's reach for PNe specifically within the Milky Way. Here, estimating the reach is further complicated by the numerous combinations of nebular age/size, distance, and extinction. The contribution of the nebular flux to the aperture is a strong function of $\Omega_{\rm VRO}/\Omega_{\rm neb}$ (see Figure 2.5). To consider the reach within the Milky Way, we provide variants of the absolute magnitudes in Table 2.5 for a range of $\Omega_{\rm VRO}/\Omega_{\rm neb}$. For example, we considered the distance-$A_{\rm V}$ based reach for VRO at a distance consistent with the Galactic center (8.3 kpc; Majaess et al., 2018). Young PNe ($t_{\rm age} \approx 3500$ yr, $r_{\rm neb} \sim 0.035$ pc) will be resolved at the Galactic center with only $\sim$1.6% of the nebular emission measured by a 0.″7 aperture ($\Omega_{\rm VRO}/\Omega_{\rm neb} = 0.075$). As a result, such a PN would be detectable in g, r, and i for lines of sight where $A_{\rm V} < 10$ mags. However, for lines of sight where $A_{\rm V}$ drops below 2 mags, the model-predicted flux would reach the saturation limits. For older models ($t_{\rm age} > 6300$ yrs) at the distance of the Galactic center, since the nebula grows in size, the nebular flux contribution reduces further. For these older models, saturation is unlikely with A_V serving as the only limit on detection with maximum line of sight A_V values in the range of $5-10$ mags.

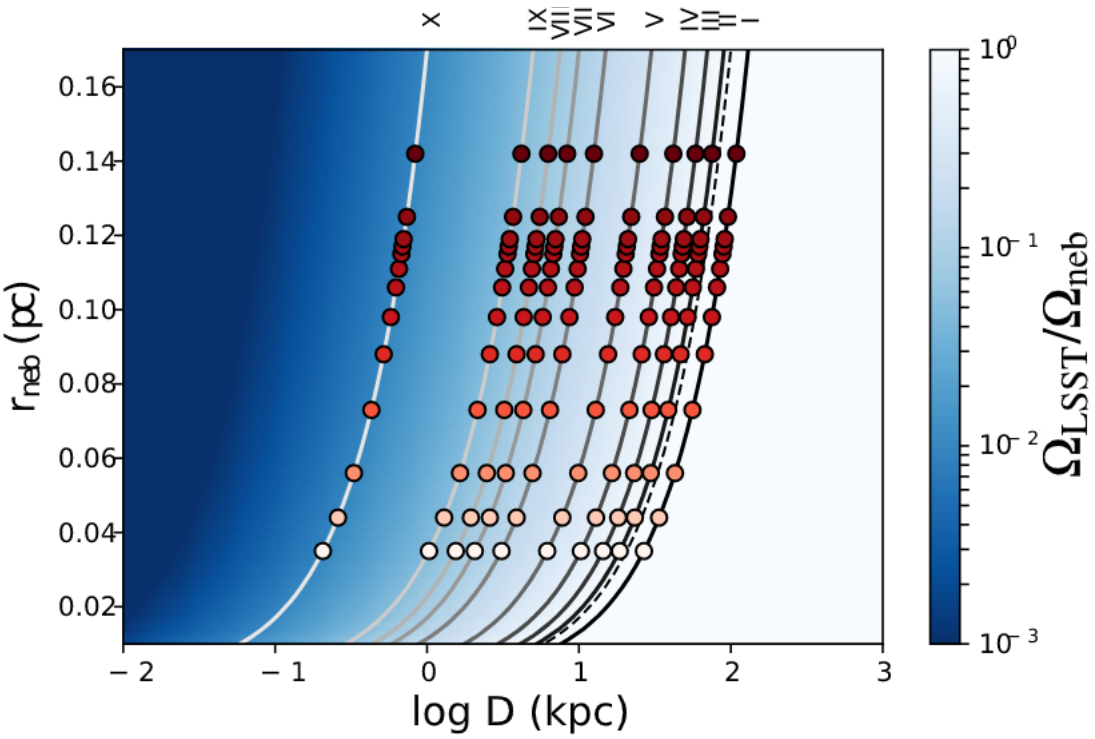

Figure 2.9: $\Omega_{\rm LSST} = \Omega_{\rm VRO}$. PNe model radius (pc) versus PNe distance is shown, along with the degree to which the PN is resolved by the nominal VRO seeing (0.″7) relative to the PN radius ($\Omega_{\rm VRO}/\Omega_{\rm neb}$) in the blue shading. Points and grey-scaled lines are described in Figure 2.5, Roman numerals label fractional variants. The point where VRO begins to resolve the PNe, $\Omega_{\rm VRO}/\Omega_{\rm neb} = 1$, falls between variants I and II (dashed line). PNe at larger distances or with smaller radii will be unresolved to VRO; PNe at smaller distances or larger radii will be resolved to a degree depending on these factors.

2.4.3 Limitations of the Current work

The methodology and results presented in this work demonstrate the potential of using synthetic optical PNe spectra and a set of filters to produce accurate magnitudes and colors. However, we have only considered the evolutionary track for a 3 $M_{\odot}$ progenitor with chemical abundances similar to those of Galactic PNe. Constructing these models for a range of progenitor masses will give a better understanding of the distribution of PNe in color-color space and their identification in future surveys.

In developing our methodology, we discovered that a crucial ingredient to construct accurate models is the hydrodynamical expansion over time of the nebular radius as the central star evolves. In particular, self-consistent radiation-hydrodynamic models of a PN (e.g., Jacob et al., 2013; Schönberner et al., 2005; Toalá and Arthur, 2014) are important ingredients necessary to track to evolutionary behavior of the nebula and its radiation.

As mentioned in section 2.4, this method can only identify PNe candidates. All potential PNe candidates will require supporting spectroscopic or narrowband observations to verify their nature. This is also necessary to distinguish true PNe from other emission line objects such as Wolf-Rayet (WR) stars, HII regions, symbiotic stars, and CVs which may contaminate the same color-color space.

Finally, our study highlights an immediate outcome and discovery space made possible by a survey like VRO. We have not carefully considered the impact of repeated observations, which can be used to search for variability of the central star and/or potential companions and push the 5-σ limiting magnitude fainter when observations are combined.

2.5 Conclusions

In this work we presented synthetic absolute magnitudes in the *ugrizy* filters of 13 PN models representing the evolution of a PN for a 3 $M_{\odot}$ progenitor star over $\sim$5000 years (Table 2.4). We have calculated the colors for various photometric aperture sizes to explore spatially resolved and unresolved cases. We showed that our model magnitudes and colors are consistent with real observations for both resolved and unresolved cases. We also showed that VRO will allow for the identification of many PNe in the Milky Way and neighboring galaxies.

Color-color diagrams will be useful in differentiating PNe from other point sources in the upcoming VRO era. We showed that the PNe model colors are entirely separate from most other SDSS objects cataloged in SDSS; indeed, we can simply provide a cutoff above $r-i=-0.75$ to find viable PNe candidates. Moreover, we showed that colors can also differentiate younger PNe ($t_{age} < 7000$ yrs) from older PNe ($t_{age} > 7500$ yrs). This will likely still be possible even in the presence of large amounts of extinction. There is still work to be done on how colors of PNe with various progenitor masses will change.

Given the VRO seeing limited resolution and magnitude limits, PNe detected at various distances will be spatially resolved to varying degrees. For distances to the Galactic center, the youngest PNe ($t_{age} \approx 3500$ yrs) will saturate with $A_V \leq 2$ mags, be visible up to $A_V \approx 10$ mags, and be partially resolved. The oldest PNe ($t_{age} \approx 8300$ yrs) will be visible up to $A_V \approx 5$ mags and be mostly resolved. Young PNe ($t_{age} < 6300$ yrs) at the LMC/SMC will be fully unresolved and visible for moderate A_V between ~ 1 and 5 mags while older models will be resolved containing at least 20% of the nebular emission. For distances similar to M31, all PNe will be unresolved but only younger PNe ($t_{age} < 7300$ yrs) will be visible with A_V between ~ 0.6 and 2.4 mags. This and future works will help prepare the astronomical community for the massive amounts of data that will be provided by VRO and enable the discovery of unprecedented numbers of new PNe, enabling detailed tests of our current theories of this phase of stellar evolution.

2.6 Acknowledgements

The specific use of Cloudy in this work is through the Python wrapper pyCloudy which allows the user to interact with the Cloudy input and output files through Python (Morisset, 2013). This research has made use of the Spanish Virtual Observatory (http://svo.cab.inta-csic.es) supported from the Spanish MINECO/FEDER through grant AyA2014-55216. This research has made use of the VizieR catalogue access tool, CDS, Strasbourg, France. This research has made use of the SIMBAD database, operated at CDS, Strasbourg, France. This work made use of the IPython package (Pérez and Granger, 2007). This research made use of SciPy (Jones et al., 2001). This research made use of NumPy (Van Der Walt et al., 2011) This research made use of matplotlib, a Python library for publication quality graphics (Hunter et al., 2007). This research made use of ds9, a tool for data visualization supported by the Chandra X-ray Science Center (CXC) and the High Energy Astrophysics Science Archive Center (HEASARC) with support from the JWST Mission office at the Space Telescope Science Institute for 3D visualization. This research made use of Astropy, a community-developed core Python package for Astronomy (Astropy Collaboration et al., 2013). Funding for the Sloan Digital Sky Survey IV has been provided by the Alfred P. Sloan Foundation, the U.S. Department of Energy Office of Science, and the Participating Institutions. SDSS-IV acknowledges support and resources from the Center for High-Performance Computing at the University of Utah. The SDSS web site is www.sdss.org. SDSS-IV is managed by the Astrophysical Research Consortium for the Participating Institutions of the SDSS Collaboration including the Brazilian Participation Group, the Carnegie Institution for Science, Carnegie Mellon University, the Chilean Participation Group, the French Participation Group, Harvard-Smithsonian Center for Astrophysics, Instituto de Astrofísica de Canarias, The Johns Hopkins University, Kavli Institute for the Physics and Mathematics of the Universe (IPMU) / University of Tokyo, Lawrence Berkeley National Laboratory, Leibniz Institut für Astrophysik Potsdam (AIP), Max-Planck-Institut für Astronomie (MPIA Hei-

delberg), Max-Planck-Institut für Astrophysik (MPA Garching), Max-Planck-Institut für Extraterrestrische Physik (MPE), National Astronomical Observatories of China, New Mexico State University, New York University, University of Notre Dame, Observatário Nacional / MCTI, The Ohio State University, Pennsylvania State University, Shanghai Astronomical Observatory, United Kingdom Participation Group, Universidad Nacional Autónoma de México, University of Arizona, University of Colorado Boulder, University of Oxford, University of Portsmouth, University of Utah, University of Virginia, University of Washington, University of Wisconsin, Vanderbilt University, and Yale University. Funding for the SDSS and SDSS-II has been provided by the Alfred P. Sloan Foundation, the Participating Institutions, the National Science Foundation, the U.S. Department of Energy, the National Aeronautics and Space Administration, the Japanese Monbukagakusho, the Max Planck Society, and the Higher Education Funding Council for England. The SDSS is managed by the Astrophysical Research Consortium for the Participating Institutions. The Participating Institutions are the American Museum of Natural History, Astrophysical Institute Potsdam, University of Basel, University of Cambridge, Case Western Reserve University, University of Chicago, Drexel University, Fermilab, the Institute for Advanced Study, the Japan Participation Group, Johns Hopkins University, the Joint Institute for Nuclear Astrophysics, the Kavli Institute for Particle Astrophysics and Cosmology, the Korean Scientist Group, the Chinese Academy of Sciences (LAMOST), Los Alamos National Laboratory, the Max-Planck-Institute for Astronomy (MPIA), the Max-Planck-Institute for Astrophysics (MPA), New Mexico State University, Ohio State University, University of Pittsburgh, University of Portsmouth, Princeton University, the United States Naval Observatory, and the University of Washington.

George Vejar thanks the LSSTC Data Science Fellowship Program, his time as a Fellow has benefited this work.

Table 2.5: Absolute magnitudes for all 13 PN models for corresponding $\Omega_{\rm aperture}/\Omega_{\rm neb}$ and f_{neb}

Variant I:	$\Omega_{\rm aperture}/\Omega_{\rm neb} = 1.3$			f_{neb} = 1		
Age	u	g	r	i	z	y
(yrs)	(mags)	(mags)	(mags)	(mags)	(mags)	(mags)
3502	-2.59	-3.63	-3.38	-2.20	-2.18	-2.09
4154	-2.70	-3.91	-3.47	-2.21	-2.20	-2.15
4860	-2.46	-3.94	-2.98	-1.87	-1.98	-1.94
5663	-2.11	-3.66	-2.53	-1.44	-1.62	-1.66
6328	-1.93	-3.41	-2.36	-1.21	-1.40	-1.49
6745	-1.95	-3.23	-2.43	-1.14	-1.29	-1.39
7031	-1.98	-3.00	-2.53	-1.06	-1.13	-1.28

7224	-2.00	-2.72	-2.64	-0.98	-0.98	-1.21
7387	-1.71	-2.10	-2.49	-0.63	-0.54	-0.95
7453	-1.44	-1.60	-2.27	-0.33	-0.18	-0.72
7552	-1.09	-0.90	-1.98	0.08	0.28	-0.45
7751	-0.75	-0.22	-1.68	0.45	0.71	-0.24
8351	-0.51	0.24	-1.46	0.73	1.00	-0.11
Variant II:		$\Omega_{\rm aperture}/\Omega_{\rm neb} = 0.9$			$f_{neb} = 4 \times 10^{-1}$	
3502	-1.88	-2.78	-2.52	-1.39	-1.35	-1.24
4154	-1.90	-3.03	-2.58	-1.35	-1.33	-1.27
4860	-1.62	-3.04	-2.09	-0.99	-1.10	-1.05
5663	-1.25	-2.76	-1.63	-0.56	-0.73	-0.77
6328	-1.06	-2.51	-1.46	-0.32	-0.50	-0.59
6745	-1.06	-2.33	-1.54	-0.24	-0.39	-0.49
7031	-1.09	-2.10	-1.63	-0.16	-0.24	-0.38
7224	-1.10	-1.82	-1.74	-0.08	-0.08	-0.31
7387	-0.82	-1.20	-1.59	0.27	0.36	-0.05
7453	-0.55	-0.70	-1.37	0.57	0.72	0.19
7552	-0.20	0.00	-1.07	0.97	1.18	0.45
7751	0.14	0.67	-0.78	1.35	1.60	0.66
8351	0.38	1.13	-0.56	1.62	1.89	0.79
Variant III:		$\Omega_{\rm aperture}/\Omega_{\rm neb} = 0.7$			$f_{neb} = 2 \times 10^{-1}$	
3502	-1.45	-2.17	-1.90	-0.83	-0.77	-0.65
4154	-1.35	-2.38	-1.93	-0.74	-0.70	-0.63
4860	-1.03	-2.38	-1.43	-0.36	-0.45	-0.39
5663	-0.63	-2.09	-0.97	0.10	-0.07	-0.10
6328	-0.41	-1.84	-0.79	0.34	0.17	0.08
6745	-0.41	-1.66	-0.86	0.43	0.29	0.18
7031	-0.42	-1.42	-0.95	0.51	0.44	0.30
7224	-0.44	-1.14	-1.06	0.59	0.60	0.37
7387	-0.15	-0.53	-0.91	0.94	1.04	0.63
7453	0.12	-0.02	-0.69	1.24	1.39	0.86
7552	0.47	0.67	-0.39	1.64	1.85	1.13

7751	0.81	1.34	-0.10	2.02	2.27	1.34
8351	1.04	1.79	0.12	2.29	2.56	1.47
Variant IV:		$\Omega_{\rm aperture}/\Omega_{\rm neb} = 0.5$			$f_{neb} = 1 \times 10^{-1}$	
3502	-1.08	-1.53	-1.24	-0.27	-0.17	-0.03
4154	-0.82	-1.65	-1.20	-0.08	-0.02	0.07
4860	-0.42	-1.61	-0.68	0.35	0.28	0.35
5663	0.05	-1.31	-0.20	0.83	0.69	0.67
6328	0.31	-1.05	-0.01	1.10	0.94	0.87
6745	0.34	-0.86	-0.07	1.20	1.07	0.97
7031	0.34	-0.62	-0.16	1.29	1.22	1.09
7224	0.34	-0.34	-0.26	1.38	1.39	1.17
7387	0.63	0.27	-0.11	1.72	1.82	1.42
7453	0.90	0.76	0.11	2.03	2.18	1.66
7552	1.24	1.46	0.41	2.42	2.64	1.93
7751	1.58	2.11	0.70	2.80	3.05	2.14
8351	1.81	2.55	0.92	3.07	3.34	2.27
Variant V:		$\Omega_{\rm aperture}/\Omega_{\rm neb} = 0.3$			$f_{neb} = 4 \times 10^{-2}$	
3502	-0.77	-0.83	-0.47	0.27	0.45	0.63
4154	-0.31	-0.73	-0.27	0.67	0.80	0.93
4860	0.23	-0.58	0.29	1.20	1.21	1.31
5663	0.82	-0.23	0.82	1.77	1.69	1.71
6328	1.19	0.05	1.06	2.11	1.99	1.94
6745	1.30	0.25	1.03	2.24	2.15	2.07
7031	1.35	0.49	0.96	2.36	2.31	2.20
7224	1.38	0.77	0.86	2.45	2.48	2.28
7387	1.68	1.37	1.02	2.80	2.92	2.54
7453	1.94	1.86	1.24	3.10	3.26	2.78
7552	2.29	2.52	1.54	3.49	3.71	3.05
7751	2.61	3.14	1.83	3.85	4.11	3.25
8351	2.83	3.54	2.05	4.11	4.38	3.39
Variant VI:		$\Omega_{\rm aperture}/\Omega_{\rm neb} = 0.15$			$f_{neb} = 9 \times 10^{-3}$	
3502	-0.62	-0.32	0.10	0.61	0.85	1.08

4154	-0.01	0.11	0.59	1.23	1.45	1.65
4860	0.66	0.51	1.24	1.90	2.06	2.23
5663	1.41	1.01	1.91	2.63	2.72	2.82
6328	1.96	1.38	2.29	3.13	3.16	3.20
6745	2.23	1.62	2.36	3.38	3.40	3.39
7031	2.40	1.88	2.35	3.56	3.60	3.56
7224	2.50	2.15	2.30	3.70	3.79	3.67
7387	2.84	2.73	2.48	4.06	4.22	3.95
7453	3.10	3.17	2.70	4.35	4.54	4.18
7552	3.42	3.75	3.00	4.71	4.95	4.45
7751	3.71	4.25	3.28	5.03	5.30	4.66
8351	3.90	4.55	3.50	5.25	5.54	4.80
Variant VII:		$\Omega_{\rm aperture}/\Omega_{\rm neb} = 0.1$			$f_{neb} = 4 \times 10^{-3}$	
3502	-0.59	-0.21	0.24	0.68	0.94	1.18
4154	0.06	0.35	0.83	1.36	1.61	1.84
4860	0.76	0.89	1.54	2.09	2.30	2.52
5663	1.55	1.50	2.28	2.88	3.05	3.22
6328	2.17	1.96	2.77	3.47	3.60	3.70
6745	2.52	2.24	2.94	3.80	3.90	3.96
7031	2.75	2.51	3.00	4.03	4.14	4.16
7224	2.91	2.79	2.99	4.20	4.35	4.30
7387	3.27	3.33	3.20	4.57	4.77	4.60
7453	3.52	3.73	3.42	4.85	5.07	4.84
7552	3.83	4.22	3.71	5.18	5.44	5.11
7751	4.09	4.64	3.99	5.47	5.76	5.32
8351	4.27	4.88	4.20	5.67	5.96	5.45
Variant VIII:		$\Omega_{\rm aperture}/\Omega_{\rm neb} = 0.075$			$f_{neb} = 2 \times 10^{-3}$	
3502	-0.58	-0.16	0.30	0.71	0.98	1.23
4154	0.08	0.47	0.96	1.42	1.69	1.93
4860	0.80	1.10	1.70	2.18	2.43	2.67
5663	1.62	1.81	2.50	3.01	3.24	3.45
6328	2.28	2.35	3.08	3.66	3.86	4.02

6745	2.67	2.68	3.34	4.04	4.21	4.35
7031	2.95	2.97	3.47	4.31	4.49	4.59
7224	3.15	3.24	3.52	4.52	4.72	4.76
7387	3.52	3.74	3.76	4.90	5.13	5.09
7453	3.77	4.10	3.99	5.17	5.42	5.32
7552	4.07	4.52	4.28	5.48	5.75	5.59
7751	4.32	4.86	4.55	5.74	6.03	5.80
8351	4.48	5.07	4.74	5.92	6.21	5.94
Variant IX:		$\Omega_{\rm aperture}/\Omega_{\rm neb} = 0.05$			$f_{neb} = 1 \times 10^{-3}$	
3502	-0.57	-0.13	0.34	0.72	1.00	1.25
4154	0.10	0.53	1.02	1.45	1.73	1.98
4860	0.82	1.22	1.78	2.22	2.49	2.74
5663	1.65	1.98	2.61	3.08	3.34	3.57
6328	2.33	2.58	3.24	3.76	4.00	4.20
6745	2.75	2.95	3.57	4.17	4.39	4.57
7031	3.05	3.25	3.77	4.47	4.69	4.85
7224	3.28	3.53	3.88	4.70	4.93	5.05
7387	3.66	4.00	4.16	5.09	5.34	5.40
7453	3.91	4.32	4.39	5.34	5.61	5.64
7552	4.19	4.69	4.68	5.64	5.92	5.90
7751	4.43	4.98	4.93	5.89	6.18	6.12
8351	4.59	5.16	5.11	6.05	6.35	6.26
Variant X:		$\Omega_{\rm aperture}/\Omega_{\rm neb} = 0.01$			$f_{neb} = 3 \times 10^{-5}$	
3502	-0.57	-0.10	0.37	0.74	1.02	1.28
4154	0.11	0.60	1.10	1.48	1.77	2.03
4860	0.85	1.36	1.88	2.27	2.57	2.83
5663	1.69	2.22	2.75	3.16	3.45	3.72
6328	2.39	2.93	3.47	3.88	4.18	4.45
6745	2.84	3.38	3.92	4.34	4.64	4.91
7031	3.17	3.72	4.26	4.68	4.98	5.25
7224	3.44	3.98	4.52	4.95	5.25	5.52
7387	3.84	4.39	4.91	5.34	5.65	5.91

7453	4.08	4.63	5.15	5.59	5.89	6.15
7552	4.36	4.91	5.43	5.86	6.16	6.42
7751	4.58	5.13	5.65	6.08	6.38	6.64
8351	4.72	5.27	5.79	6.22	6.52	6.78

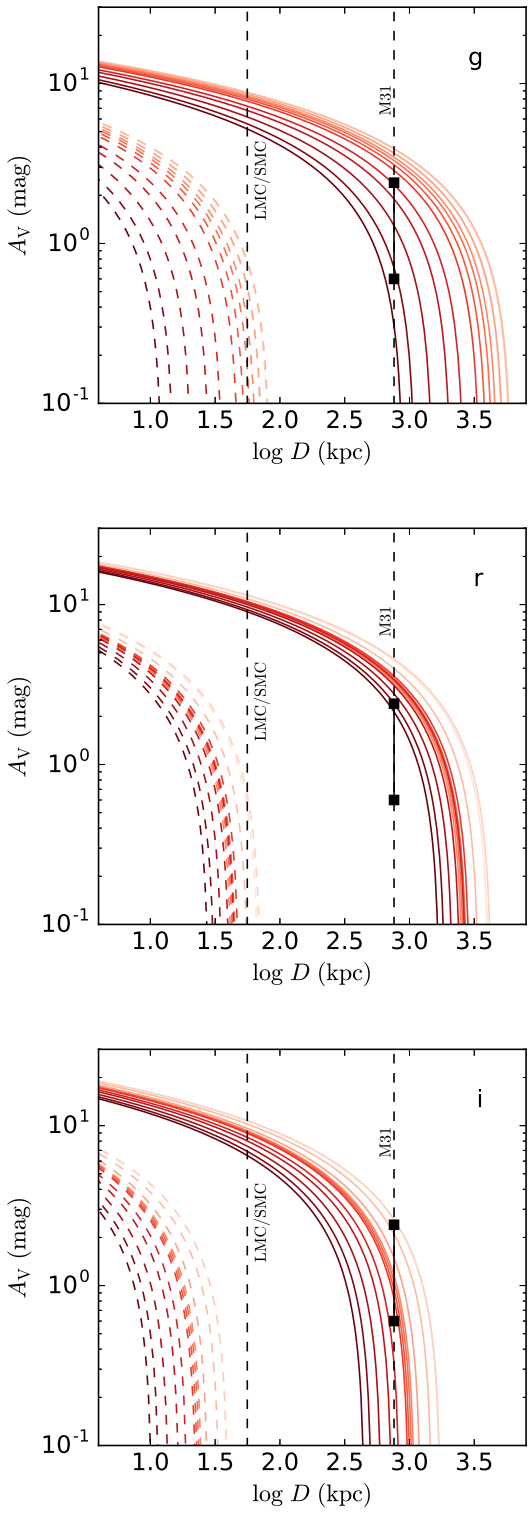

Figure 2.10: Magnitude limits based on the VRO saturation and 5σ detection limits for three filters as a function of distance and extinction (LSST Science Collaboration et al., 2009). Models shown represent fully unresolved PNe. Lines shaded for age, lighter correspond to younger models. Dashed red lines show distance at which PNe will saturate for given amount of extinction. Solid lines show distance at which PNe will reach the 5σ detection limit. Black squares show range of extinction values for M31 ($0.6 \geq A_V \leq 2.4$ (Dalcanton et al., 2015))

CHAPTER 3

Detailed Abundances of Planet-Hosting Open Clusters. The Praesepe (Beehive) Cluster

This chapter is based on work published in The Astrophysical Journal, 2021, Volume 919, Article ID 100.

3.1 Abstract

It is not yet fully understood how planet formation affects the properties of host stars, in or out of a cluster; however, abundance trends can help us understand these processes. We present a detailed chemical abundance analysis of six stars in Praesepe, a planet-hosting open cluster. Pr0201 is known to host a close-in (period of 4.4 days) giant planet (mass of $0.54 M_J$), while the other five cluster members in our sample (Pr0133, Pr0081, Pr0208, Pr0051, and Pr0076) have no detected planets according to RV measurements. Using high-resolution, high signal-to-noise echelle spectra obtained with Keck/HIRES and a novel approach to equivalent width measurements (XSpect-EW), we derived abundances of up to 20 elements spanning a range of condensation temperatures (T_C). We find a mean cluster metallicity of [Fe/H] = +0.21$\pm$0.02 dex, in agreement with most previous determinations. We find most of our elements show a [X/Fe] scatter of $\sim$0.02-0.03 dex and conclude that our stellar sample is chemically homogeneous. The T_C slope for the cluster mean abundances is consistent with zero and none of the stars in our sample exhibit individually a statistically significant T_C slope. Using a planet engulfment model, we find that the planet-host, Pr0201, shows no evidence of significant enrichment in its refractory elements when compared to the cluster mean that would be consistent with a planetary accretion scenario.

3.1.1 Introduction

It has been over a decade now since the discoveries of Meléndez et al. (2009) and Ramírez et al. (2009) suggesting that the formation of our solar system's planets have imprinted a measurable trend on the elemental abundances of the Sun. This trend, known as the condensation temperature (T_C) trend, can be influenced in various ways depending on the formation and evolution of the planetary system. Planet formation may reduce abundances in refractory elements ($T_C > 900$K), imparting a negative trend on abundances vs T_C since refractory-depleted material can still be accreted by the host star during the lifetime of the protoplanetary disk (Saffe et al., 2017). Planets in orbit can also be engulfed by their host star, which in turn could result in a positive slope since the star is accreting refractory-rich material into its outer layers (Mack et al., 2014). The T_C slope can inform us on the amount of planetary material sequestered or accreted and help us determine if planet formation has occurred in the first place, in cases where planets have not been detected by other

means. Planetary signatures and T_C trends have been studied by numerous groups making use of wide binary systems with at least one known planet in order to take advantage of the assumption that they formed from the same molecular cloud and any differences in their abundances would be due to planet formation (Ramírez et al., 2011; Mack et al., 2014; Tucci Maia et al., 2014; Biazzo et al., 2015; Ramírez et al., 2015; Saffe et al., 2015; Teske et al., 2015; Mack et al., 2016; Saffe et al., 2017; Ramírez et al., 2019). In this work, we apply similar methods to another chemically homogeneous stellar population: the Praesepe Open Cluster.

Open clusters are important laboratories for understanding a broad range of astrophysical phenomena. They have been used to study Galactic chemical evolution (Boesgaard et al., 2020; Anthony-Twarog et al., 2018), the structure and evolution of the Galactic disk (Reddy et al., 2015; MacLean et al., 2015), stellar physics (Davis et al., 2019; Schuler et al., 2009a), and light element abundances (Boesgaard et al., 2016; François et al., 2013), to name a few. The basis of all these studies is the assumption that open clusters are stellar conglomerates containing coeval stars that form out of a well-mixed molecular cloud. This implies that the stars in a given open cluster are the same age and have the same primordial compositions. These properties allow for the systematic determination of their ages (Maurya and Joshi, 2020; Sandquist et al., 2016), distances (Monteiro and Dias, 2019; González-Díaz et al., 2019), kinematic properties (Maurya and Joshi, 2020; Geller et al., 2015), and detailed compositions (Lum and Boesgaard, 2019; Liu et al., 2016a). There may be more useful information available about the cluster environment than there would be about a wide binary system, such as more accurate age determinations. A cluster can provide these advantages and many more stars to analyze in the context of exoplanets.

According to Meibom et al. (2013), planets in stellar clusters may be just as likely as planets around field stars, but a cluster environment can also be hostile to the formation of planets and currently there are only tens of known planets in open clusters (Cai et al., 2019). The main difference between field and cluster stars comes in the effect of the chaotic cluster environment on the formation process (protoplanetary disk) or already formed systems. O/B stars emit high energy FUV photons that can photoevaporate nearby circumstellar disks, limiting planet formation timescales (Anderson et al., 2013; Haworth et al., 2018; Winter et al., 2018). Stellar fly-by's are frequent in the first 1-2 Myr after cluster formation which can lead to smaller systems (< 5.5 AU in size) affecting 12-20% of stars in the lifetime of a cluster similar to Praesepe (Pfalzner et al., 2018). Flybys can also eject planets from a system with an efficiency of a few percent to $\sim$10% depending on semi-major axis of the planet, mass of the host star, and age of the cluster (Fujii and Hori, 2019). Gas expulsion from stellar winds of massive stars or supernova explosions can cause a cluster to become supervirial and boost ejection rates as the cluster reestablishes virial equilibrium (Zheng et al., 2015). In low density environments (2k stars in 1pc virial radius), survival rates for systems containing multiple Jupiter-sized planets could be about 84% and 90% for Earth-only systems in the first 50 Myr (Cai et al., 2017). Based off estimates of the

specific-free floating planet production rate from Pacucci et al. (2013), Praesepe could have produced more than 1500 free floating planets. Aside from cluster environment, intra-system dynamics/evolution will also affect a fraction of surviving planetary systems such as: planetary migration (Mayor and Queloz, 1995; Lin et al., 1996), Kozai-Lidov effect (Naoz, 2016), and planet-planet scattering (Johansen et al., 2012) depending on the structure of the system. The effectiveness of these mechanisms depends heavily on the size and structure of the cluster.

In this paper, we present the analysis of detailed abundance trends for six stars in Praesepe, a planet-hosting open cluster. In Section 3.2, we describe our sample, observations/data, spectral analysis including our novel approach to measuring absorption line EWs, and verify our methods. In Section 3.3, we compare our results to the literature and present the derived stellar abundances and observed trends. In Section 3.4, we discuss our results in the context of a simple model for how the accretion of Earth-like rocky planets would affect refractory elemental abundances as a function of T_C and atomic number. Finally, we briefly summarize the main conclusions in Section 3.5.

3.2 Data and Analysis

3.2.1 Stellar Sample

Stars in Praesepe are of special interest due to the discovery of planets around a number of its members (Quinn et al., 2012; Cai et al., 2019). Praesepe is home to $\sim$1000 stars, is relatively close by at 182 pc (Cantat-Gaudin et al., 2018), and has an age of $\sim$600 Myr (Delorme et al., 2011), making it a strong candidate for high resolution spectroscopy of main sequence sun-like stars. It has the highest metallicity ([Fe/H] = +0.21 $\pm$ 0.01 dex) of any nearby open cluster according to D'Orazi et al. (2020), which can increase the likelyhood of giant planet formation (Johnson et al., 2010) if the metallicity correlation applies to stars in open clusters.

The six stars in our sample consist of a planet-host, Pr0201, and five non-hosts: Pr0133, Pr0081, Pr0076, Pr0051, and Pr0208. The data used in this study are a combination of spectra acquired by our group in 2013 and high-quality Keck Observatory Archive (KOA) spectra taken at an earlier time, all of which are publicly available. While other planet-hosts exist within Praesepe, we only acquired data for Pr0201. The derived temperatures (see Sections 2.3 and 2.4) for our stars cover $\sim$500 K with spectral classes between G5 and F8 shown in Table 3.1. Half of our stars have temperatures within 100 K from the Sun and the other half are hotter with temperatures $\sim$6100 K. Five out of the six stars have similar surface gravity estimates ranging from 4.34 to 4.44 dex and errors of about 0.10 dex. Pr0133 is an exception having a much lower surface gravity of 4.18 dex. The metallicity of our stars ranges between 0.16 and 0.26 with an average of $+0.21 \pm 0.02$ dex. In Figure 3.1, we show broadband SED fits (using the methodology of Stassun and Torres, 2016) for two of our stars which are also consistent with our spectral analysis.

Table 3.1: Stellar Parameters. Adopted solar parameters: $T_{\rm eff} = 5777$ K, $\log g = 4.44$, and $\xi = 1.38$ km s^{-1}.

	Pr0201	Pr0133	Pr0208	Pr0081	Pr0051	Pr0076 (2003)	Pr0076 (2013)
$T_{\rm eff}$(K)	6168 ± 35	6067 ± 60	5869 ± 46	5731 ± 42	6017 ± 27	5789 ± 72	5748 ± 24
$\log g$ (cgs)	4.34 ± 0.10	4.18 ± 0.12	4.37 ± 0.13	4.44 ± 0.11	4.40 ± 0.07	4.48 ± 0.12	4.44 ± 0.07
[Fe/H]	0.23 ± 0.05	0.19 ± 0.06	0.26 ± 0.07	0.18 ± 0.06	0.16 ± 0.03	0.25 ± 0.06	0.22 ± 0.05
ξ (km s^{-1})	1.52 ± 0.06	1.74 ± 0.11	1.53 ± 0.07	1.41 ± 0.06	1.54 ± 0.05	1.33 ± 0.04	1.35 ± 0.03

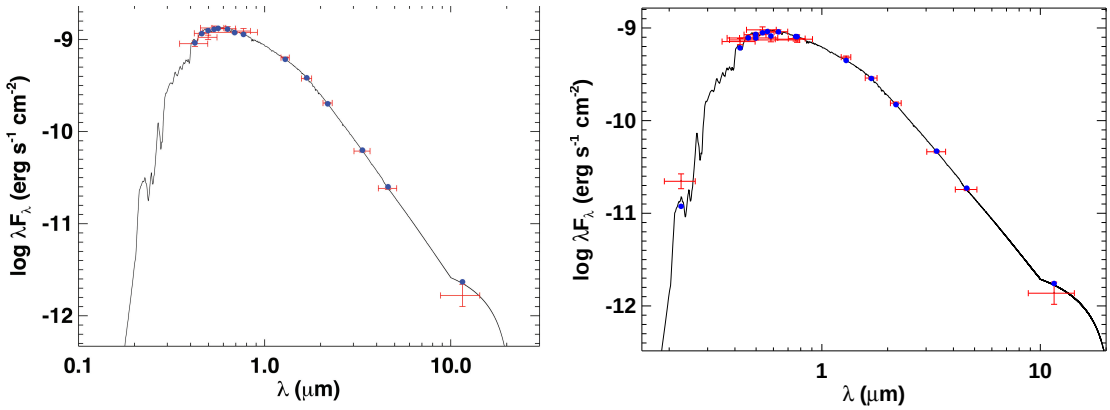

Figure 3.1: Spectral Energy Distributions for two representative targets in our study sample. Red symbols represent the broadband fluxes drawn from GALEX (Martin et al., 2003), APASS (Henden et al., 2009), 2MASS (Skrutskie et al., 2006), and WISE (Wright et al., 2010). Black curve is the best fitting Kurucz atmosphere model. Blue symbols are the model fluxes corresponding to each of the observed passbands. The integrated bolometric fluxes together with the *Gaia* DR2 parallax (Gaia Collaboration et al., 2018) yields the stellar radii. (Left) Pr0201: Reduced χ^2 = 2.1, best fit extinction is A_V = 0.072 $\pm$ 0.024, resulting in a bolometric flux at Earth of F_{bol} = 1.77 $\pm$ 0.03 $\times 10^{-9}$ erg s^{-1} cm^{-2}, giving a radius of R = 1.166 $\pm$ 0.022 $R_\odot$. (Right) Pr0051: Reduced χ^2 = 1.2, best fit extinction is A_V = 0.07 $\pm$ 0.03, resulting in a bolometric flux at Earth of $F_{\rm bol} = 1.241 \pm 0.029 \times 10^{-9}$ erg s^{-1} cm^{-2}, giving a radius of R = 1.086 $\pm$ 0.019 $R_\odot$.

3.2.2 Data Acquisition

Three of the six stars (Pr0201, Pr0051, and Pr0076) were observed on UT 2013 December 9 with the HIRES echelle spectrograph (Vogt et al., 1994) in the R $= \lambda/\Delta\lambda = 72,000$ mode on the 10-m Keck I telescope. We used the kv418 filter combined with the B2 slit setting ($0\farcs574 \times 7''$) and 2×1 binning; the spectra cover a wavelength range of 4600–9000Å. One exposure was taken for each star, with an integration time of 1200 s for Pr0201 and 2100 s for Pr0051 and Pr0076 individually. The signal-to-noise ratio (S/N) in the continuum near 6700Å for Pr0201 and Pr0051 is $\sim$300, and for Pr0076, it is $\sim$250.

For the remaining three stars, Pr0133, Pr0208, and Pr0081, we obtained raw data files from the KOA. These spectra, which we will collectively refer to as archive spectra, were taken in UT 2003 in January and February belonging to program ID H39aH and H47aH; the data are fully described in Boesgaard et al. (2013). We also obtained an archive spectrum for Pr0076 from the same program to verify that our analysis produces

consistent results between these different sets of spectra. In our final results we report the stellar parameters and abundances for Pr0076 from both data sets and adopt the results from data taken in 2013. The archive spectra covered a smaller wavelength range (5650–8090Å) than our new spectra and were obtained in the R = 48,000 mode. One exposure was taken for each star with an integration time of 840 s for Pr0133, 1200 s for Pr0208, 1500 s for Pr0076, and 1500 s for Pr0081. The S/N in the continuum near 6700Å for these spectra is ∼220.

All of the data were reduced consistently using the MAKEE data reduction software. We required a solar spectrum to derive the solar abundances used to determine the abundances of our target stars relative to the Sun. For this purpose, we used the high-quality Keck/HIRES solar spectrum (S/N ∼ 800 near 6700Å) from Schuler et al. (2015) obtained in 2010 June in the R=50,000 mode over the wavelength range 3750–8170Å. A sample region of the spectra used is shown in Figure 3.2 for Pr0076 from both data sets in comparison to the solar spectrum.

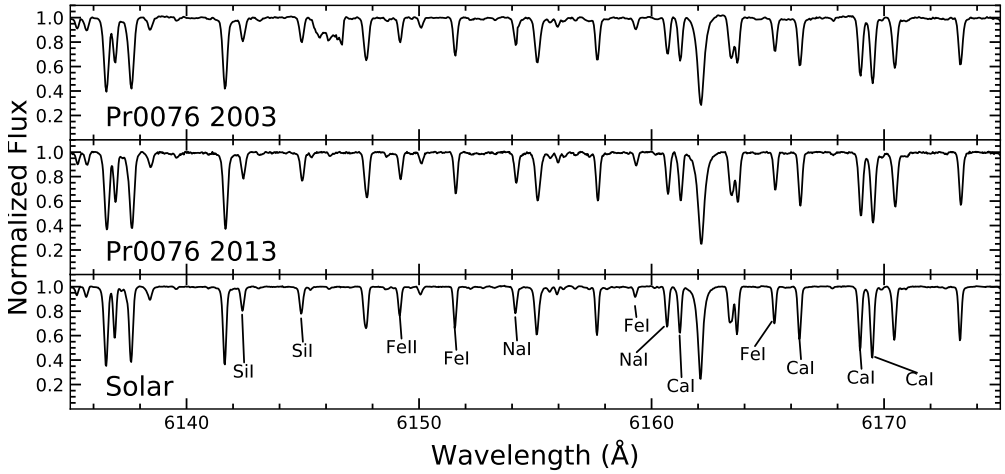

Figure 3.2: Sample Keck/HIRES spectra for Pr0076 and the sun, spanning a wavelength range of ∼ 6135 − 6175 Å. Top panel represents the archive data, middle panel represents data taken in 2013, and bottom panel shows the solar spectrum used. Marked absorption lines are those measured within this range.

3.2.3 Abundance and Stellar Parameter Determination

We have derived chemical abundances relative to solar ([X/H]) for up to 20 elements in each of our stars. For our analysis, the adopted solar parameters were $T_{\rm eff} = 5777$ K, $\log g = 4.44$, and $\xi = 1.38$ km s^{-1}. A sample of the adopted line lists, equivalent widths (EWs), and $\log(N)$ line-by-line abundances for each element are given in Table 3.2. We derived abundances from measurements of EWs of atomic absorption lines in combination with MOOG, an LTE spectral analysis package (Sneden, 1973, version 2014) and ATLAS9 stellar atmosphere models (Kurucz, 1993). For the archive spectra, we used an abbreviated line list excluding

lines not found in those spectra. To determine the stellar parameters of each star, we require the excitation and ionization balance of Fe I and Fe II lines. Atomic excitation energies (χ) and transition probabilities ($\log gf$) were taken from Mack et al. (2014). For the odd-Z elements Sc, V, Mn, and Co, hyper-fine structure (hfs) effects (Prochaska and McWilliam, 2000) are taken into account for strong lines through spectral synthesis incorporating hfs components; the resulting abundances are listed in Table 3.3. The hfs components were obtained from Johnson et al. (2006), and line lists for regions encompassing each feature were taken from VALD (Piskunov et al., 1995; Kupka et al., 1999). Adopted Sc, V, Mn, and Co abundances were derived from the hfs analysis and lines with EWs where hfs effects are negligible. The general abundance and error analysis method is detailed in Schuler et al. (2011b), with new methods used for our current analysis detailed below.

Table 3.2: Lines Measured, Equivalent Widths, and Abundances

	λ	χ		Solar		Pr0201		Pr0133		Pr0208		Pr0081		Pr0051		Pr0076	
Ion	(Å)	(eV)	log gf	$EW_\odot$	$\log N_\odot$	EW	$\log N$	EW	$\log N$	EW	$\log N$	EW	$\log N$	EW	$\log N$	EW	$\log N$
C I	5052.167	7.685	-1.304	31.58	8.417	48.52	8.481	–	–	–	–	–	–	44.66	8.507	–	–
	5380.337	7.685	-1.615	19.37	8.444	33.17	8.531	–	–	–	–	–	–	30.44	8.566	20.54	8.481
	6587.61	8.537	-1.021	12.2	8.358	28.46	8.565	20.64	8.387	20.58	8.567	14.05	8.454	19.24	8.43	12.22	8.358
	7111.469	8.64	-1.074	10.53	8.431	23.78	8.596	12.28	8.24	15.3	8.544	13.8	8.598	–	–	10.75	8.443
	7113.179	8.647	-0.762	22.81	8.563	40.39	8.642	30.7	8.482	26.88	8.581	26.74	8.694	30.7	8.561	24.98	8.632
N I	7468.313	10.336	-0.189	4.18	8.131	9.48	8.195	–	–	–	–	–	–	7.64	8.21	–	–
O I	6300.304	0.0	-9.72	5.10	8.838	4.96	8.930	–	–	–	–	–	–	–	–	8.44	9.141
	7775.39	9.15	0.001	45.45	8.806	84.57	9.078	84.38	9.139	61.74	9.007	58.58	9.097	67.51	8.951	51.79	8.96
	7774.17	9.15	0.223	64.78	8.925	105.5	9.139	95.89	9.082	77.69	9.039	64.0	8.968	86.72	9.013	64.3	8.96
	7771.94	9.15	0.369	69.65	8.856	119.2	9.16	106.3	9.076	86.34	9.018	72.46	8.956	98.46	9.024	74.15	8.97
Na I	5682.633	2.102	-0.7	98.56	6.282	102.5	6.552	–	–	116.8	6.555	–	–	99.82	6.419	119.2	6.524
	6154.226	2.102	-1.56	36.15	6.267	35.74	6.449	35.3	6.359	47.67	6.49	45.52	6.391	37.5	6.403	49.84	6.466
	6160.747	2.104	-1.26	54.69	6.255	49.66	6.374	51.33	6.317	64.53	6.43	61.46	6.321	54.25	6.362	67.11	6.411
Mg I	4730.029	4.346	-2.523	66.13	7.802	60.68	7.927	–	–	–	–	–	–	67.72	7.942	81.46	8.009
	5711.088	4.346	-1.833	103.6	7.597	96.82	7.725	–	–	117.8	7.827	–	–	103.6	7.718	119.7	7.798
	6965.409	5.753	-1.51	–	–	–	–	–	–	25.88	7.34	–	–	–	–	–	–
	6841.19	5.753	-1.61	64.3	7.849	69.54	8.004	77.19	8.063	85.91	8.139	–	–	68.45	7.942	74.84	8.08
Al I	6696.023	3.143	-1.347	37.33	6.253	–	–	–	–	47.45	6.453	44.71	6.348	39.17	6.39	51.94	6.47
	6698.673	3.143	-1.647	21.1	6.222	18.94	6.339	20.1	6.292	27.89	6.413	27.36	6.34	22.68	6.366	29.37	6.39
Si I	5701.104	4.93	-1.581	37.85	7.087	39.86	7.236	–	–	–	–	–	–	41.87	7.216	47.47	7.266
	5690.425	4.93	-1.769	50.48	7.485	54.33	7.66	–	–	59.0	7.641	–	–	51.69	7.563	57.96	7.621
	5708.4	4.954	-1.034	75.82	7.14	84.46	7.388	–	–	90.55	7.375	–	–	80.76	7.268	91.02	7.378
	5772.149	5.082	-1.358	50.81	7.213	58.97	7.445	59.77	7.384	66.03	7.466	62.82	7.402	56.25	7.35	63.21	7.42
	7405.772	5.614	-0.313	89.3	7.108	100.7	7.352	102.1	7.332	104.6	7.326	106.4	7.324	100.7	7.289	106.3	7.34
	6125.021	5.614	-1.464	32.55	7.48	39.8	7.688	39.12	7.62	41.65	7.658	39.71	7.614	38.83	7.631	41.96	7.657
	6244.466	5.616	-1.093	44.9	7.316	54.31	7.54	53.57	7.477	58.57	7.539	55.23	7.479	53.51	7.484	56.47	7.505
	6243.815	5.616	-1.242	44.62	7.46	53.32	7.675	55.52	7.655	57.63	7.675	53.49	7.604	48.09	7.555	62.3	7.734
	6145.016	5.616	-1.31	39.69	7.45	46.7	7.644	42.13	7.518	53.6	7.685	43.08	7.516	44.76	7.572	48.16	7.6
	6142.483	5.619	-1.295	33.85	7.339	39.73	7.522	35.73	7.397	41.73	7.495	39.28	7.443	38.38	7.459	43.42	7.516
	6848.58	5.863	-1.524	17.25	7.401	21.13	7.572	19.82	7.485	23.61	7.584	23.82	7.582	19.27	7.491	24.55	7.602
	6414.98	5.871	-1.035	46.89	7.484	55.2	7.671	–	–	–	–	–	–	54.52	7.622	59.12	7.665
	7003.569	5.964	-0.937	57.28	7.606	61.99	7.74	68.65	7.794	77.06	7.873	66.17	7.734	59.56	7.669	62.59	7.697
	6741.628	5.984	-1.428	15.06	7.344	20.56	7.56	19.67	7.49	22.05	7.553	19.79	7.491	18.54	7.477	20.47	7.511
S I	4694.113	6.525	-1.77	11.0	7.311	13.81	7.27	–	–	–	–	–	–	16.24	7.419	13.26	7.423
	4695.443	6.525	-1.92	6.13	7.167	11.15	7.307	–	–	–	–	–	–	9.21	7.267	9.29	7.382
	6757.171	7.87	-0.31	14.14	7.197	34.72	7.514	28.69	7.393	23.76	7.438	–	–	25.91	7.402	19.24	7.394
K I	7698.98	0.0	-0.17	155.6	5.278	156.3	5.617	164.0	5.611	–	–	171.8	5.397	164.8	5.55	174.6	5.457
Ca I	6572.779	0.0	-4.24	33.23	6.252	22.26	6.404	26.57	6.319	45.12	6.535	47.48	6.438	28.67	6.397	47.77	6.467
	6166.439	2.521	-1.142	70.02	6.281	68.18	6.487	69.96	6.409	83.04	6.522	82.72	6.441	73.04	6.458	84.55	6.496
	6169.042	2.523	-0.797	91.23	6.267	90.34	6.503	94.6	6.472	105.5	6.519	108.7	6.481	95.54	6.465	111.9	6.556

	6161.297	2.523	-1.266	62.73	6.291	55.6	6.408	57.2	6.327	72.38	6.481	70.25	6.372	62.23	6.414	77.07	6.505
	6169.563	2.526	-0.478	109.1	6.203	105.7	6.423	114.8	6.471	117.9	6.375	128.9	6.419	110.6	6.367	130.2	6.467
	7326.145	2.933	-0.208	109.5	6.217	109.3	6.465	–	–	–	–	–	–	113.9	6.405	132.1	6.48
	5867.562	2.933	-1.57	23.79	6.288	21.84	6.448	23.51	6.396	32.43	6.517	32.54	6.446	24.85	6.439	36.48	6.533
Sc II	6604.601	1.357	-1.309	36.77	3.217	41.01	3.319	39.38	3.124	43.33	3.377	41.49	3.362	40.08	3.295	43.39	3.415
	6320.851	1.5	-1.819	9.12	3.102	11.35	3.24	–	–	11.43	3.261	–	–	9.38	3.144	–	–
	6245.637	1.507	-1.03	34.46	3.058	38.73	3.158	36.45	2.952	39.43	3.191	35.59	3.135	35.55	3.094	38.06	3.2
Ti I	5039.957	0.021	-1.13	72.88	4.688	63.51	4.915	–	–	–	–	–	–	71.56	4.888	87.26	4.939
	5210.385	0.048	-0.884	87.96	4.747	77.02	4.925	–	–	–	–	–	–	84.93	4.898	102.0	4.989
	5064.653	0.048	-0.991	88.13	4.882	79.82	5.108	–	–	–	–	–	–	86.6	5.061	–	–
	5024.844	0.818	-0.602	70.96	4.924	65.67	5.181	–	–	–	–	–	–	68.36	5.074	84.73	5.167
	5022.868	0.826	-0.434	69.99	4.745	61.11	4.938	–	–	–	–	–	–	69.0	4.926	83.53	4.983
	5739.469	2.249	-0.6	8.24	4.825	–	–	–	–	11.67	5.061	–	–	–	–	12.64	5.01
	5866.451	1.067	-0.84	47.33	4.901	37.04	5.078	40.2	4.959	59.03	5.159	63.42	5.118	42.58	5.033	61.57	5.115
	6261.098	1.43	-0.479	48.81	4.903	40.65	5.097	42.08	4.956	58.6	5.122	59.96	5.034	44.9	5.035	62.91	5.112
	6258.102	1.443	-0.355	51.46	4.839	42.9	5.025	43.19	4.864	60.88	5.048	64.88	5.007	47.35	4.966	64.86	5.036
	6091.171	2.267	-0.423	12.84	4.864	12.15	5.127	–	–	–	–	–	–	12.33	5.024	23.92	5.172
	6098.658	3.062	-0.01	5.72	4.835	–	–	–	–	8.8	5.093	10.24	5.079	–	–	11.15	5.132
	7138.906	1.443	-1.59	6.34	4.825	–	–	–	–	–	–	–	–	–	–	11.07	5.06
Ti II	5154.068	1.566	-1.75	73.94	5.045	86.31	5.273	–	–	–	–	–	–	83.21	5.197	80.56	5.253
	5381.021	1.566	-1.92	60.55	4.933	72.6	5.15	–	–	–	–	–	–	68.14	5.059	69.83	5.186
	5336.786	1.582	-1.59	71.81	4.841	83.84	5.057	–	–	–	–	–	–	79.92	4.969	78.87	5.055
	4779.985	2.048	-1.26	63.97	4.859	75.92	5.066	–	–	–	–	–	–	72.79	4.999	67.48	5.002
V I	6285.15	0.275	-1.51	10.22	3.844	6.71	4.065	–	–	14.86	4.125	15.42	3.992	7.83	3.978	17.47	4.077
	6251.827	0.287	-1.34	13.46	3.824	8.9	4.041	–	–	17.94	4.065	22.2	4.029	11.25	3.995	24.85	4.114
	6224.529	0.287	-2.01	4.9	4.018	–	–	–	–	–	–	–	–	–	–	9.64	4.298
	6243.105	0.301	-0.98	28.1	3.879	18.71	4.067	22.53	3.97	35.54	4.112	43.06	4.102	23.92	4.041	43.85	4.141
	6111.645	1.043	-0.715	10.09	3.822	10.95	4.232	11.57	4.086	16.87	4.164	17.17	4.041	10.48	4.072	20.07	4.143
	5737.059	1.064	-0.74	11.14	3.938	7.52	4.119	–	–	13.46	4.118	–	–	10.11	4.121	15.13	4.064
	5727.048	1.081	-0.012	38.13	3.93	27.15	4.071	–	–	47.27	4.16	–	–	34.47	4.079	56.29	4.224
	6081.441	1.051	-0.579	14.95	3.892	–	–	–	–	–	–	–	–	12.94	4.048	27.06	4.187
	6090.214	1.081	-0.062	32.8	3.851	27.53	4.106	–	–	–	–	–	–	29.91	4.015	47.35	4.088
Cr I	6330.091	0.941	-2.92	27.03	5.631	19.96	5.835	22.6	5.722	34.39	5.859	38.79	5.81	24.57	5.804	40.18	5.858
	7400.249	2.9	-0.111	75.93	5.569	73.08	5.775	76.58	5.708	94.81	5.896	96.07	5.838	80.61	5.778	93.11	5.826
	5787.918	3.322	-0.083	45.16	5.51	45.24	5.744	–	–	–	–	–	–	50.71	5.739	62.14	5.789
	5783.85	3.322	-0.295	44.18	5.705	40.72	5.875	45.2	5.846	58.87	5.997	57.73	5.904	47.73	5.901	59.62	5.959
	5783.063	3.323	-0.5	30.73	5.656	29.43	5.859	29.03	5.742	–	–	44.19	5.878	32.97	5.838	42.79	5.871
	5702.306	3.449	-0.667	23.0	5.77	21.88	5.966	–	–	–	–	–	–	26.3	5.983	36.76	6.049
	6978.397	3.464	0.142	58.64	5.594	59.81	5.839	58.49	5.712	77.04	5.923	75.88	5.834	61.86	5.771	76.98	5.878
	6979.795	3.464	-0.41	35.36	5.74	33.2	5.921	32.11	5.794	43.8	5.935	47.11	5.919	37.75	5.916	50.97	6.002
Mn I	5432.546	0.0	-3.795	50.91	5.465	30.39	5.538	–	–	–	–	–	–	39.95	5.54	69.84	5.771
	5399.499	3.853	-0.287	37.61	5.518	37.5	5.739	–	–	–	–	–	–	39.15	5.677	52.82	5.785
Fe I	4779.439	3.42	-2.02	39.79	7.237	38.25	7.464	–	–	–	–	–	–	41.27	7.265	49.46	7.415
	4788.757	3.24	-1.76	65.33	7.29	65.69	7.558	–	–	–	–	–	–	67.74	7.337	75.06	7.480
	5054.643	3.64	-1.92	39.03	7.315	38.24	7.544	–	–	–	–	–	–	38.66	7.308	49.90	7.513
	5322.041	2.28	-2.8	61.14	7.267	56.99	7.503	–	–	–	–	–	–	60.04	7.246	–	–
	5379.574	3.69	-1.51	61.2	7.344	63.69	7.629	–	–	–	–	–	–	62.16	7.361	71.26	7.526
	5522.447	4.21	-1.55	43.66	7.55	44.22	7.775	–	–	–	–	–	–	45.5	7.583	55.06	7.752
	5543.936	4.22	-1.14	61.98	7.469	62.55	7.697	–	–	–	–	–	–	65.73	7.534	74.13	7.683
	5546.5	4.37	-1.31	49.71	7.563	54.14	7.849	–	–	–	–	–	–	53.6	7.631	65.04	7.830
	5546.991	4.22	-1.91	25.65	7.55	25.80	7.767	–	–	–	–	–	–	27.29	7.587	37.93	7.801
	5560.207	4.43	-1.19	51.79	7.539	51.81	7.744	–	–	–	–	–	–	54.52	7.586	63.11	7.735
	5577.03	5.03	-1.55	10.15	7.459	12.23	7.718	–	–	–	–	–	–	12.11	7.545	17.71	7.734
	5579.335	4.23	-2.4	8.92	7.492	9.60	7.741	–	–	–	–	–	–	10.54	7.573	13.65	7.695
	5587.574	4.14	-1.85	32.77	7.566	34.89	7.827	–	–	–	–	–	–	35.34	7.618	42.96	7.758
	5646.684	4.26	-2.5	7.54	7.54	7.28	7.735	–	–	–	–	–	–	7.68	7.548	12.24	7.768
	5651.469	4.47	-2.0	18.0	7.674	18.73	7.896	–	–	–	–	–	–	19.4	7.715	26.76	7.895
	5652.318	4.26	-1.95	26.79	7.652	27.59	7.882	–	–	–	–	–	–	28.11	7.682	36.45	7.848
	5661.346	4.28	-1.74	22.53	7.357	23.17	7.584	–	–	–	–	–	–	24.83	7.414	32.05	7.567
	5667.518	4.18	-1.58	50.25	7.66	53.20	7.929	–	–	–	–	–	–	53.97	7.726	64.38	7.908
	5677.684	4.1	-2.7	6.7	7.53	7.39	7.797	–	–	10.95	7.817	–	–	–	–	10.98	7.759
	5679.023	4.65	-0.92	58.87	7.584	60.58	7.813	–	–	71.40	7.827	–	–	61.95	7.635	72.62	7.816
	5680.24	4.19	-2.58	9.92	7.683	9.75	7.891	–	–	14.18	7.911	–	–	9.05	7.638	15.66	7.906
	5731.762	4.26	-1.3	57.03	7.576	56.69	7.783	–	–	66.22	7.768	–	–	61.82	7.659	71.12	7.821
	5732.275	4.99	-1.56	13.43	7.567	15.11	7.799	–	–	17.84	7.753	–	–	16.41	7.67	19.35	7.753

	5741.846	4.26	-1.85	31.14	7.643	34.40	7.921	–	–	40.82	7.874	–	–	34.98	7.721	43.17	7.871
	5752.032	4.55	-1.18	54.08	7.667	54.90	7.882	–	–	68.86	7.950	–	–	56.98	7.717	65.96	7.870
	5775.081	4.22	-1.3	58.13	7.556	59.23	7.790	61.45	7.730	72.73	7.840	71.63	7.764	61.02	7.606	71.72	7.793
	5778.45	2.59	-3.48	21.27	7.42	18.63	7.658	21.06	7.633	26.92	7.626	30.49	7.602	21.1	7.415	32.68	7.668
	5809.218	3.88	-1.84	49.01	7.61	47.99	7.822	52.62	7.807	62.60	7.885	63.09	7.832	50.32	7.634	61.91	7.836
	5934.655	3.93	-1.17	74.38	7.431	75.30	7.679	76.95	7.584	89.73	7.722	86.91	7.614	76.91	7.475	89.22	7.687
	6078.999	4.65	-1.12	45.07	7.535	50.94	7.831	–	–	–	–	–	–	49.91	7.62	56.95	7.740
	6085.259	2.76	-3.1	42.75	7.646	38.93	7.869	–	–	–	–	–	–	40.59	7.605	55.38	7.860
	6098.245	4.56	-1.88	15.83	7.553	18.10	7.819	19.53	7.803	25.52	7.863	23.83	7.762	18.08	7.623	25.01	7.800
	6151.617	2.18	-3.3	49.27	7.384	43.93	7.616	47.49	7.559	57.73	7.584	58.39	7.499	48.06	7.362	61.57	7.585
	6159.368	4.61	-1.97	12.49	7.568	14.80	7.846	16.39	7.842	23.85	7.957	17.56	7.727	14.42	7.641	19.69	7.800
	6165.36	4.14	-1.47	43.68	7.373	42.54	7.569	46.05	7.547	54.50	7.601	53.80	7.528	47.24	7.437	55.32	7.576
	6173.336	2.22	-2.88	67.93	7.337	65.82	7.612	72.32	7.575	80.69	7.596	83.04	7.558	68.7	7.351	–	–
	6187.987	3.94	-1.72	46.71	7.487	44.33	7.671	–	–	–	–	–	–	48.54	7.52	61.21	7.739
	6220.776	3.88	-2.46	19.45	7.588	14.92	7.681	14.36	7.593	23.50	7.747	23.80	7.680	19.8	7.598	26.27	7.753
	6226.73	3.88	-2.22	28.6	7.573	26.42	7.757	32.41	7.807	35.94	7.770	40.57	7.787	29.98	7.603	40.97	7.813
	6229.228	2.85	-2.81	37.66	7.34	36.74	7.613	38.93	7.554	49.51	7.607	47.29	7.482	39.5	7.375	51.30	7.577
	6240.645	2.22	-3.23	49.7	7.353	43.88	7.574	47.22	7.515	61.27	7.603	57.48	7.444	46.97	7.304	61.60	7.546
	6293.924	4.84	-1.72	13.4	7.567	16.08	7.841	–	–	–	–	–	–	17.19	7.697	21.86	7.823
	6297.793	2.22	-2.74	72.68	7.277	69.31	7.528	–	–	–	–	–	–	74.83	7.317	–	–
	6322.685	2.59	-2.43	75.11	7.374	73.58	7.637	75.98	7.535	93.21	7.725	88.04	7.561	78.5	7.436	93.00	7.685
	6380.743	4.19	-1.38	52.09	7.473	52.38	7.692	54.71	7.640	62.72	7.688	61.46	7.609	54.09	7.508	63.76	7.673
	6392.538	2.28	-4.03	16.51	7.491	11.36	7.634	15.95	7.710	21.32	7.703	22.94	7.636	13.95	7.404	23.94	7.679
	6597.557	4.79	-1.07	43.46	7.567	43.98	7.761	48.28	7.763	56.30	7.820	53.77	7.726	46.52	7.621	56.49	7.790
	6608.024	2.28	-4.03	16.74	7.486	16.50	7.810	16.67	7.721	21.75	7.702	24.26	7.655	15.1	7.433	26.47	7.726
	6609.11	2.56	-2.69	65.5	7.411	63.50	7.671	67.39	7.602	80.11	7.696	81.71	7.648	64.31	7.389	80.18	7.657
	6627.54	4.55	-1.68	27.39	7.63	29.37	7.869	32.19	7.860	37.53	7.876	35.11	7.771	28.94	7.664	38.38	7.848
	6653.85	4.15	-2.52	10.09	7.552	11.73	7.845	–	–	–	–	–	–	11.33	7.609	15.14	7.748
	6703.567	2.76	-3.16	37.17	7.566	31.54	7.753	35.81	7.738	47.06	7.799	48.00	7.726	36.14	7.546	50.64	7.795
	6710.316	1.49	-4.88	15.91	7.513	10.90	7.706	13.84	7.719	23.01	7.798	25.97	7.740	13.74	7.439	24.77	7.734
	6713.745	4.8	-1.6	20.94	7.63	23.80	7.884	22.24	7.788	29.59	7.872	30.95	7.846	23.89	7.705	31.10	7.861
	6716.222	4.58	-1.92	15.11	7.564	15.93	7.785	15.08	7.699	21.11	7.787	20.08	7.699	17.36	7.637	22.43	7.772
	6725.353	4.1	-2.3	17.17	7.549	16.88	7.761	17.32	7.708	24.44	7.794	26.13	7.764	18.2	7.58	25.17	7.756
	6726.666	4.61	-1.13	45.83	7.493	48.91	7.739	51.63	7.706	59.60	7.759	58.57	7.688	50.25	7.569	60.41	7.740
	6733.151	4.64	-1.58	26.82	7.599	28.65	7.830	29.50	7.784	35.31	7.814	35.81	7.767	29.43	7.656	38.31	7.829
	6739.52	1.56	-4.79	11.32	7.321	9.01	7.589	–	–	18.43	7.656	16.99	7.487	10.47	7.283	19.18	7.572
	6745.09	4.58	-2.16	7.8	7.477	9.17	7.749	–	–	14.37	7.822	–	–	8.13	7.497	13.17	7.726
	6745.957	4.08	-2.77	6.66	7.531	8.09	7.847	–	–	–	–	–	–	7.96	7.616	11.74	7.796
	6750.15	2.42	-2.62	73.4	7.332	69.88	7.570	72.88	7.476	85.02	7.559	87.06	7.518	73.7	7.337	88.39	7.581
	6752.716	4.64	-1.3	35.72	7.505	37.19	7.724	42.02	7.743	51.91	7.830	49.08	7.727	39.67	7.58	49.57	7.753
	7114.549	2.69	-4.01	7.57	7.455	6.74	7.709	–	–	11.19	7.715	14.01	7.725	9.48	7.562	11.81	7.656
	7284.835	4.14	-1.75	41.49	7.561	39.72	7.744	46.28	7.777	55.41	7.838	52.31	7.726	43.28	7.593	53.79	7.771
Fe II	4620.521	2.828	-3.315	53.41	7.435	67.36	7.641	–	–	–	–	–	–	64.51	7.68	57.82	7.608
	5197.577	3.23	-2.348	80.04	7.387	105.30	7.775	–	–	–	–	–	–	98.31	7.746	89.86	7.672
	5234.625	3.221	-2.279	80.43	7.314	105.70	7.701	–	–	–	–	–	–	98.12	7.662	89.54	7.585
	5264.812	3.23	-3.133	39.51	7.308	57.43	7.571	–	–	–	–	–	–	53.91	7.617	50.27	7.616
	5414.073	3.221	-3.645	25.69	7.486	40.63	7.730	–	–	–	–	–	–	36.77	7.748	31.12	7.687
	5425.257	3.199	-3.39	39.8	7.536	52.66	7.695	–	–	–	–	–	–	49.66	7.746	46.86	7.762
	6084.111	3.199	-3.881	20.4	7.542	31.34	7.728	–	–	–	–	–	–	27.42	7.73	25.58	7.752
	6113.322	3.221	-4.23	12.35	7.628	20.74	7.831	–	–	17.90	7.841	13.98	7.756	16.98	7.8	15.65	7.820
	6149.258	3.889	-2.841	36.26	7.549	51.45	7.722	52.47	7.653	48.11	7.783	38.23	7.658	46.4	7.77	39.17	7.689
	6247.557	3.892	-2.435	50.89	7.459	78.65	7.848	76.92	7.696	67.16	7.755	58.06	7.673	68.38	7.815	59.82	7.727
	7222.394	3.889	-3.402	18.76	7.63	24.49	7.668	31.20	7.762	–	–	22.18	7.797	27.26	7.867	21.07	7.770
	7449.335	3.889	-3.488	18.06	7.686	32.46	7.930	33.91	7.896	30.34	8.011	23.90	7.924	26.7	7.931	22.45	7.889
	7711.723	3.903	-2.683	44.82	7.533	66.54	7.784	72.21	7.784	59.00	7.789	53.25	7.776	59.31	7.821	50.48	7.735
Co I	5301.039	1.71	-2.0	19.9	4.945	–	–	–	–	–	–	–	–	15.26	5.017	24.35	5.054
	6093.143	1.74	-2.44	10.5	5.034	–	–	–	–	–	–	–	–	7.81	5.108	12.56	5.115
	6814.942	1.956	-1.9	18.5	4.959	11.96	5.07	13.57	4.956	26.79	5.242	25.16	5.103	17.65	5.136	26.59	5.156
	5647.234	2.28	-1.56	14.06	4.863	9.34	4.976	–	–	–	–	–	–	11.07	4.935	19.91	5.042
	6632.433	2.28	-2.0	8.7	5.012	–	–	–	–	12.44	5.262	12.04	5.146	–	–	13.42	5.217
Ni I	6643.629	1.676	-2.3	92.89	6.366	86.9	6.55	–	–	–	–	–	–	91.31	6.48	108.6	6.636
	6108.107	1.676	-2.45	65.59	6.062	57.99	6.226	58.99	6.056	72.29	6.216	76.1	6.217	60.95	6.142	74.99	6.234
	6327.593	1.676	-3.15	38.63	6.253	30.41	6.41	30.53	6.231	45.0	6.431	49.24	6.418	35.71	6.385	49.6	6.449
	5846.986	1.676	-3.21	23.29	6.017	19.29	6.236	20.53	6.09	28.38	6.21	30.43	6.157	22.39	6.188	33.95	6.251
	5748.346	1.676	-3.26	28.42	6.193	22.36	6.373	–	–	33.67	6.374	–	–	24.43	6.294	36.84	6.364

	6128.963	1.676	-3.33	25.97	6.184	20.33	6.367	20.26	6.186	31.53	6.377	34.14	6.334	21.23	6.261	36.57	6.403
	6767.768	1.826	-2.17	78.94	6.122	74.29	6.325	–	–	–	–	–	–	80.83	6.3	93.74	6.385
	6177.236	1.826	-3.5	13.77	6.154	10.98	6.358	–	–	17.26	6.347	19.21	6.31	11.82	6.269	20.82	6.373
	5754.655	1.935	-2.33	74.12	6.395	68.12	6.564	73.16	6.475	85.24	6.627	83.04	6.527	73.38	6.525	86.08	6.628
	6370.341	3.542	-1.94	13.37	6.251	12.66	6.439	–	–	20.53	6.531	16.51	6.353	12.52	6.347	17.84	6.407
	6842.035	3.658	-1.48	23.78	6.196	22.79	6.377	23.75	6.279	32.77	6.44	29.41	6.315	24.41	6.331	33.59	6.418
	6176.807	4.088	-0.26	62.48	6.161	64.01	6.372	64.73	6.277	74.79	6.398	71.56	6.305	66.65	6.324	75.28	6.395
	6111.066	4.088	-0.87	34.04	6.257	35.09	6.461	38.58	6.421	42.8	6.462	40.78	6.38	37.48	6.427	42.84	6.434
	6204.6	4.088	-1.1	21.49	6.198	22.58	6.41	23.23	6.319	28.58	6.409	28.4	6.357	23.98	6.368	30.63	6.419
	6175.36	4.089	-0.559	48.4	6.219	51.43	6.455	57.24	6.45	62.76	6.501	58.01	6.379	53.47	6.405	58.49	6.409
	5760.828	4.105	-0.8	33.33	6.203	32.7	6.373	36.88	6.349	45.33	6.468	40.81	6.34	35.42	6.347	44.12	6.418
	6223.981	4.105	-0.91	29.89	6.223	29.3	6.392	29.42	6.287	37.3	6.411	35.86	6.337	30.4	6.337	38.29	6.4
	6186.709	4.105	-0.96	31.48	6.308	30.73	6.474	–	–	–	–	–	–	32.7	6.436	39.76	6.479
	6230.09	4.105	-1.26	20.34	6.342	21.26	6.55	23.48	6.499	25.19	6.507	27.29	6.507	22.03	6.494	29.4	6.568
	6378.247	4.154	-0.83	31.93	6.226	33.22	6.432	32.3	6.307	40.78	6.435	37.67	6.333	33.31	6.355	42.51	6.44
	5805.213	4.167	-0.64	40.8	6.245	40.52	6.419	41.17	6.326	47.93	6.41	49.31	6.391	42.14	6.368	51.83	6.455
	6598.593	4.236	-0.98	24.83	6.288	25.5	6.479	26.81	6.406	35.44	6.553	33.6	6.473	26.67	6.431	35.27	6.52
	6130.13	4.266	-0.96	22.71	6.262	21.08	6.394	20.97	6.289	30.91	6.489	27.64	6.373	23.01	6.37	30.98	6.459
	6635.118	4.419	-0.82	24.34	6.288	23.84	6.442	22.09	6.3	32.79	6.511	31.49	6.443	25.61	6.413	32.79	6.482
Cu I	5782.127	1.642	-1.72	77.4	4.46	63.08	4.481	67.35	4.368	83.97	4.605	88.92	4.64	68.61	4.442	88.83	4.686
Zn I	4722.153	4.03	-0.338	69.25	4.463	74.14	4.615	–	–	–	–	–	–	74.11	4.56	74.89	4.641

Table 3.3: Synthesized HFS Line Abundances. Listed synthesized abundances replace EW abundances from Table 3.2

Ion	λ (Å)	χ (eV)	log gf	Solar $\log N_\odot$	Pr0201	Pr0133	Pr0208	Pr0081	Pr0051	Pr0076
Co I	6814.942	1.956	-1.9	–	5.07	–	–	–	–	–
	5301.039	1.71	-2.0	–	–	–	–	–	–	–
Mn I	5432.546	0.0	-3.795	5.28	5.46	–	–	–	5.41	5.55
Sc II	6604.601	1.357	-1.309	3.10	3.18	3.09	3.25	3.15	3.17	3.27
	6245.637	1.507	-1.03	3.10	3.23	3.09	3.25	3.15	3.16	3.17
V I	6111.645	1.043	-0.715	–	–	–	–	–	–	4.05
	6090.214	1.081	-0.062	3.83	4.03	–	–	–	–	4.05

3.2.4 User Guided Equivalent Width Measurements

The EW measurement of absorption lines is performed by an in-house user guided code called eXtract from SPECTra - Equivalent Widths (XSpect-EW), specifically created for this purpose. The general process for measuring EWs of absorption lines for abundance derivations includes three main steps: normalization of the continuum, wavelength shift, and fitting the absorption lines with Gaussian or Voigt profiles to determine the EW of the lines. Each step of the process can be vulnerable to user error if done manually, as detailed in the following subsections, depending on how much care and time is given to each part of the analysis. Ideally, one would take extreme care in each of these parts within a minimal amount of time.

3.2.4.1 Continuum Normalization

Arguably the most important part of the EW measuring process is the ability to consistently determine the continuum of the spectrum or each spectral order. The differential Curve of Growth (CoG) abundance determination involves comparing the abundances of the star of interest to those of a standard or reference star,

often the Sun; therefore, one must be able to determine the continuum in each spectral order in the same way for the star and the standard so as to minimize differences in the abundances that could arise as a result of the analysis. XSpect-EW has been designed to normalize the spectrum efficiently and accurately by using a two-step process.

Step 1: a spectrum is split into smaller pieces (referred to as selection windows), the size of which is set to larger than the typical size of the absorption lines to ensure that the selection windows do not fall entirely within a line. For example, in an optical high resolution Keck/HIRES spectrum with R>60k, the width of a typical line will be 0.4–0.6 Å, so the size of the selection window could be ∼1.6 Å. Points above 90% of the flux values within a selection window are chosen as points in the continuum (90% value can be adjusted by the user if needed).

Step 2: the chosen continuum points are used to normalize the spectrum by fitting them with a Gaussian Process (GP). A GP is a collection of random variables, any finite number of which have a joint Gaussian distribution. GPs are useful for data containing non-trivial stochastic signals or noise. A square exponential kernel (or Gaussian kernel) $k_{SE}(x,x') = A\exp[-\Gamma(x-x')^2]$ is used for the covariance function in the GP where A is the variance and Γ is the inverse lengthscale ($\Gamma = (1/2l^2)$). A variance of similar order of magnitude as the flux values is used (10^7), along with an inverse lengthscale of 0.1. After testing various values, these gave the best results for our spectra. XSpect-EW will be updated to automatically determine the variance and lengthscale values for each order in a spectrum and to have a variety of kernels available. The flux is then divided by the curve output by the GP (grey curve in Fig. 4.1 top panel) which normalizes the order (Fig. 4.1 bottom panel).

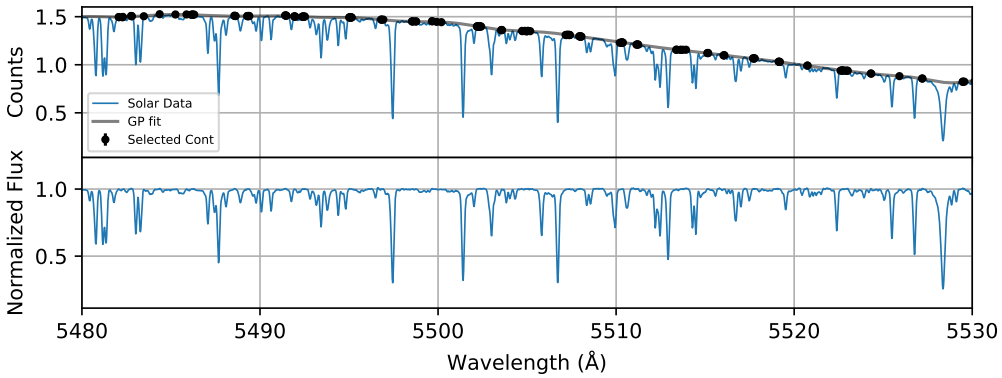

Figure 3.3: Sample section of an order within the observed solar spectrum before and after normalization. Black points are those selected as part of the continuum; black curve is the output of the Gaussian Process.

3.2.4.2 Wavelength Shift

Once normalization is complete, each order is wavelength shifted to the rest frame. This can be done manually by visually identifying a portion of an order in the observed spectrum, comparing it to a reference spectrum, and using software to shift the wavelength axis by the appropriate amount. Errors in this part of the process can lead to measuring the wrong lines within an order, which may show up as abundance outliers or result in higher than expected abundance errors later in the analysis.

XSpect-EW makes use of a simple χ^2 minimization approach to this problem. An input spectrum is shifted to match a solar spectrum order by order. This is done by determining the median wavelength value in the order of the spectrum to be shifted, finding which order in the solar spectrum this value falls, and shifting the order to match the solar spectrum. The shift is determined by evaluating χ^2 between both orders for a range of wavelength shifts from -5 Å to +5 Å in steps of 0.1 Å and selecting the shift with the minimum χ^2 value (shift ranges and resolution can be changed by user if needed). In cases where a shift cannot be determined for an order, the shifts for other orders are used to predict the shift of the missing order by linear interpolation of the shift values. A user may also manually shift any order by a specified amount for further correction if needed.

3.2.4.3 Equivalent Width Measurements

Measuring the EW of an absorption line generally involves fitting a Gaussian or Voigt function to the line and then integrating that function to determine the area enclosed by the curve and continuum. XSpect-EW uses a four step process for this.

Step 1: the extent of the line being measured is determined. Carefully determining the extent, or width of the line at the continuum, is critical to obtaining an accurate measure of the absorption in the line. A piece of the spectrum around a selected line is trimmed from the rest of the spectrum (default set to 1.5 Å about the line center). The boundaries of the line being measured are determined by utilizing the slope of the flux values within the piece of the spectrum. These values range from a maximum or minimum near the center of the line to zero at the continuum and the core, as shown in Figure 3.4. Using one half of the standard deviation of the flux slope values, a range of values centered on the continuum is created. After testing various values, one half of the standard deviation gave us best results relative to hand-measured EWs. The boundaries of the absorption line are defined as the points where the slope enters this range from the maximum or minimum values to either edge of the line. At this boundary, the slope values approach zero as the flux values approach the constant continuum.

Step 2: with the boundaries defined, XSpect-EW assumes the continuum is correct and shifts the data outside the boundaries of the line (still within the 1.5 Å line window) to match the continuum, effectively

isolating the line to be measured.

Step 3: the isolated absorption line and associated continuum is fed into another GP (same kernel) with a small variance of 1 and large inverse lengthscale of 100.

Step 4: the GP can produce different realizations of the data, and XSpect-EW uses this to perform a Gaussian fit to the line, repeating the process 100 times and thus producing 100 different EW measurements. The mean and standard deviation are calculated using the 100 measurements of the line. Each absorption line can be plotted and remeasured if needed, with the ability to adjust the local continuum, center of the line, and boundaries of the line.

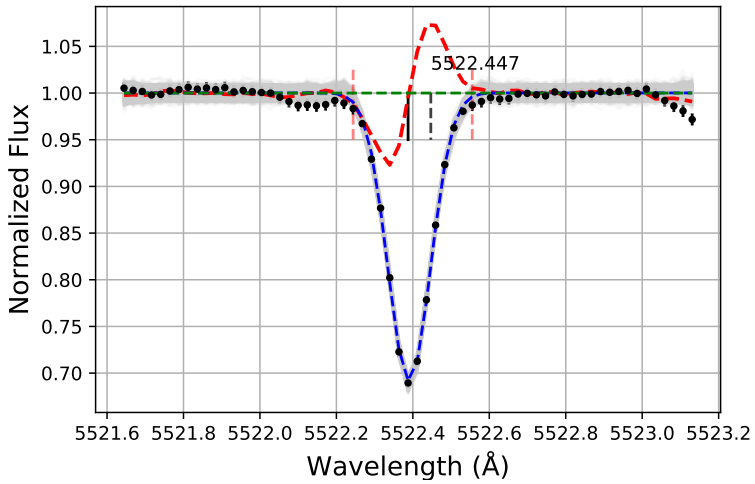

Figure 3.4: Sample plot for an Fe I line (5522.447Å) from the solar spectrum. Black dots with error bars correspond to data; grey shading shows the 1σ variance, blue curve is the Gaussian fit. Green horizontal line defines the continuum. Red curve shows the slope of the flux values (shifted to the continuum). Red vertical lines establish the boundaries of the line measured. Dashed black vertical line is the input wavelength of the line, solid vertical line is the best fit wavelength of the line.

3.2.4.4 Verification of Methodology

To verify the robustness of our new EW measuring tool, in Figure 4.5 we compare EWs of Fe I and Fe II lines measured in our solar spectrum with XSpect-EW and by hand with SPECTRE, a spectral analysis package (Sneden et al., 2012). All differences are $< 15\%$, with 80% of Fe lines having differences smaller than 5%. In the remaining elemental lines (not shown here), $\sim$70% of lines have differences smaller than 5%. XSpect-EW requires some user input to obtain these measurements which consists of checking each automatic line fit and remeasuring problematic lines by adjusting extra parameters that characterize the absorption line. We note that this interactive functionality has been purposely built into XSpect-EW for this specific purpose. The scatter in the fractional difference of the line measurements is larger for the other elements, because those lines can generally be more difficult to measure due to the variety in the strength of the lines and proximity to

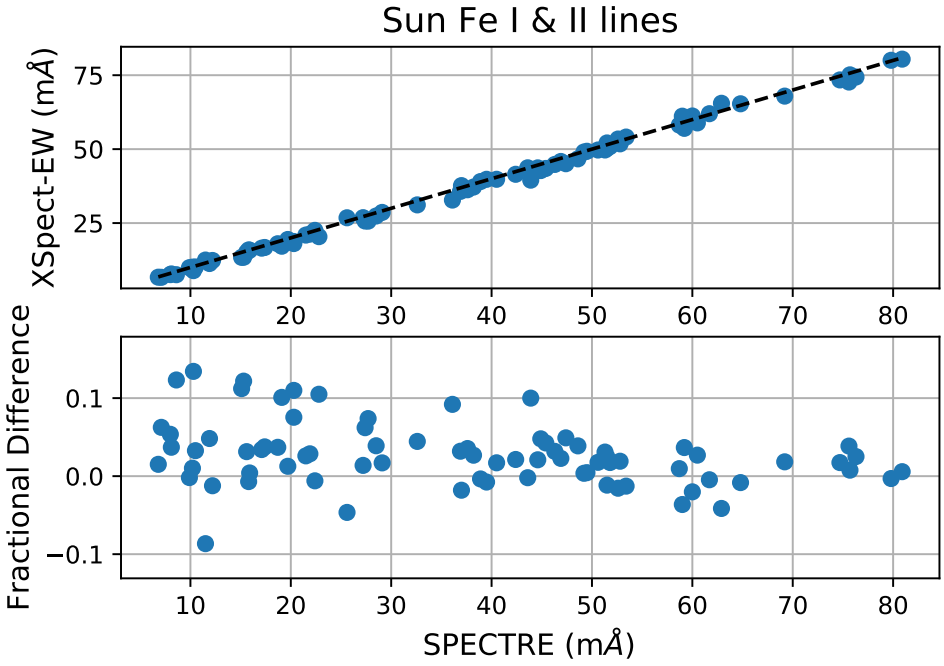

Figure 3.5: Top panel: XSpect-EW measured lines (with some user input) plotted against hand measured EWs in SPECTRE. Dashed line is the one-to-one line. Bottom panel: Fractional difference ([XSpect-EW − hand] / hand) between XSpect-EW and hand measured values.

other lines. A well curated line-list can be helpful for automatic line fits as strong, isolated absorption lines are easier for XSpect-EW to measure automatically. The quality of the data will also be a deciding factor in the number of lines that need to be remeasured. In this example, 17% of Fe lines and 23% of other elemental lines required remeasuring, greatly reducing the amount of time needed to measure all lines and allowing the user to focus on problematic lines to produce abundances with high precision. Lines that are remeasured are only considered based on visual inspection of the fit, not in comparison to previous measurements, since when measuring a new star no comparison would be available. The average of the Fe absolute abundances derived from the XSpect-EW and SPECTRE EWs, shown in Figure 4.6, agree within errors and agree with the input solar absolute abundance within MOOG of 7.50 dex. For all Fe I and II lines, we see a smaller scatter in the absolute abundances from the XSpect-EW measurements than in the SPECTRE measurements by 0.01 dex. From this we can see that XSpect-EW performs as well, if not slightly better, than a full set of hand-measured EWs from SPECTRE.

From the FeI and FeII abundances derived using the EWs measured with XSpect-EW, we determine an average cluster metallicity for Praesepe of 0.21 ± 0.02 dex, which is in good agreement with most past works on the cluster metallicity. In Table 4.1, we show the literature stellar parameter values for each star along with our own derived values. Our derived stellar parameters ($T_{\rm eff}, \log G, [Fe/H]$) are also in good agreement with

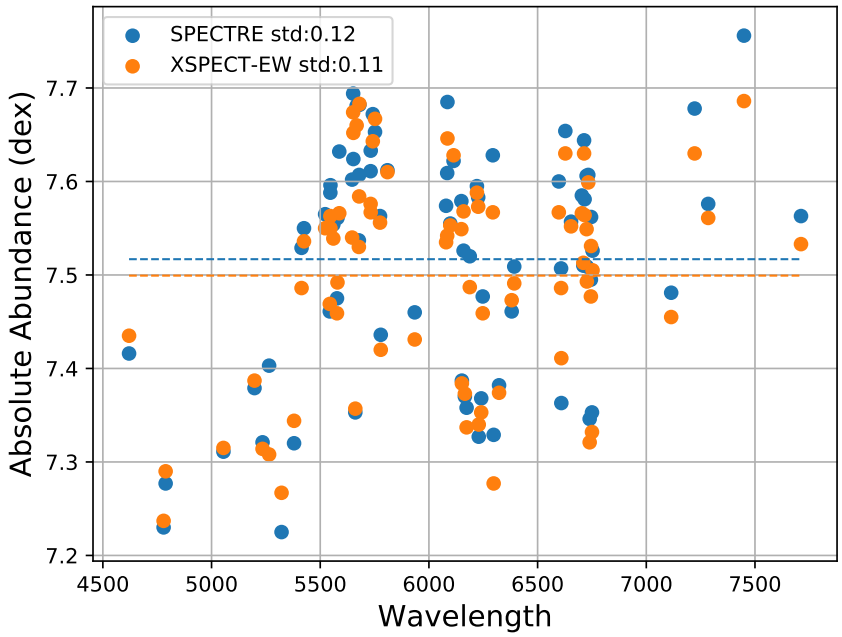

Figure 3.6: Output absolute abundances from Solar FeI and FeII lines shown in Figure 4.5 using MOOG. Blue points represent abundances from SPECTRE measurements while orange points represent abundances from XSpect-EW. The dashed lines (same colors used as for points) show the average abundances for each method.

Table 3.4: Comparison to Literature

Star ID alt ID	T_{eff} K	log G $\log(g \cdot cm \cdot sec^{-1})$	ξ km/s	[Fe/H] dex	Reference
Pr0201	6168 ± 35	4.34 ± 0.10	1.52 ± 0.06	0.23 ± 0.05	This work
Prae kw 418	6174 ± 50	4.41 ± 0.10	—	0.19 ± 0.04	Quinn et al. (2012)
	6062 ± 110	4.44 ± 0.07	1.27 ± 0.18	0.24 ± 0.10	Pace et al. (2008)
Pr0133	6067 ± 60	4.18 ± 0.12	1.74 ± 0.11	0.19 ± 0.06	This work
Prae kw 208	6005 ± 19	4.46 ± 0.21	1.05 ± 0.04	0.18 ± 0.03	Gebran et al. (2019)
	5997 ± 60	4.38 ± 0.20	1.40 ± 0.20	0.12 ± 0.10	Boesgaard et al. (2013)
	5993 ± 110	4.45 ± 0.07	1.52 ± 0.18	0.28 ± 0.10	Pace et al. (2008)
Pr0208	5869 ± 46	4.37 ± 0.13	1.53 ± 0.07	0.26 ± 0.07	This work
N2632-8	5977 ± 75	4.55 ± 0.15	1.30 ± 0.20	0.25 ± 0.11	D'Orazi et al. (2020)
Prae kw 432	5841 ± 73	4.40 ± 0.20	1.25 ± 0.20	0.17 ± 0.10	Boesgaard et al. (2013)
Pr0081	5731 ± 42	4.44 ± 0.11	1.41 ± 0.06	0.18 ± 0.06	This work
CPrae kw 30	5716 ± 45	4.57 ± 0.42	1.18 ± 0.04	0.12 ± 0.04	Gebran et al. (2019)
	5675 ± 111	4.44 ± 0.20	1.07 ± 0.20	0.12 ± 0.10	Boesgaard et al. (2013)
Pr0051 TYC 1395-668-1	6017 ± 27	4.40 ± 0.07	1.54 ± 0.05	0.16 ± 0.03	This work
Pr0076	5748 ± 24	4.44 ± 0.07	1.35 ± 0.03	0.22 ± 0.05	This work
Prae kw 23	5773 ± 53	4.56 ± 0.24	1.20 ± 0.04	0.20 ± 0.04	Gebran et al. (2019)
	5699 ± 79	4.43 ± 0.20	1.10 ± 0.20	0.12 ± 0.10	Boesgaard et al. (2013)

current literature values. The main discrepancy between our stellar parameters and literature values comes from the ξ parameter values which in general are larger than literature values, likely due to the higher ξ value adopted for the Sun in this work (1.38 km/s here, compared to lower values used in other studies)(Pace et al., 2008; Gebran et al., 2019; D'Orazi et al., 2020). A more detailed comparison of individual stars to the literature is presented in section 3.3.2.

3.3 Results

3.3.1 Derived Stellar Abundances

The derived elemental abundances for our targets are summarized in Table 3.5. Elements with only one measured absorption line have no mean and therefore no uncertainty in the mean; for those lines we have adopted the total error to be the average total error of all other elements in the star. Some elements in some stars were not measurable due to lack of spectral coverage or removal of lines that were not measurable (due to noise, blending, bad fit...etc). The errors for all stellar parameters and abundances are symmetric or close to symmetric (where $\pm\sigma_{Total}$ intervals are equal or close to equal); in all cases we conservatively adopt the larger error, except with surface gravity where we adopt the average error. The resulting differences between the archive data (2003) and our data (2013) for Pr0076 are within error bars for the derived stellar parameters and elemental abundances, as shown in Table 3.5. Despite the fact that we are using data of differing quality, observing conditions, instrument setup, and time of observation we are able to produce consistent results

Table 3.5: Stellar Abundances. $^{b}\sigma_{\mu}$– the uncertainty in the mean. $^{c}\sigma_{Total}$– quadratic sum of σ_{μ} and uncertainties due to $T_{\rm eff}$, $\log g$, and ξ.

	Pr0201	Pr0133	Pr0208	Pr0081	Pr0051	Pr0076 (2003)	Pr0076 (2013)
[C/H]	$0.12 \pm 0.03^{b} \pm 0.05^{c}$	$0.02 \pm 0.03 \pm 0.06$	$0.12 \pm 0.06 \pm 0.09$	$0.13 \pm 0.03 \pm 0.05$	$0.07 \pm 0.03 \pm 0.04$	$0.10 \pm 0.07 \pm 0.09$	$0.03 \pm 0.01 \pm 0.04$
[O/H]	$0.11 \pm 0.03 \pm 0.05$	$0.07 \pm 0.03 \pm 0.07$	$0.09 \pm 0.05 \pm 0.08$	$0.10 \pm 0.09 \pm 0.11$	$0.05 \pm 0.03 \pm 0.05$	...	$0.07 \pm 0.04 \pm 0.05$
[Na/H]	$0.19 \pm 0.02 \pm 0.03$	$0.12 \pm 0.04 \pm 0.05$	$0.22 \pm 0.04 \pm 0.03$	$0.09 \pm 0.03 \pm 0.04$	$0.13 \pm 0.01 \pm 0.02$	$0.27 \pm ... \pm 0.08$	$0.20 \pm 0.03 \pm 0.03$
[Mg/H]	$0.14 \pm 0.01 \pm 0.03$	$0.18 \pm ... \pm 0.05$	$0.23 \pm 0.03 \pm 0.05$	...	$0.12 \pm 0.01 \pm 0.02$	$0.20 \pm 0.24 \pm 0.24$	$0.21 \pm 0.01 \pm 0.05$
[Al/H]	$0.12 \pm ... \pm 0.05$	$0.11 \pm ... \pm 0.05$	$0.20 \pm 0.00 \pm 0.02$	$0.11 \pm 0.01 \pm 0.02$	$0.14 \pm 0.00 \pm 0.01$	...	$0.19 \pm 0.02 \pm 0.03$
[Si/H]	$0.20 \pm 0.01 \pm 0.01$	$0.15 \pm 0.01 \pm 0.02$	$0.20 \pm 0.01 \pm 0.01$	$0.14 \pm 0.01 \pm 0.01$	$0.12 \pm 0.01 \pm 0.01$	$0.19 \pm 0.02 \pm 0.02$	$0.18 \pm 0.01 \pm 0.01$
[Ca/H]	$0.19 \pm 0.02 \pm 0.03$	$0.17 \pm 0.01 \pm 0.05$	$0.23 \pm 0.02 \pm 0.05$	$0.17 \pm 0.02 \pm 0.04$	$0.16 \pm 0.01 \pm 0.03$	$0.27 \pm ... \pm 0.08$	$0.24 \pm 0.01 \pm 0.03$
[Sc/H]	$0.12 \pm 0.02 \pm 0.05$	$-0.01 \pm ... \pm 0.05$	$0.16 \pm 0.01 \pm 0.07$	$0.05 \pm ... \pm 0.05$	$0.06 \pm 0.01 \pm 0.03$	...	$0.12 \pm 0.05 \pm 0.07$
[Ti/H]	$0.22 \pm 0.01 \pm 0.06$	$0.13 \pm 0.01 \pm 0.06$	$0.24 \pm 0.01 \pm 0.04$	$0.19 \pm 0.03 \pm 0.05$	$0.15 \pm 0.01 \pm 0.04$	$0.24 \pm 0.03 \pm 0.10$	$0.22 \pm 0.02 \pm 0.06$
[V/H]	$0.22 \pm 0.03 \pm 0.05$	$0.28 \pm 0.05 \pm 0.08$	$0.25 \pm 0.02 \pm 0.06$	$0.19 \pm 0.02 \pm 0.05$	$0.16 \pm 0.01 \pm 0.03$	$0.27 \pm 0.03 \pm 0.08$	$0.24 \pm 0.01 \pm 0.03$
[Cr/H]	$0.20 \pm 0.01 \pm 0.03$	$0.21 \pm 0.01 \pm 0.05$	$0.27 \pm 0.03 \pm 0.05$	$0.21 \pm 0.02 \pm 0.04$	$0.19 \pm 0.01 \pm 0.02$	$0.29 \pm 0.01 \pm 0.05$	$0.26 \pm 0.01 \pm 0.02$
[Mn/H]	$0.20 \pm ... \pm 0.04$	...	...	...	$0.13 \pm ... \pm 0.03$	$0.36 \pm 0.01 \pm 0.07$	$0.27 \pm ... \pm 0.04$
[Fe/H]	$0.23 \pm 0.01 \pm 0.05$	$0.19 \pm 0.01 \pm 0.06$	$0.26 \pm 0.01 \pm 0.07$	$0.18 \pm 0.01 \pm 0.06$	$0.16 \pm 0.00 \pm 0.03$	$0.25 \pm 0.01 \pm 0.06$	$0.22 \pm 0.00 \pm 0.05$
[Co/H]	$0.11 \pm 0.01 \pm 0.03$	$0.14 \pm ... \pm 0.05$	$0.27 \pm 0.02 \pm 0.04$	$0.14 \pm 0.01 \pm 0.03$	$0.10 \pm 0.03 \pm 0.04$	$0.18 \pm 0.03 \pm 0.07$	$0.16 \pm 0.02 \pm 0.03$
[Ni/H]	$0.19 \pm 0.01 \pm 0.02$	$0.14 \pm 0.01 \pm 0.04$	$0.21 \pm 0.01 \pm 0.03$	$0.14 \pm 0.01 \pm 0.03$	$0.13 \pm 0.01 \pm 0.02$	$0.24 \pm 0.01 \pm 0.05$	$0.21 \pm 0.01 \pm 0.02$
[Zn/H]	$0.15 \pm ... \pm 0.05$	...	...	...	$0.12 \pm ... \pm 0.03$	$0.18 \pm ... \pm 0.08$	$0.15 \pm ... \pm 0.04$
[S/H]	$0.23 \pm 0.09 \pm 0.09$	$0.20 \pm ... \pm 0.05$	$0.20 \pm ... \pm 0.05$	...	$0.12 \pm 0.02 \pm 0.03$	$0.22 \pm 0.02 \pm 0.05$	$0.20 \pm 0.03 \pm 0.05$
[Cu/H]	$0.02 \pm ... \pm 0.05$	$-0.09 \pm ... \pm 0.05$	$0.14 \pm ... \pm 0.05$	$0.18 \pm ... \pm 0.05$	$-0.02 \pm ... \pm 0.03$	$0.28 \pm ... \pm 0.08$	$0.22 \pm ... \pm 0.04$
[K/H]	$0.34 \pm ... \pm 0.05$	$0.31 \pm ... \pm 0.05$	...	$0.12 \pm ... \pm 0.05$	$0.29 \pm ... \pm 0.03$	...	$0.18 \pm ... \pm 0.04$
[N/H]	$0.06 \pm ... \pm 0.05$	...	...	...	$0.08 \pm ... \pm 0.03$	...	...

giving us great confidence in our analysis.

Fig 3.7 shows the abundance vs atomic number for each star and the cluster mean. Most elements have a similar spread about the mean while some (K, Sc, Co, and Cu) show a larger spread. This larger spread is likely due to the fact that these elements have a low number of lines measured, lines may be weak, noisy, or blended with other nearby lines making them difficult to measure, or some combination of these factors.

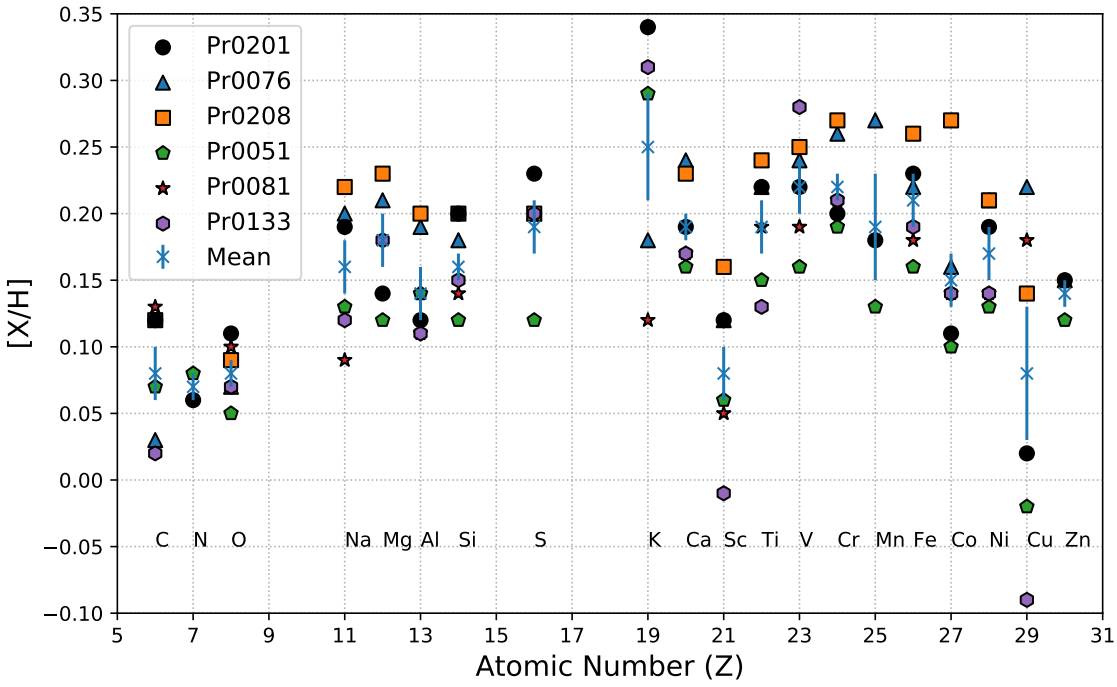

Figure 3.7: Abundances vs. atomic number (Z) for all Praesepe stars (2013 data used for Pr0076). The planet host, Pr0201, is shown as a filled circle. The typical error bar for elements is 0.05 dex (check Table 3.5 for specific errors). The mean for each element is shown in the blue cross along with the error in the mean.

3.3.1.1 Planet-Hosting Star

In order to see if the planet host, Pr0201, is different from the rest of the our sample, we compare the abundances to the cluster mean. Figure 3.8 shows the difference between Pr0201 and the cluster mean (not including the planet host) for each derived element vs atomic number. Most elements fall between ± 0.05 dex of the cluster mean and are within errors of zero with a few exceptions. The element with the largest difference is K having an overabundance of 0.12 dex when compared to the cluster. Si, having the smallest total error of 0.01 dex, is also significantly overabundant in the planet host by 0.04 dex. The planet host shows no obvious trend in abundance vs atomic number over all measured elements.

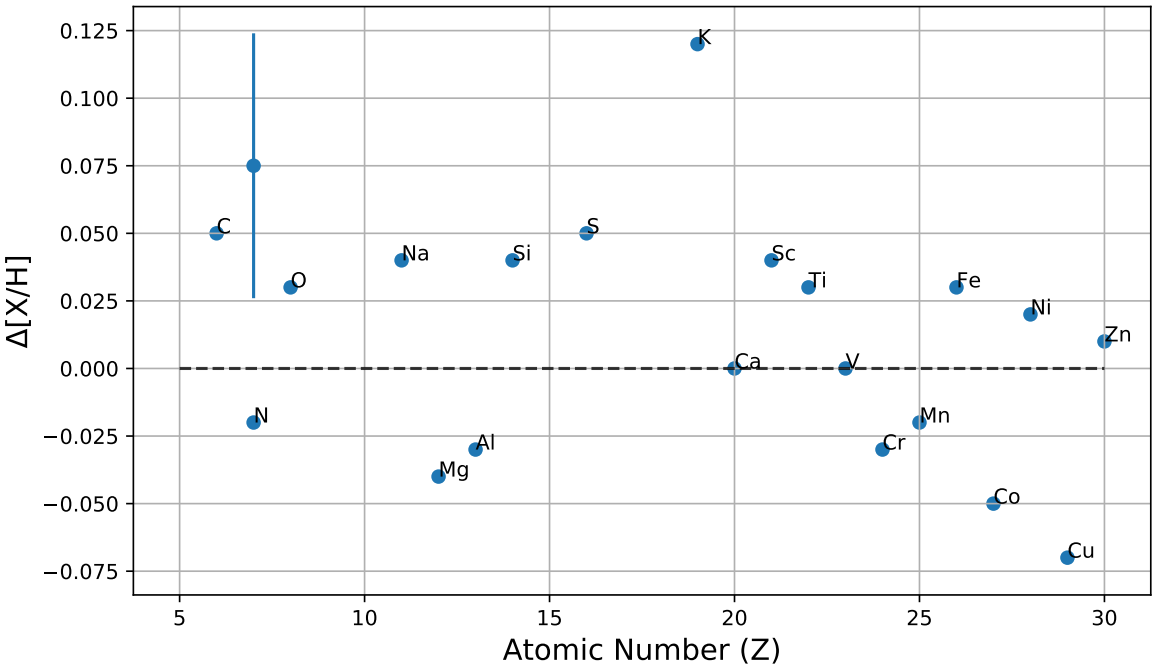

Figure 3.8: Abundance difference between planet host (Pr0201) and cluster mean vs. atomic number for all elements. Dashed line denotes zero difference and the average error is shown in the top left corner, which shows the $\pm 1\sigma$ error with a dot to mark the center.

3.3.1.2 Non Planet-Hosting Stars

In Figure 3.9 we show the difference between each star and the cluster mean (the mean not including that specific star). Elements noted below are considered overabundant or deficient if they are more than 1σ (in actual errors, not average errors) different from zero.

Pr0133 is only overabundant in K by 0.08 dex and deficient in C by 0.07 dex, Ti by 0.07 dex, Sc by 0.11 dex, and Cu by 0.20 dex.

Pr0208 has the highest metallicity of our analysed stars, [Fe/H] of 0.26 dex, and shows an overabundance in many elements: S by 0.04 dex, Ni by 0.05 dex, Ti by 0.06 dex, Cr by 0.06 dex, Na by 0.07 dex, Mg by 0.07

dex, Al by 0.07 dex, Sc by 0.09 dex, and Co by 0.14 dex. While elements of high condensation temperature tend to be overabundant in Pr0208, the high error bars on the volatile elements make it difficult to say if there is any overall trend with condensation temperature.

Pr0081 shows an overabundance in C by 0.06 dex and Cu by 0.13 dex. Deficient elements include: Si by 0.03 dex, Al by 0.04 dex, Na by 0.08 dex, and K by 0.16 dex.

Pr0051 shows no overabundance but many deficiencies: Cr by 0.04 dex, Si by 0.05 dex, Ni by 0.05 dex, Ti by 0.05 dex, V by 0.08 dex, Fe by 0.06 dex, Mg by 0.07 dex, Co by 0.06 dex, S by 0.09 dex, Mn by 0.09 dex, and Cu by 0.11 dex.

Pr0076 shows deficiencies in C by 0.06 dex and K by 0.08 dex while being overabundant in: Cr by 0.04 dex, Na by 0.05 dex, Al by 0.05 dex, Ni by 0.05 dex, Ca by 0.06 dex, Mn by 0.11 dex, and Cu by 0.17 dex.

3.3.2 Comparison to Previous Work

An et al. (2007) determined [Fe/H] of four G type dwarfs in Praesepe through spectroscopy (equivalent width method) and photometry (photometric metallicity). The mean [Fe/H] they determined through spectroscopy ($+0.11 \pm 0.03$) was lower than our determined mean metallicity of 0.21 ± 0.02. The [Fe/H] they determined through photometry ($+0.20 \pm 0.04$) is in much better agreement with our results and most current literature values.

Pace et al. (2008) performed a detailed chemical study of eight elements (Fe, Na, Al, Si, Ca, Ti, Cr, Ni) on 20 solar-type stars in four open clusters, obtaining high resolution (R=100K) and high signal to noise (S/N = 130) data for seven stars in Praesepe (with two overlapping stars; Pr0133 and Pr0201). They measure a higher mean Fe abundance of $+0.27 \pm 0.10$, though still within errors of our mean abundance. For Pr0201, all eight elements agree within errors, while Pr0133 shows less agreement. Half of the elements agree with our results (Ca, Ti, Cr, Fe) while the other half (Na, Al, Si, Ni) are higher in abundance than our measurements. Our Al measurement comes from just one absorption line for Pr0133 with the total error being the average of the other elements, this could mean this error is underestimated. It is unclear why there is such a discrepancy in the other elements. All reported mean abundances relative to Fe are within error bars except for O which is much lower than our determined abundance.

Carrera and Pancino (2011) studied abundances of three giants in Praesepe using the equivalent width method and while they measure a lower mean [Fe/H] abundance of $+0.16 \pm 0.05$ dex, this mean does fall within errors of our determined mean. Many of the other abundances relative to Fe (Al, Ca, Co, Cr, Mg, Na, Ni, Sc, Si, Ti, and V) disagree with our results having higher abundances except in the case of Ti and Ca. This is likely due to the fact that these stars are of different stellar type than ours and the lower measured metallicity would increase the abundance ratios relative to Fe.

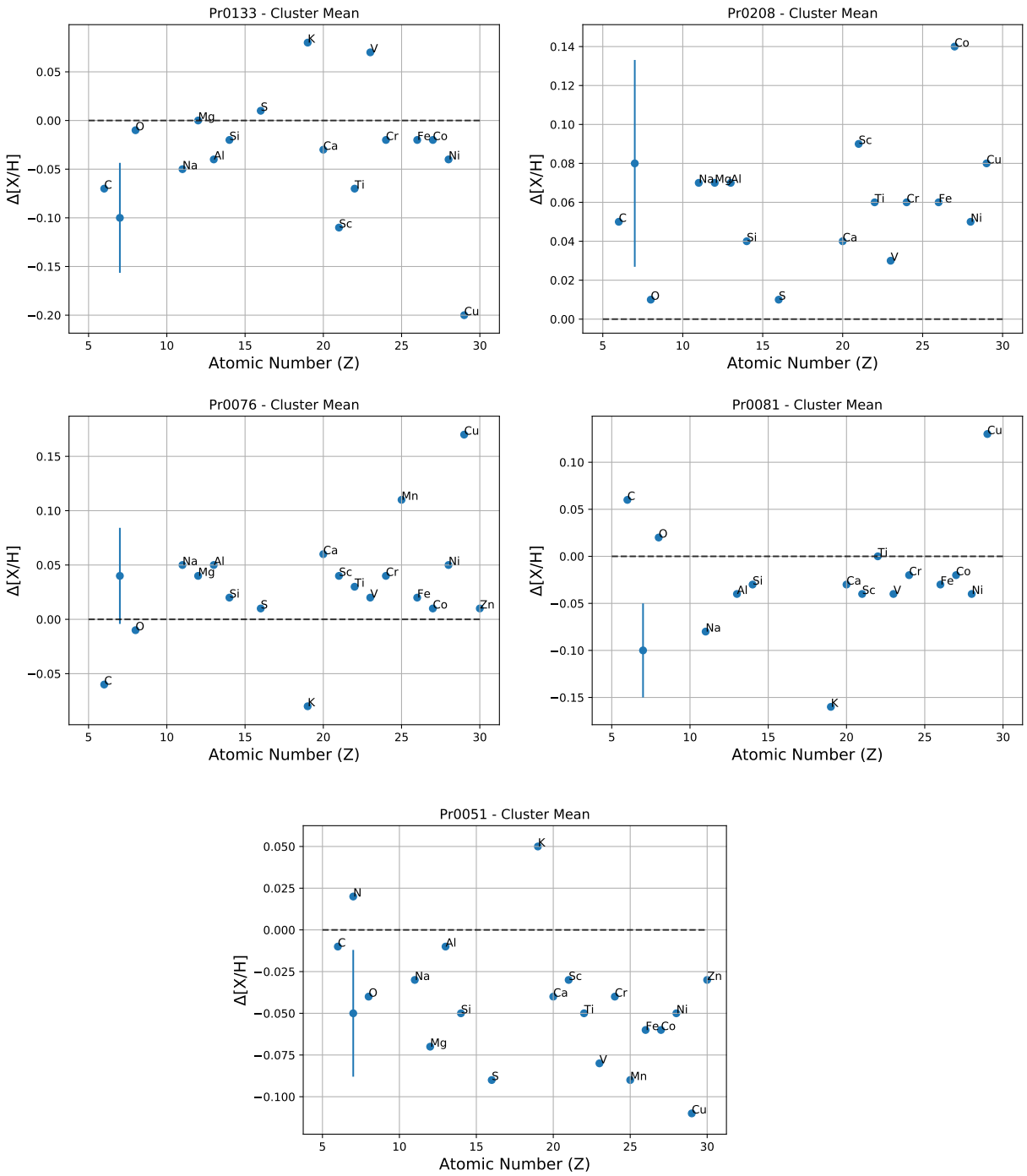

Figure 3.9: Abundance difference between each other star in Praesepe and cluster mean vs. atomic number for all elements. Dashed line denotes zero difference and the average error is shown on the left of each plot, which shows the $\pm 1\sigma$ error with a dot to mark the center.

Boesgaard et al. (2013) presented chemical abundances of 16 elements (Li, C, O, Na, Mg, Al, Si, Ca, Sc, Ti, V, Cr, Fe, Ni, Y, and Ba) for 11 solar-type stars in Praesepe (with four overlapping stars; Pr0133,

Pr0208, Pr0081, and Pr0076) through equivalent width analysis. They determined a mean cluster metallicity of $+0.12 \pm 0.04$ dex, which is lower than our determined mean by 0.09 dex. Abundance ratios for other elements relative to Fe are within 1σ of our measurements except for Al and Sc. In most cases the abundance ratios are higher in value, likely because of the lower mean [Fe/H] abundance. In Pr0133, Pr0208, and Pr0076, our study overlaps with 13 elements (excluding Li, Y, and Ba) while Pr0081 overlaps with 12 elements (excluding Mg as well). For Pr0133, all elements agree within errors except for Sc, which was found to be about solar or higher (0.04$\pm$0.08 dex) while we derived a sub-solar value (-0.20$\pm$0.08 dex). For Pr0208, errors are not reported in this study, but most elements agree within our own erros. Two elements that do not agree within our errors are Sc and Ti; however, if the errors on these elements are at all similar to the errors for the other stars reported in Boesgaard et al. (2013) then it is very likely they would agree with our abundances. Abundances for Pr0081 are also presented without errors and similarly to Pr0208, all derived abundances (Fe, C, O, Na, Al, Si, Ca, Sc, Ti, V, Cr, and Ni) are within our own errors except for Sc. It is also true that if the errors for this star are similar to the other stars, Sc would also fall within the errors. For Pr0076, all 13 elements fall within reported errors.

Gebran et al. (2019) used an automated spectral analysis code (BACCHUS) to determine abundances of 24 elements for five stars in Praesepe (with three overlapping stars; Pr0133, Pr0081, and Pr0076). They report mean abundances for G and K stars separately, $+0.17 \pm 0.04$ and $+0.12 \pm 0.01$ dex respectively. These means are consistent with each other and the literature, the average for G types is consistent with our work. In Pr0133 and Pr0081, our study overlaps with 14 elements (C, O, Na, Mg, Al, Si, Ca, Sc, Ti, V, Cr, Co, Ni, and Cu), all of which agree within errors for Pr0081. For Pr0133, all elements but Na and Cu agree within errors. Our [Na/Fe] abundance is about solar or less (-0.07$\pm$0.07 dex) while Gebran et al. (2019) determined an even lower abundance of -0.35$\pm$0.16 dex. The reverse is true for Cu, our work derived a very low abundance of -0.28$\pm$0.09 dex while Gebran et al. (2019) derived a solar or higher value of 0.02$\pm$0.03 dex. For Pr0076, our study overlaps with 17 elements (Fe, C, O, Na, Mg, Al, Si, Ca, Sc, Ti, V, Cr, Mn, Co, Ni, Cu, Zn), all of which also fall within reported errors.

D'Orazi et al. (2020) revisited the metallicity of Praesepe taking high-resolution spectroscopic observations of 10 solar-type dwarf stars, including Pr0208. All eight elements (Fe, Na, Mg, Al, Si, Ca, Ti, and Ni) studied are within errors of our derived abundances for Pr0208. They report a mean metallicity of $+0.21 \pm 0.01$ dex and conclude that Praesepe is the most metal-rich, young open cluster in the solar neighborhood, in remarkable agreement with our results that also gives confidence in works that report a higher metallicity. Pr0051 has no literature values to be compared to but the general agreement of our results to the literature gives us confidence in those values as well.

Even with similar analyses the literature suggests a large scatter in metallicity for Praesepe, however,

each individual work shows a much lower scatter within their respective sample. The scatter within these works (for [X/Fe]), including our own, is largely consistent with what we would expect from open clusters (Kovalev et al., 2019; De Silva et al., 2007; Bovy, 2016). This implies that the Praesepe cluster is chemically homogeneous and these works may be self-consistent but they may not all be consistent with each other. As our analyses and precision improve, it seems we may converge on a consistent metallicity for Praesepe, perhaps a larger sample analyzed consistently could shed more light on the mean and scatter for the cluster.

3.3.3 Chemical Homogeneity of Praesepe

In Table 3.6 we show the [X/H] and [X/Fe] abundance mean, standard deviation, and error in the mean for our stars in Praesepe. For most of the elements, the [X/Fe] standard deviation and the error in the mean are lower than either for [X/H]. A few exceptions are the elements C, N, O, and Zn which show a lower [X/H] standard deviation and error in the mean. K shows the same standard deviation and error in the mean in both [X/H] and [X/Fe]. The average standard deviation is $\sim$0.01 dex lower in [X/Fe] than [X/H], while the average error in the mean is about the same. In [X/Fe], the standard deviation of most elements is at or below the average $\sim$0.02-0.03 dex, well within literature limits on open cluster abundance scatter (De Silva et al., 2007; Bovy, 2016; Kovalev et al., 2019). With this, we verify that the stars in our sample are chemically homogeneous; a larger sample would be required to confirm the chemical homogeneity of Praesepe as a whole. C and N are above the average by $\sim$ 0.02 dex. K and Cu are much higher than the average by $\sim$ 0.04 and $\sim$ 0.06 dex respectively. Looking at the error in the mean we see a similar separation where most elements are below the average at $\sim$0.01-0.02 dex with elements N, K, and Cu being $\sim$ 0.03 dex higher than the average. C and Mn are above the mean by $\sim$ 0.01 dex or less.

For elements with $Z > 19$ (Ca, Sc, Ti, V, Cr, Mn, Co, Ni, Zn), the scatter in both standard deviation and error in the mean is higher for odd-Z elements (Sc, V, Mn) with the exception of Co which is similar to Ca, Ti, and Cr, but higher than Ni and Zn. This is likely due to the fact that some of these odd-Z elements may have 1-2 synthetically measured absorption lines for each star to account for hfs effects along with lines measured normally where hfs effects are negligible.

3.4 Discussion

Differential abundances studies often compare the abundances of a planet host with that of a wide stellar companion assumed to have formed of the same cloud of material (Ramírez et al., 2011; Tucci Maia et al., 2014; Mack et al., 2014). The resulting differences are attributed to processes occurring after the stars have formed such as planet formation, system evolution, and stellar evolution. Generally, open clusters are assumed to be chemically homogeneous (De Silva et al., 2006; Boesgaard et al., 2013) (which we verify for our sample in

Table 3.6: Abundance Scatter

[X/Y]	Mean	Std	Error in Mean
[C/H]	0.082	0.045	0.02
[C/Fe]	−0.125	0.048	0.021
[N/H]	0.07	0.01	0.01
[N/Fe]	−0.125	0.045	0.045
[O/H]	0.082	0.02	0.009
[O/Fe]	−0.125	0.029	0.013
[Na/H]	0.158	0.047	0.021
[Na/Fe]	−0.048	0.024	0.011
[Mg/H]	0.176	0.041	0.021
[Mg/Fe]	−0.036	0.029	0.015
[Al/H]	0.145	0.037	0.016
[Al/Fe]	−0.062	0.03	0.014
[Si/H]	0.165	0.03	0.014
[Si/Fe]	−0.042	0.009	0.004
[S/H]	0.19	0.037	0.018
[S/Fe]	−0.022	0.026	0.013
[K/H]	0.248	0.084	0.042
[K/Fe]	0.052	0.084	0.042
[Ca/H]	0.193	0.031	0.014
[Ca/Fe]	−0.013	0.02	0.009
[Sc/H]	0.083	0.056	0.025
[Sc/Fe]	−0.123	0.036	0.016
[Ti/H]	0.189	0.04	0.018
[Ti/Fe]	−0.017	0.021	0.01
[V/H]	0.223	0.039	0.018
[V/Fe]	0.017	0.034	0.015
[Cr/H]	0.223	0.03	0.014
[Cr/Fe]	0.017	0.023	0.01
[Mn/H]	0.193	0.058	0.041
[Mn/Fe]	−0.01	0.043	0.031
[Fe/H]	0.207	0.033	0.015
[Co/H]	0.153	0.056	0.025
[Co/Fe]	−0.053	0.38	0.017
[Ni/H]	0.17	0.034	0.015
[Ni/Fe]	−0.037	0.014	0.006
[Cu/H]	0.075	0.112	0.05
[Cu/Fe]	−0.132	0.104	0.047
[Zn/H]	0.14	0.014	0.01
[Zn/Fe]	−0.063	0.017	0.012
$[X/H]_{avg}$		0.043	0.021
$[X/Fe]_{avg}$		0.035	0.018

section 3.3), here we have the rare opportunity to compare our planet host Pr0201 with not just one stellar companion, but five other stars that formed from the same cloud with no known planets.

3.4.1 Abundance Trends and Condensation Temperature

In the search for planet formation signatures we specifically focus on trends in refractory elements with $T_C > 900$K (Meléndez et al., 2009). During early disk evolution, elements with high T_C are expected to condense into solids at shorter distances from the host star, leading to refractory-poor gas and refractory-rich planetesimals. This results in two possible abundance signatures for the host star. The removal of these elements from the protoplanetary disk allows the accretion of the refractory-depleted material onto the host star which imparts a decreasing trend in the refractory elements with T_C. Alternatively, accretion of refractory-rich planetesimals or planets themselves would impart an increasing trend.

In this section we interpret condensation temperature trends in the context of a planet engulfment model, explained in Mack et al. (2014), based on the addition or removal of material with similar composition as the Earth to/from the convection zone of a solar-type star. The composition of the Earth is taken from McDonough (2001) and solar composition is from Asplund et al. (2009). We adjust the size of the convection zone based on the temperature of the star according to Pinsonneault et al. (2001). Solar abundances are modified to match those of the cluster mean (excluding Pr0201) then we can adjust the number of $M_\oplus$ accreted/sequestered in order to produce a desired T_C slope.

Figure 3.10 shows the T_C trend for refractory elements of the cluster mean. Here, we have excluded the planet host, Pr0201, to show that the mean cluster abundances alone present no trend with condensation temperature. The cluster mean abundances show a slope of $-5.98 \times 10^{-6} \pm 3.25 \times 10^{-5}$dex/K consistent with zero slope. When comparing each other star with the cluster mean (excluding that star and the planet host in the mean), no star shows a statistically significant trend in refractory elements with condensation temperature (slopes shown in Fig 3.11).

We will take a closer look at Pr0201, because it is the only known planet-host in our sample. Figure 3.12 shows the T_C trend for refractory elements in the planet host Pr0201 relative to the cluster mean. The best fit line to these elements gives a negative slope of $-8.64 \times 10^{-5} \pm 6.59 \times 10^{-5}$dex/K. While not a statistically significant detection (1.3σ), if taken at face value, this trend could be explained by the sequestering of $\sim$1.62 $M_\oplus$ of material from the convection zone of Pr0201.

Our T_C slope results are relative to solar abundances ([X/H]), meaning a slope consistent with zero tells us the distribution of abundances with respect to T_C is similar to that of the sun. Results for the cluster mean T_C slope are consistent with zero slope meaning the cluster abundance distribution may be similar to the sun. This could indicate that planet-formation for sun-like stars in the cluster is common or that the cluster

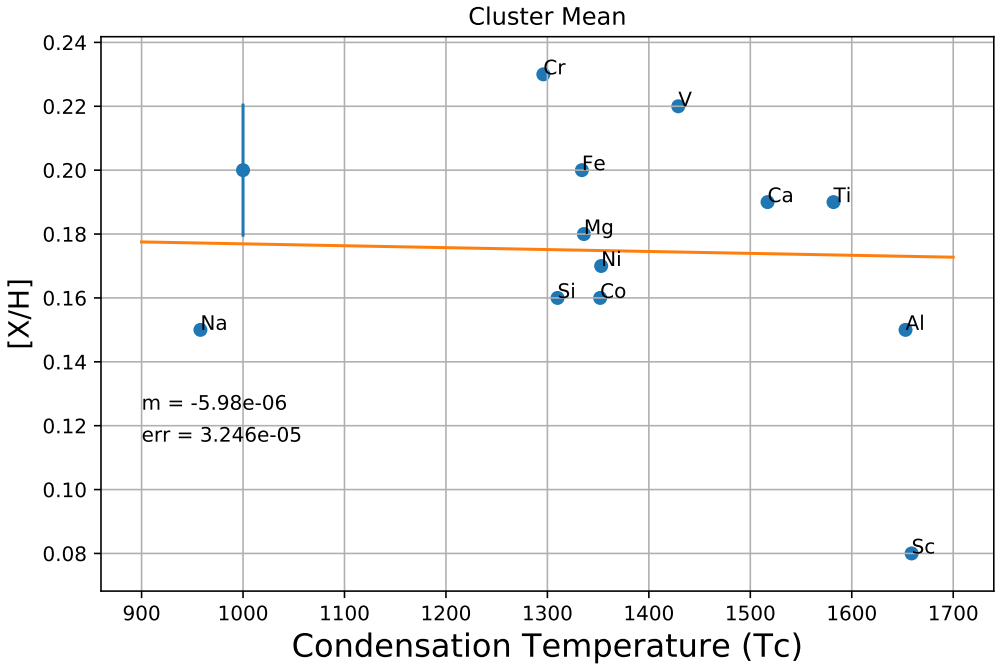

Figure 3.10: Cluster mean vs. condensation temperature (T_C) for refractory elements excluding the planet host Pr0201. The average error is shown on the top left, which shows the $\pm 1\sigma$ error with a dot to mark the center.

initially formed from a cloud with this distribution already in place. The possible discovery of more planets within the cluster could give more weight to the prominent planet-forming case. All six of our analyzed stars, including the known planet-host, show a slope consistent with zero when compared to the cluster mean. If planet formation is in fact prevalent, the lack of detected planets in our sample could be due to the difficulty of finding smaller planets or these systems may have lost their planets entirely.

3.4.2 Limits on Chemical Signatures of Planet Ingestion in Pr0201

The Pr0201 system is host to a short period (4.4264 $\pm$ 0.0070 days) gas giant (Pr0201b) with a minimum mass of 0.54 $\pm$ 0.039 M_J in a circular orbit (Quinn et al., 2012). With such a close-in giant planet and a T_C slope consistent with zero, we investigate the possibility that Pr0201 could have accreted or sequestered refractory-rich material during the planet formation process. Using our planet engulfment model mentioned above, we can place limits on the amount of this material. To do this, we assume Pr0201 formed with the same composition as the cluster mean, starting off with zero slope in the refractory elements. We then add material with the same composition as the Earth until we produce a significant T_C slope (3σ using the measured error in the T_C slope for Pr0201) in the refractory elements (shown in the top panel of Figure 3.13). In order to produce a statistically significant T_C slope, Pr0201 would have needed to accrete 4.42 $M_\oplus$ of material. In the

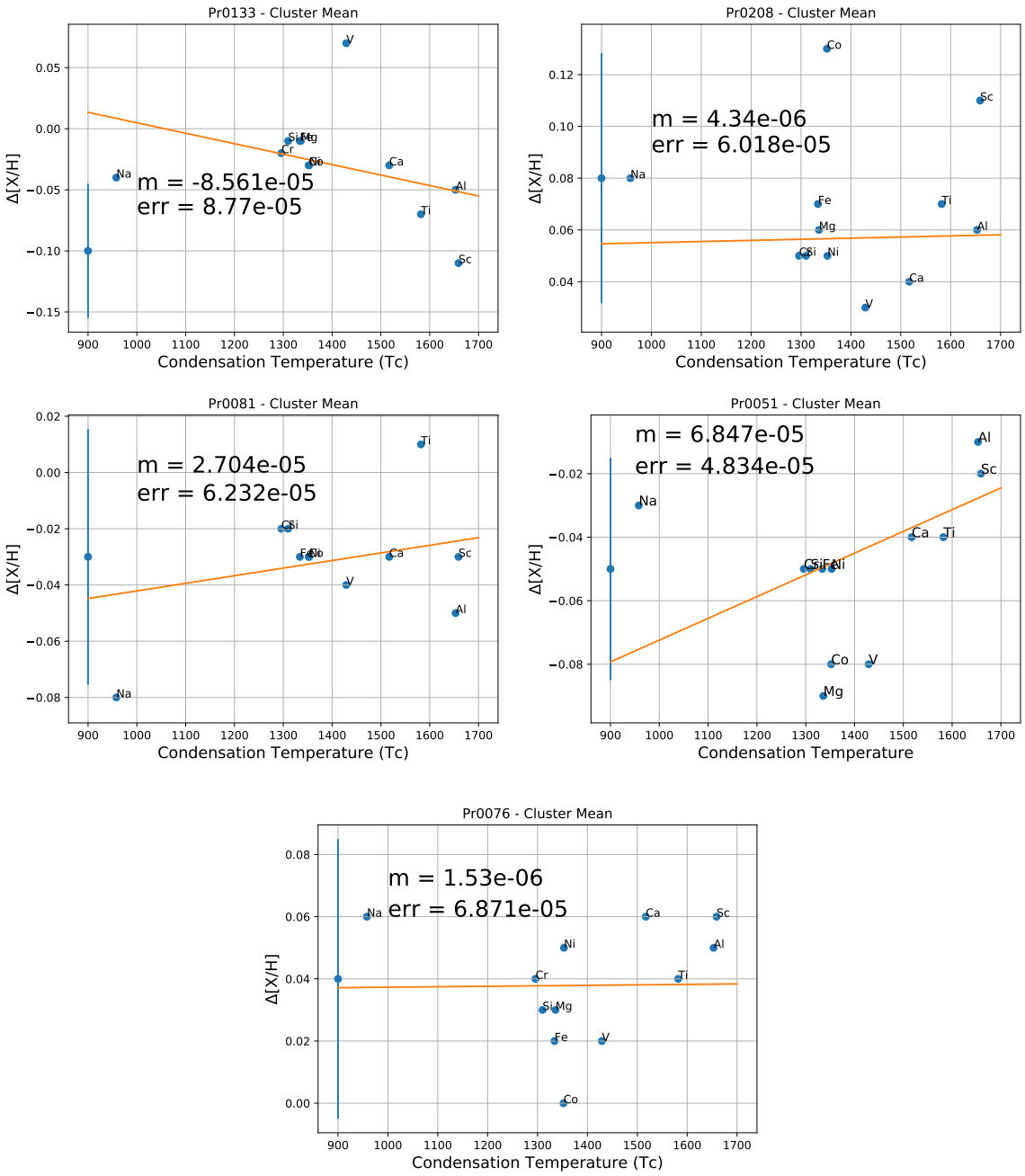

Figure 3.11: T_C trend between each other star and cluster mean for refractory elements. The average error is shown on the left of each plot, which shows the $\pm 1\sigma$ error with a dot to mark the center.

bottom panel of Figure 3.13, we show how this would affect the individual refractory elements of the cluster mean, depicted by the orange points and lines, which can be compared to the abundances of Pr0201 in purple. The solid lines show the mean abundance while the dashed lines show $\pm$ the error in the mean. This accretion scenario would produce abundances that are noticeably enhanced compared Pr0201 and can be ruled out at

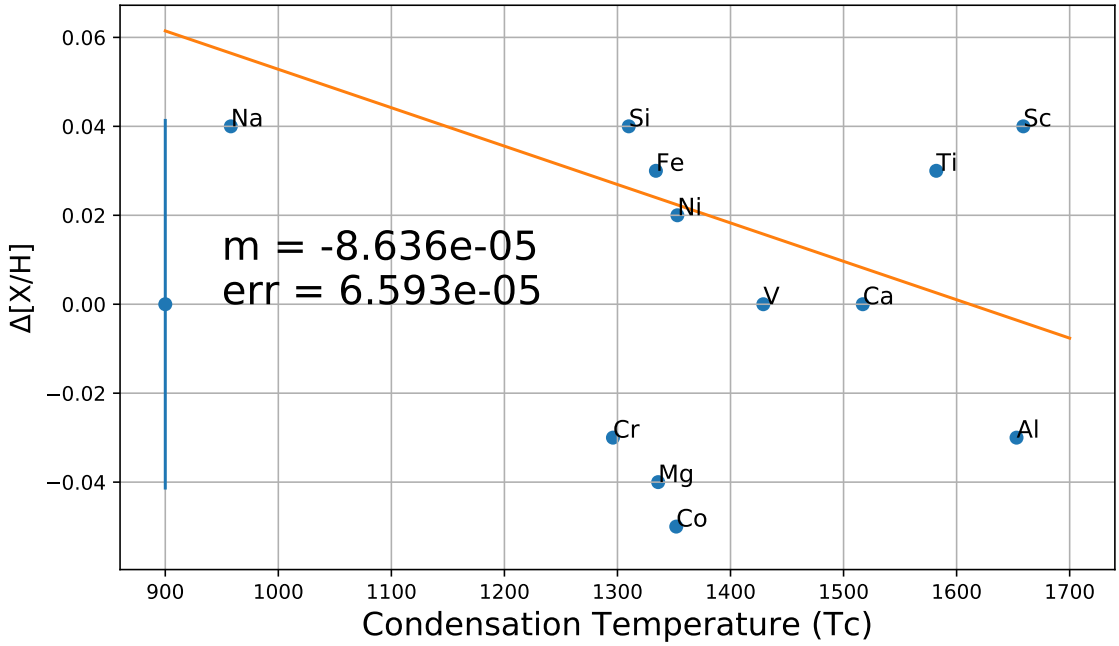

Figure 3.12: T_C trend of the difference between planet host, Pr0201, and cluster mean for refractory elements. The average error is shown on the left side of the plot, which shows the $\pm 1\sigma$ error with a dot to mark the center.

the $\sim 16.5\sigma$ level. Excluding Ti, V, and Fe, it is also the case that 1.25 $M_\oplus$ of material can be ruled out at the 5σ level, indicated by the green lines. In general, Pr0201 does not seem significantly enhanced in refractory elements when compared to the cluster mean. This analysis focuses on accretion but can also be applied to material sequestered.

3.5 Conclusion

In this work we have used new Keck/HIRES observations combined with KOA spectra of six G or F type stars, one of which hosts a 0.54 M_J giant planet, in the nearby Praesepe Cluster to derive detailed solar-relative elemental abundances with a precision of $\sim$0.05 dex. For each star we determined $T_{\rm eff}$, $\log g$, [Fe/H], ξ (microturbulence parameter), and abundances of up to 20 elements (Table 3.5; Figure 3.7). We verify that our results are in good agreement with the current literature and determine a mean cluster metallicity of $+0.21 \pm 0.02$ dex.

We made use of a new custom-built python code for EW measurements called XSpect-EW. The code automatically normalizes each order, wavelength shifts the orders to the rest frame, and fits a Gaussian profile to each line of interest while allowing the user to edit and rerun any of these processes with specified parameters when necessary. This makes measuring hundreds of lines much faster as many lines can be measured automatically with little user contribution and helps to remove some user error when manually performing

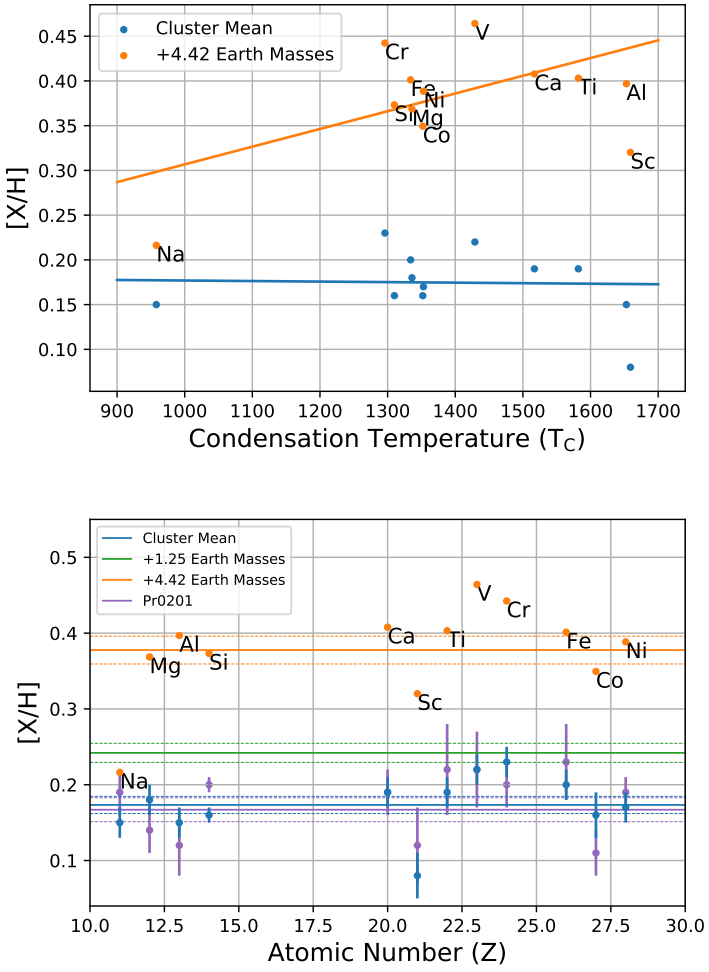

Figure 3.13: Top panel: The refractory cluster mean abundances (excluding Pr0201) are shown in blue vs T_C along with simulated abundances (orange) of the addition of 4.42 $M_\oplus$ to the cluster mean, which would produce a statistically significant slope at the 3 sigma level. Bottom panel: Cluster mean abundances are shown in blue vs atomic number along with the average (solid line) and $\pm$ the error in the mean (dashed lines). Green and orange lines denote the addition of different amounts of $M_\oplus$. Purple points show the abundances for Pr0201, the planet host.

these tasks.

We find no T_C trend in the mean cluster abundances (Figure 3.10). Comparing each star's individual elemental abundances with the cluster mean abundances we see a negative T_C trend in the planet host, Pr0201, of $-8.64 \times 10^{-5} \pm 6.59 \times 10^{-5}$dex/K. According to our planet engulfment model, the slope in Pr0201 corresponds to the sequestering of 1.62 $M_\oplus$ of terrestrial material from the convection zone of the star which could be an indication of terrestrial planet formation, although no terrestrial planets have been detected for this star. We conclude that Pr0201 likely did not accrete a significant amount of Earth-like material.

As mentioned in the introduction, a natural dependence on cluster size and structure is prominent in

determining the strength of the chaotic effects of the cluster environment on planet formation and survival. Praesepe, being an open cluster, contains less mass than a globular cluster, only about $\sim 600 \pm 19\ M_{\odot}$ (Adams et al., 2002). Less mass would dictate fewer O/B stars could initially form, lowering the effect of photoevaporation on disks, stellar winds and supernovae on gas expulsion, and impart a lower average velocity on the cluster members lowering the frequency of stellar encounters. Even in high density environments, short period planets can survive throughout the lifetime of the cluster (Cai et al., 2019). Cluster environmental effects on planet survivability are still not completely understood; however, the current picture painted by recent studies is one of planet formation being common and most of them surviving the evolution of the cluster (albeit in smaller sized systems or as free-floating planets, most of which are expected to escape the cluster; e.g., van Elteren et al., 2019). Combined with the high metallicity of Praesepe, we have reason to believe that planets could be abundant in the cluster. Already, studies have found 13 planets in Praesepe and about 30 total planets in open clusters (Cai et al., 2019). Pfalzner and Vincke (2020) reported that our solar system likely formed in a high-mass extended or intermediate-mass compact association like NGC 6611 or Praesepe, due to roughly 10% of solar-type stars experiencing flyby's after which a solar system analog would remain. As RV surveys become more precise, we expect many more planets will be discovered in nearby open clusters.

The authors acknowledge support by NSF AAG AST-1009810 and NSF PAARE AST-0849736. This research has made use of the Keck Observatory Archive (KOA), which is operated by the W. M. Keck Observatory and the NASA Exoplanet Science Institute (NExScI), under contract with the National Aeronautics and Space Administration. This work makes use of the Radial Velocity Simulator accessed through the Astronomy Education at the University of Nebraska-Lincoln Web Site (http://astro.unl.edu). We thank the LSSTC Data Science Fellowship Program which has benefited this work. George Vejar also thanks Karl Jaehnig for his help and support which benefited this work.

CHAPTER 4

eXtract from SPECTra - Equivalent Widths (XSpect - EW)

This chapter is based on work published in The Astrophysical Journal, 2021, Volume 919, Article ID 100 and provides an overview of the latest version of XSpect-EW[1].

4.1 Introduction

All objects have some temperature and emit radiation (or photons) with a distribution of energies called a blackbody spectrum, as defined by Planck's law. The shape of this distribution of energies is determined by the temperature of the object though, generally, there is a peak of emission with lower energy photons dropping off in a shallow manner towards longer wavelengths while higher energy photons drop off steeply towards shorter wavelengths. As an object increases in temperature, the peak of the distribution shifts towards shorter wavelengths (higher energies) and the emission at all wavelengths increases.

The Sun, and all stars, are generally assumed to be perfect blackbodies. The brightness of a star tells us how much energy is being emitted while the surface temperature tells us how that energy is distributed across the electromagnetic spectrum (EMS). Starlight can then be split up revealing the underlying photon distribution (or spectrum of photon energies) by passing the light through a prism or diffraction grating. Depending on how finely we split the light (depends on spacing between slits of the grating) we can begin to see that the stellar spectrum is not completely smooth. With high enough resolution (fine enough grating), we can see dark lines or wavelengths where photons are not collected as much as at other wavelengths called absorption lines. For the optical or visible part of the EMS, the typical resolution should be $\sim$40,000 $\lambda/\Delta\lambda$ or higher. These lines are formed when the cooler gas at the surface of the star absorbs those specific photon energies as the light passes through the gas and as we detect the rest of the light we obtain an absorption spectrum. The specific photon energies are a direct result of the elements present in the gas and can be used as a fingerprint to identify the elements. Conversely, a hot gas with the same elemental composition will emit the same photon energies instead of absorbing them, resulting in an emission spectrum (like a neon sign).

Once the light has been split into a spectrum, an array of detectors (CCDs) can collect the light at specific wavelengths creating a digitized image of the absorption spectrum. The detector collects photons and will do so for as long as it is exposed to the starlight. A digital image is essentially a detector with a shutter that controls the length of exposure to the photons from the outside world. Telescopes also have a shutter to do the same thing, the longer we keep the shutter open, the more photons we can collect. The level to which we

[1] XSpect-EW has been made publicly available through Github.

fill the detectors is called the continuum of the spectrum, it can be higher if we use a longer exposure time (giving us more photons, but can be expensive and risks over-flowing the detector) or it can be lower if we use a shorter exposure time (giving us less photons which makes the noise more apparent), regardless, the shape of the underlying distribution will be the same.

Spectra can give us information about the physics of an object as well as its composition. The peak of an absorption spectrum can tell us about the temperature, while excess emission in specific areas of the EMS can clue us in to the presence of dust (at longer wavelengths). Absorption and emission lines can be blue or red shifted, which tells us if the object is moving toward or away from us and at what speed. We can also combine stellar models with an observed spectrum to reverse engineer the stellar situation (temperature, surface gravity, metallicity) and abundances of elements that resulted in the observed spectrum, explained below.

Determining stellar parameters and abundances can be done in two main ways. 1) Template matching where synthesized stellar spectral templates are used to match the observed spectrum to determine the best fitting template and in turn obtaining the parameters or abundances used to create the template. 2) Line-by-line EW measurement and Curve of Growth (CoG) method, a meticulous process of measuring the EWs of individual absorption lines in a target star and the sun that uses the CoG to determine abundances from EWs. Both methods have their pros and cons but the CoG method allows for more control over the data and has been used in studies reaching abundance precision down to 0.01 dex (Ramírez et al., 2009). XSpect - EW was originally created to automate and mimic the manual process of the EW measurement in order to eliminate as much human error or inconsistency as possible and to remove tedious and time consuming steps of the process all while conserving the precision by allowing for user adjustments. This software was created by a graduate student so that future graduate students will not have to sit for hours or days clicking three dots to make a Gaussian and instead focus their time on science (also to replace antiquated software used in the manual process).

A number of automated chemical abundance software currently exist. In 2007, ARES was publicly available to the community, a code originally written in C++ and, similarly to XSpect-EW, was created to autonomously mimic the process of manually measuring EWs (Sousa et al., 2007). DAOSPEC (Stetson and Pancino, 2008) is a Fortran code designed to measure EWs with minimal human interaction, although requires some amount of experimentation to arrive at the appropriate hyper parameters for a given spectrum. TAME is a code similar to ARES with some interactivity written in IDL, which requires a license to use (Kang and Lee, 2012). iSpec is a fully automated spectral analysis suite written in Python, with capabilities of using both template matching and EW methods, however comparisons between both methods determined the template matching to be superior in this software (Blanco-Cuaresma et al., 2014). ARES was updated

to ARES v2 (Sousa et al., 2015) in 2015, including new features and Python 3 support through Cython (C Python). ARES v2 is considered simpler to use than other software, however it still requires compiling, the use of non-standard libraries, and a flurry of input parameters.

It is not surprising that as features and tools are added, the general ease of use will in these software decrease. This is where XSpect-EW may differentiate itself. It is very minimal compared to some of these other established pieces of software in what it can do, however, the code is written in Python 3 with easy to access packages that can all be conda installed. XSpect-EW makes use of classes and small functions to organize spectral data in a straight-forward way. It is used in an interactive Python environment so the user has full control over the data, the user can see a clear history of what they have done so far, and they can easily rerun any parts of the process if necessary. Ideally, a user could start up a notebook and have EWs within minutes (following a step by step tutorial available with the code).

4.2 Basic Functioning

XSpect-EW is used to extract equivalent width information from an input absorption spectrum. This is achieved by first loading a Keck fits file (or extracted spectrum as X and Y arrays) into the Spectrum_Data class object. The user can decide on a window_width value (should be larger than width of absorption lines) and a continuum_depth value (depth of noise to include from the continuum, for low noise choose bigger depth value, for high noise choose lower depth value) which are used as inputs for the normalization function. The spectrum is then normalized, order by order, according to the input parameters (normalization can also be performed for a specified wavelength range within an order). If the spectrum needs to be shifted to the rest frame, another spectrum already at the rest frame (solar spectrum or previously wavelength corrected spectrum) can be used as input to the estimate_shift method which will determine the shift autonomously.

The absorption spectrum is now ready to be measured. A line list (with a specific format) can be loaded into the Spectrum_Data object and the loaded lines will be automatically found and measured by fitting a Gaussian function to the absorption line and also producing errors for each line. XSpect-EW provides the option to plot any or all specified lines that are measured for inspection (I suggest only not plotting all lines if they have already been inspected). Specific lines can also be measured and inspected without measuring all lines. Whether measuring all lines at once or specific lines at a time, extra parameters can specified for each measured line to adjust the parameters of each individual Gaussian fit. For well-behaved (high signal-noise) data, the automatic fit will likely be acceptable for most lines, requiring only some lines to be remeasured or adjusted. The check_for_flags method can be useful for quickly flagging lines with high percent error or bad fits (data not matching fit closely). Once lines have been measured and checked, the make_ew_doc method can be used to save the measurements into a text file formatted to work with MOOG.

4.3 Features

4.3.1 Continuum Normalization

Arguably the most important part of the EW measuring process is the ability to consistently determine the continuum of the spectrum or each spectral order. The differential Curve of Growth (CoG) abundance determination involves comparing the abundances of the star of interest to those of a standard or reference star, often the Sun; therefore, one must be able to determine the continuum in each spectral order in the same way for the star and the standard so as to minimize differences in the abundances that could arise as a result of the analysis. XSpect-EW has been designed to normalize the spectrum efficiently and accurately by using a two-step process which is explained in more detail in 3.

Step 1: a spectrum is split into smaller pieces (referred to as selection windows) where points above 90% of the flux values within a selection window are chosen as points in the continuum (90% value can be adjusted by the user if needed to accommodate different quality data).

Step 2: the chosen continuum points are used to normalize the spectrum by fitting them with a Gaussian Process (GP). Originally, in Vejar et al. (2021), a squared exponential (or gaussian) kernel was used to correlate the selected points on the continuum. While this was an effective kernel for fitting the continuum, it proved to be too smooth across absorption lines leading to a concave or convex fit over the absorption either increasing or decreasing some of the measured EW. To better fit the continuum, relying on the simple assumption that the noise in the spectrum is relatively Gaussian (not completely true due to instrument noise), the kernel was update to the Matern32 kernel. The Matern covariance between two points separated by distance d units is given by $C_\nu(d) = \sigma^2 \frac{2^{1-\nu}}{\Gamma(\nu)}(\sqrt{2\nu}\frac{d}{\rho})^\nu K_\nu(\sqrt{2\nu}\frac{d}{\rho})$ where Γ is the gamma function, K_ν is the modified Bessel function of the second kind, and ρ and ν are positive parameters of the covariance (Abramowitz, 1974). The Matern32 kernel is a ν half integer simplification where $\nu = p + 1/2$ which gives: $C_{3/2}(d) = \sigma^2(1 + \frac{\sqrt{3}d}{\rho})\exp(-\frac{\sqrt{3}d}{\rho})$. As ν reaches infinity, the Matern covariance converges to the squared exponential covariance. Intuitively, this means the Matern family of kernels are less smooth than the Gaussian Kernel, which is what we are looking for when fitting the continuum due to the noise in the data. After testing, the Matern32 kernel delivers more consistent EW measurements allowing for better precision. The flux is then divided by the curve output by the GP (grey curve in Fig. 4.1 top panel) which normalizes the order (Fig. 4.1 bottom panel).

The updated kernel came about from another normalization related update. Instead of using custom written GP code, the GP code has been switched over to the python package called george (Ambikasaran et al., 2015). The package comes standard with a variety of kernels and the GP is written in a object oriented manner, allowing for hyper parameters to be optimized. This in turn, made it possible to automate most of the

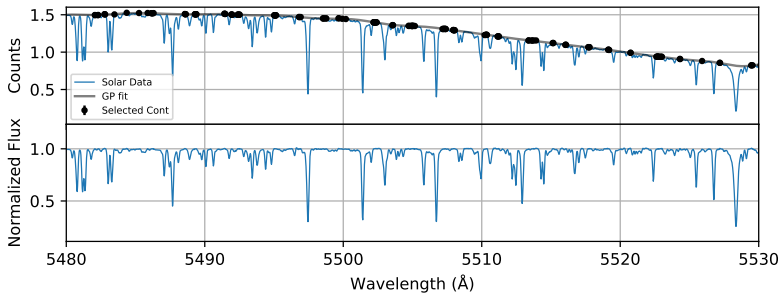

Figure 4.1: Sample section of an order within the observed solar spectrum before and after normalization. Black points are those selected as part of the continuum; black curve is the output of the Gaussian Process.

normalization process, with only two inputs from the user; the size of the spectrum slices used to select the continuum (dependant on the size of the absorption lines) and the depth of the points selected (points above this percentile within the spectrum slice are chosen as part of the continuum).

The user can now specify a wavelength range to isolate and re-normalize. While the overall normalization is generally robust, it can unpredictable given any spectrum data so this tool is meant to give the user more control in making any minor adjustments to eliminate any build up of inconsistencies in the EW measurement.

4.3.1.1 Wavelength Shift

Once normalization is complete, each order is wavelength shifted to the rest frame. XSpect-EW makes use of a simple χ^2 minimization approach to this problem. An input spectrum is shifted to match a solar spectrum or reference spectrum order by order. The solar or reference spectrum should be normalized before being used for this process. The shift is determined by evaluating χ^2 between each order for a range of wavelength shifts from -5 Å to +5 Å in steps of 0.1 Å then selecting the shift with the minimum χ^2 value. A user may also manually shift any order by a specified amount for further correction if needed.

4.3.1.2 Equivalent Width Measurements

Measuring the EW of an absorption line generally involves fitting a Gaussian or Voigt function to the line and then integrating that function to determine the area enclosed by the curve and continuum. XSpect-EW uses a four step process for this.

Step 1: the extent of the line being measured is determined. A piece of the spectrum around a selected line is trimmed from the rest of the spectrum (default set to 1.5 Å about the line center). The boundaries of the line being measured are determined by utilizing the slope of the flux values within the piece of the spectrum. Using one half of the standard deviation of the flux slope values, a range of values centered on the continuum is created. After testing various values, one half of the standard deviation gave us best results

relative to hand-measured EWs.

Step 2: with the boundaries defined, XSpect-EW assumes the continuum is correct and shifts the data outside the boundaries of the line (within the 1.5 Å line window) to match the continuum, effectively isolating the line to be measured.

Step 3: the isolated absorption line and associated continuum is fed into another GP (using the original squared exponential kernel) with a small variance of 1 and large inverse lengthscale of 100.

Step 4: the GP can produce different realizations of the data, and XSpect-EW uses this to perform a Gaussian fit to the line, repeating the process now 500 times and thus producing 500 different EW measurements. The mean and standard deviation are calculated using the 500 measurements of the line. Each absorption line can be plotted and remeasured if needed, with the ability to adjust the local continuum, center of the line, and boundaries of the line.

The default window width of 1.5 Å has been updated to be adjustable if necessary. At times an absorption line will appear very close to the edge of an order. When isolating a line to be measured, XSpect-EW will select a total wavelength range of 1.5 Å about the line which can fall outside of the spectrum values and cause an error. By changing this wavelength range to a smaller range, the user will be able to avoid this ”out of range” error. It should be kept in mind that the wavelength range used to isolate the line is also used to fit the line so EWs may be slightly affected.

The user can now save any and all measured line plots automatically. This option is off by default but if turned on will create a directory for all images and automatically populate the directory as new images are saved. This can be useful for sharing measured lines with colleagues or for use in publications and posters.

The output plot has been updated to show only information to the user and now includes green points where the data is within 1σ of the continuum. This is meant to make it easier to see how close the data actually is to the continuum past the wings of the Gaussian, which makes it easier for the user to determine if the data needs to be vertically shifted. A secondary panel plot has been added as well and can be seen in Fig. 4.2. The second panel plots only the data points for a better look at the actual data with no extra overlapping information.

4.3.2 New User Tools

4.3.2.1 Spectrum Combine

At times spectra are obtained in multiple observations producing multiple files and have not been combined. The user now has the ability to combine the flux of these files to achieve a higher signal to noise ratio. Ideally, the data would be structured in the same way (same number of orders and arrays having the same number of elements). Spectra are likely to have very similar wave-shift (if not identical), so an option has been included

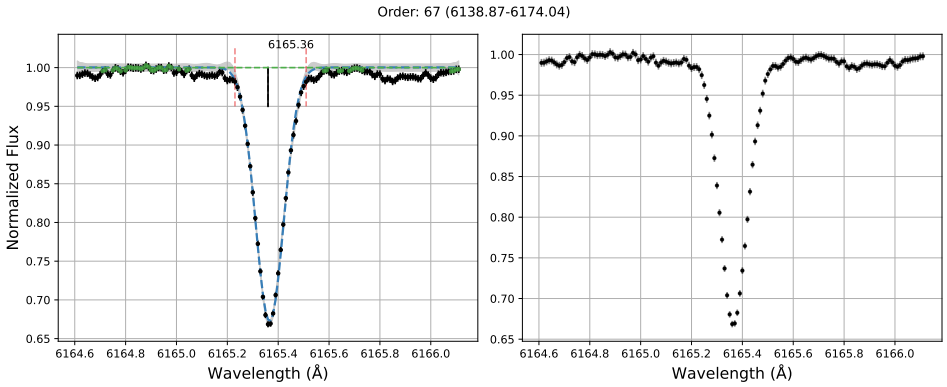

Figure 4.2: Updated line measurement view. Left Panel: Original output line measure plot with a few updates to the visual presentation. The dashed blue line is the averaged Gaussian fit to the line. Black points are the data while grey fill represents the estimated error of the data. Red vertical dashed lines show the boundaries of the data considered for the line fit (which can be adjusted by the user). Vertical dashed and solid black lines are the input and best fit wavelengths for the line. Green points show where the data is within 1σ of the continuum. Right Panel: Same plot as the left except only the data is shown for closer inspection of the shape and position of the data points.

that shifts the spectra about each other at an adjustable resolution to achieve the most accurate stacking per wavelength element.

4.3.2.2 Pickle Me This

It may be useful to save the spectrum object if some work has already been done to it to continue working with the object at a later time, or to share the object with colleagues. The user can now save the spectrum object and all of its stored information to a pickle file (a type of file that allows storing python objects that can be retrieved later). An alternative is to make sure to save the notebook, since it keeps all the steps performed as individual cells.

4.3.2.3 Auto S/N Estimation

The user can now estimate the signal to noise ratio for each order in the spectrum. This is presented as a grid of plots (the number of plots can be adjusted to account for different numbers of orders). For Keck files, with the appropriate header information, the S/N will be automatically calculated from the stored chip gain values in the header. If this information does not exist (values are not present in the header or not using a fits file to load data), the user can assign the gain values manually. Estimating the S/N per order is a good way to double check that the quality of the data is as expected.

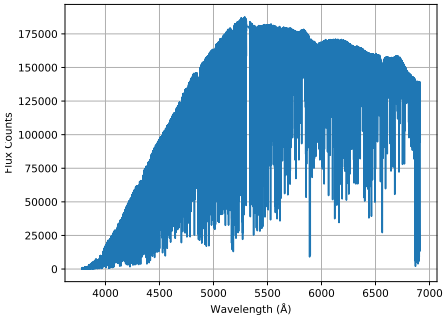

Figure 4.3: A publicly available Solar spectrum from the HARPS spectrograph used for testing. The data, being all one color, is completely held in just two arrays; a wavelength and a flux array.

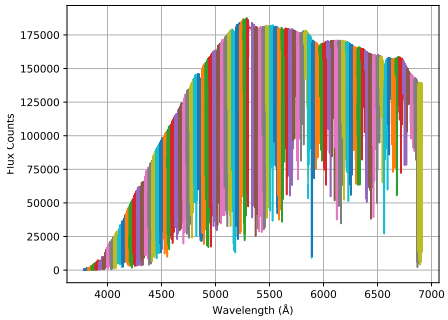

Figure 4.4: The same data set in 4.3 after it has been automatically split into artificial orders by XSpect-EW. Each separate color represents a different order (colors that appear multiple times are not apart of the same order).

4.3.2.4 Input Any Spectrum

The most important update to XSpect-EW is the ability to load any x and y array as spectra. Before, only Keck FITS files were accepted as input. This is because XSpect-EW was written using Keck FITS files as tests and precautions were taken to accept data before and after 2003 when an upgrade was made to the spectrograph, changing the structure of the FITS files. The update makes it possible for anyone to use XSpect-EW on any spectra, an important feature to help make XSpect-EW more universal.

XSpect-EW handles spectrum data order by order. Data can be loaded in one large array for the wavelength and another for the flux, in which case, XSpect-EW will do the work of splitting up the data into artificial orders of a size where the number of points is manageable per order, shown in Figs. 4.3, 4.4. If the data is already split into order then this step is skipped. After testing on a MackBook Pro 2017, with a 2.3 GHz Dual-Core Intel Core i5, the number of manageable points is about 3500 points/order. It should take about a minute to normalize all orders depending on the resolution of the spectrum, total number of orders, and computer performance. The number of points/order can also be changed if necessary, possibly in cases where the computer used is taking too long to normalize or will not finish. It is possible for the notebook kernel to die if a process takes too long. To avoid this, decrease the number of points/order, this will increase the total number of orders but will use less points as input to the GP which is the bottleneck.

4.3.2.5 Verification of Methodology

XSpect-EW was used to analyze all the stars in Vejar et al. (2021) where verification is covered in detail. This will be a summary for completeness. To verify the robustness of XSpect-EW, in Figure 4.5 we compare

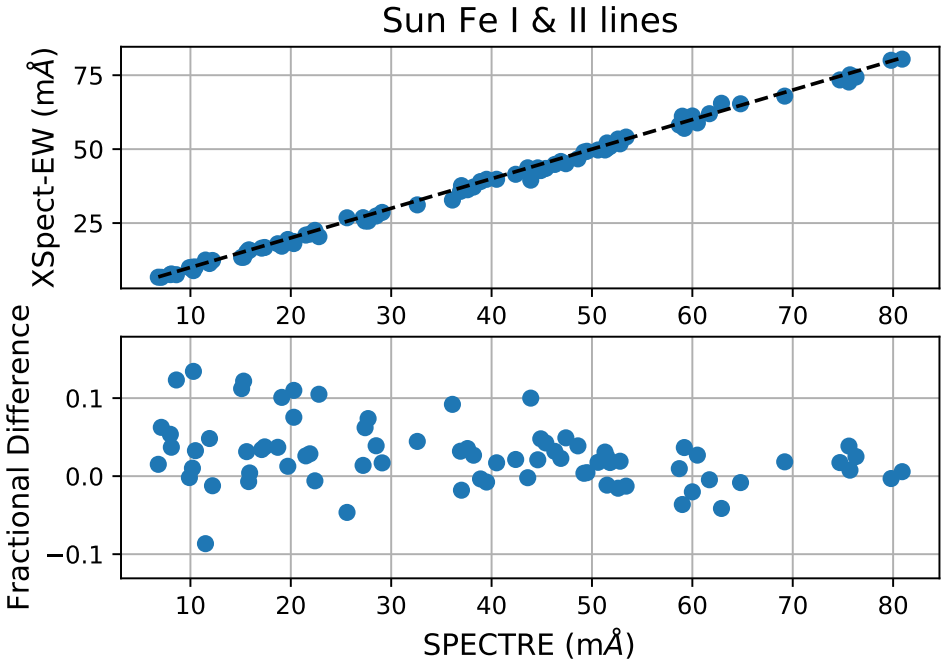

Figure 4.5: Top panel: XSpect-EW measured lines (with some user input) plotted against hand measured EWs in SPECTRE. Dashed line is the one-to-one line. Bottom panel: Fractional difference ([XSpect-EW − hand] / hand) between XSpect-EW and hand measured values.

EWs of Fe I and Fe II lines measured in our solar spectrum with XSpect-EW and by hand with SPECTRE, a spectral analysis package (Sneden et al., 2012). All differences are $< 15\%$, with 80% of Fe lines having differences smaller than 5%. In the remaining elemental lines (not shown here), $\sim$70% of lines have differences smaller than 5%. The scatter in the fractional difference of the line measurements is larger for the other elements, because those lines can generally be more difficult to measure due to the variety in the strength of the lines and proximity to other lines. In this example, 17% of Fe lines and 23% of other elemental lines required remeasuring, greatly reducing the amount of time needed to measure all lines and allowing the user to focus on problematic lines to produce abundances with high precision. The average of the Fe absolute abundances derived from the XSpect-EW and SPECTRE EWs, shown in Figure 4.6, agree within errors and agree with the input solar absolute abundance within MOOG of 7.50 dex. For all Fe I and II lines, we see a smaller scatter in the absolute abundances from the XSpect-EW measurements than in the SPECTRE measurements by 0.01 dex. From this we can see that XSpect-EW performs as well, if not slightly better, than a full set of hand-measured EWs from SPECTRE.

In Table 4.1, we show the literature stellar parameter values for each star in Vejar et al. (2021) along with our own derived values. Our derived stellar parameters ($T_{\rm eff}, \log G, [Fe/H]$) are also in good agreement with current literature values. The main discrepancy between our stellar parameters and literature values comes

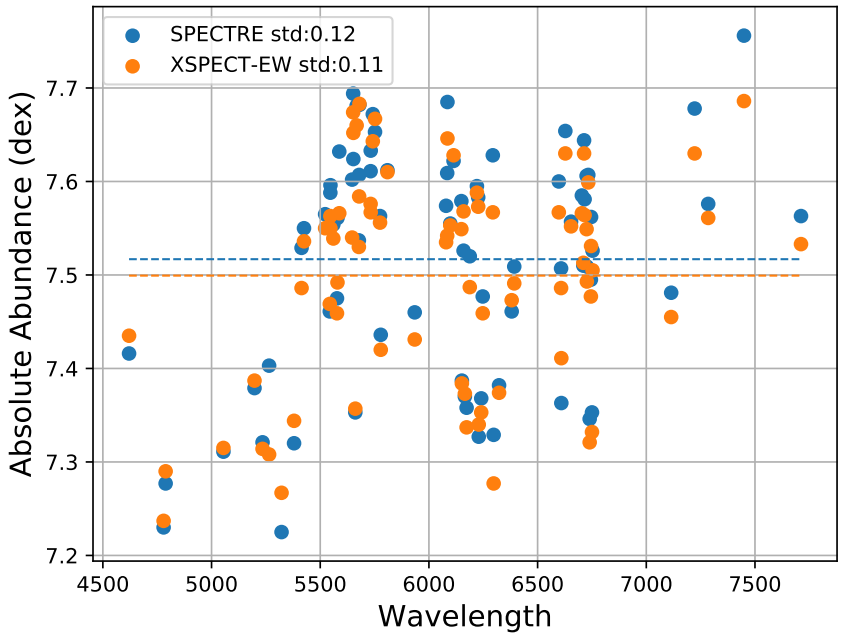

Figure 4.6: Output absolute abundances from Solar FeI and FeII lines shown in Figure 4.5 using MOOG. Blue points represent abundances from SPECTRE measurements while orange points represent abundances from XSpect-EW. The dashed lines (same colors used as for points) show the average abundances for each method.

Table 4.1: Comparison to Literature

Star ID alt ID	T_{eff} K	$\log G$ $\log(g \cdot cm \cdot sec^{-1})$	ξ km/s	[Fe/H] dex	Reference
Pr0201	6168 ± 35	4.34 ± 0.10	1.52 ± 0.06	0.23 ± 0.05	Vejar et al. (2021)
Prae kw 418	6174 ± 50	4.41 ± 0.10	—	0.19 ± 0.04	Quinn et al. (2012)
	6062 ± 110	4.44 ± 0.07	1.27 ± 0.18	0.24 ± 0.10	Pace et al. (2008)
Pr0133	6067 ± 60	4.18 ± 0.12	1.74 ± 0.11	0.19 ± 0.06	Vejar et al. (2021)
Prae kw 208	6005 ± 19	4.46 ± 0.21	1.05 ± 0.04	0.18 ± 0.03	Gebran et al. (2019)
	5997 ± 60	4.38 ± 0.20	1.40 ± 0.20	0.12 ± 0.10	Boesgaard et al. (2013)
	5993 ± 110	4.45 ± 0.07	1.52 ± 0.18	0.28 ± 0.10	Pace et al. (2008)
Pr0208	5869 ± 46	4.37 ± 0.13	1.53 ± 0.07	0.26 ± 0.07	Vejar et al. (2021)
N2632-8	5977 ± 75	4.55 ± 0.15	1.30 ± 0.20	0.25 ± 0.11	D'Orazi et al. (2020)
Prae kw 432	5841 ± 73	4.40 ± 0.20	1.25 ± 0.20	0.17 ± 0.10	Boesgaard et al. (2013)
Pr0081	5731 ± 42	4.44 ± 0.11	1.41 ± 0.06	0.18 ± 0.06	Vejar et al. (2021)
CPrae kw 30	5716 ± 45	4.57 ± 0.42	1.18 ± 0.04	0.12 ± 0.04	Gebran et al. (2019)
	5675 ± 111	4.44 ± 0.20	1.07 ± 0.20	0.12 ± 0.10	Boesgaard et al. (2013)
Pr0051 TYC 1395-668-1	6017 ± 27	4.40 ± 0.07	1.54 ± 0.05	0.16 ± 0.03	Vejar et al. (2021)
Pr0076	5748 ± 24	4.44 ± 0.07	1.35 ± 0.03	0.22 ± 0.05	Vejar et al. (2021)
Prae kw 23	5773 ± 53	4.56 ± 0.24	1.20 ± 0.04	0.20 ± 0.04	Gebran et al. (2019)
	5699 ± 79	4.43 ± 0.20	1.10 ± 0.20	0.12 ± 0.10	Boesgaard et al. (2013)

from the ξ parameter values which in general are larger than literature values, likely due to the higher ξ value adopted for the Sun in this work (1.38 km/s here, compared to lower values used in other studies)(Pace et al., 2008; Gebran et al., 2019; D'Orazi et al., 2020). A more detailed comparison of individual stars to the literature is presented in section 3.3.2.

4.4 Known Issues and Future Updates

XSpect-EW and its updates are already being used to analyze more stars in Open Clusters, however, it is far from being finished or free of bugs. Not all data used as input will work immediately, more options will be added slowly. At the moment, there may need to be some pre-processing of the data by the user to have it work correctly within XSpect-EW, but tutorials have been included to cover some common situations. Hot pixels or cosmic ray detection is currently not included, adding detection of this is planned but not a priority. Values that differ greatly from the continuum (above) will be correlated by the GP and cause issues in the continuum fit. These values should be handled by the user beforehand (XSpect-EW does have a function that can be used to replace any value in an array with an input value or the median or average of the input array, see documentation). Not a number (NaN) values should be removed or replaced as they will cause an issue with the GP during normalization. After normalization, the last element in each order may be left untouched by the normalization, this is a bug and planned to be fixed. Until then, the user can ignore these points (as they usually do not interfere with the measurements) or, only if completely necessary, the replace function

can be used to bring those points to the same level as the continuum. Take care when doing this as some points may be a part of an absorption line and adjusting these points can affect the EW measurement in the final Gaussian fit.

The GP regression is slow for a large amount of points, it is always better to decrease the number points/order and increase the number of orders for the GP to be able to finish. When measuring individual lines (either alone or in bulk), XSpect-EW will find the desired line and move on to the next line once it has made the measurement, this is intentional but will be updated to include multiple measurements of the same line if it appears in other parts of the spectrum. This can happen when orders overlap and a desired line is positioned in the overlapping wavelength region. The user can either take the first measurement, or work with the code to specifically measure the line only in a specific order, which is possible, however requires a deeper knowledge of the inner workings of the code. At the moment, plans are to either add the multiple measurement or include a tutorial on how to measure a line in a specific order, whichever takes less time to implement. The long term goal is to include the multiple possible measurements. The spectrum combine function currently only works correctly if the spectra are nearly identical and should be tested before accepting the output. If it does not seem to be working, the user may have to combine the spectra beforehand manually or using a different software. Plans are to correct any issues with this part of the code, although unexpected variations in input spectral data are likely to challenge how well this function will work. XSpect-EW is currently so simple it only uses one line profile to fit absorption lines, a Gaussian profile. It is planned to include other functions such as the Voigt function for larger absorption lines that the user can select for specific lines when necessary. Absorption lines may occasionally be split between orders (especially if the orders are artificially created by XSpect-EW) and will not be measured by the automated fitting function. An attempt is made to combine the order where this has happened with either the previous order or following order (depending where the line falls) and remeasure the line, however, this is currently an unreliable algorithm. The user is encouraged to inspect every measured line, use the tools available to help find problematic lines (see tutorials and documentation), not measure the line if possible, or re-load the data with a different number of orders (in hopes that the line will not end up between orders again).

4.5 Conclusion

XSpect-EW was created to make the process of manually measuring EWs from stellar spectra quick and simple to perform, this is the first set of updates that follow this idea. The code automatically normalizes each order, wavelength shifts the orders to the rest frame, and fits a Gaussian profile to each line of interest while allowing the user to edit and rerun any of these processes with specified parameters when necessary. This makes measuring hundreds of lines much faster as many lines can be measured automatically with little

user contribution and helps to remove some user error when manually performing these tasks.

The most important update is the ability to load spectra from any telescope, however, pre-processing steps may need to be taken before loading the data to ensure the code will work as intended. This update will open up the possible use of XSpect-EW to anyone interested in measuring EWs. The squared exponential kernel (Gaussian Kernel) for normalization has been changed to the Matern32 kernel for the fact that this kernel is less smooth than the squared exponential and fits the noisy data better. Continuum normalization is done autonomously, relying only on two hyper parameters for the user to choose (example parameters are given though other values should be tested if the quality or wavelength coverage of the spectra used differ from the sample included in the code). A number of tools have been added to improve the control and experience of the user: - Re-normalization of any input wavelength range - Line measurement window size adjustment - Improved line measurement plots - Spectrum Object can be pickled - S/N can be estimated given the gain of the instrument. A variety of bugs and known issues are addressed and either expect an update to fix them or a possible work-around is described. XSpect-EW has been made publicly available through Github at https://github.com/forgeousgeorge/XSpect.

4.6 Appendix

Tutorials on how to use XSpect-EW and its extra functions will be included in the Github as Jupyter Notebooks. Some helpful comments are also available within the code. This overview will outline the basic use and function of important parts of the code.

4.6.1 Loading the Data

Create the class object and store in a variable. This object initializes where all analysis data will go, including the spectral data itself. Data can be accessed using the dot notation with object: Spectrum_Data.wavelength or .flux will return appropriate loaded arrays. Other stored values can also be returned, go to the Github page for more detials.

Spectrum_Data(filename, KECK_file = True, spectx=False, specty=False, order_split = (False,3500))

- filename: path name of location of file if using a Keck fits file (leave other options alone)
- KECK_file: set to False if not using KECK file
- spectx: set to wavelength array data if not using KECK file; wavelength array must be an array of arrays (inside arrays are each order in spectrum); wavelength array can be a single array but must use order_split

- specty: set to flux array data if not using KECK file; flux array must be an array of arrays (inside arrays are each order in spectrum); flux array can be a single array but must use order_split
- order_split: set to (True,3500) if using single arrays for spectx and specty; 3500 refers to the number of points per order used when splitting input arrays into orders; more points will slow down GP during normalization; set to (False, 3500) if input arrays are already split up into orders

4.6.2 Normalizing the Data

This method takes the loaded data, normalizes it through the process explained in this chapter, and returns the normalized flux array to its own variable within the class object.

Spectrum_Data.normalize_all(window_width = 1.5, continuum_depth = 90)

- window_width: set size of window used to divide orders; should be much larger than typical size of absorption lines
- continuum_depth: set percentage of values within each window above which points will be selected as part of the continuum; high value for high signal-to-noise ratio; low value for low signal-to-noise ratio

4.6.3 Loading the Line List

This method takes a path to a line list text file as input, extracts information from the file, and populates the class object with this line information. File must be formatted to work with MOOG, examples are included in Github.

Spectrum_Data.load_lines(filename)

- filename: path name of line list text file

4.6.4 Measuring and Plotting All Lines

This method has five options detailed below. This is used to bulk measure all lines loaded to the class object.

Spectrum_Data.measure_all_ew(exclude_lines= [], plot_lines=[], ex_params = {}, window_size = 1.5, save_all = False)

- exclude_lines: set to an array of lines by wavelength that should not be measured; lines will be skipped
- plot_lines: set to an array of lines by wavelength that should be plotted for visual inspection; all lines initially should be inspected by user
- ex_params: set to dictionary where keys are line wavelength values and dictionary values are a list of four values associated with that wavelength; the four values define adjustments to be made to the Gaussian fit; [vertical shift, left line boundary, right line boundary, line center]

- window_size: set window size of data extracted around a line when measured; useful to make smaller if a line is close to the edge of an order
- save_all: set to True if you want to save all printed figures; this will create a folder for saved images

4.6.5 Measure and Plot Single Lines

This method is to be used to measure single lines, perhaps to revisit a line. It has some similar options to the previous method but also some unique options.

Spectrum_Data.measure_line_ew(line,ex_params=[0,0,0,0], save_line = False, save_plot = False, window_size = 1.5)

- line: line wavelength to measure
- ex_params: same as above; parameters to adjust fit; [vertical shift, left line boundary, right line boundary, line center]
- save_line: set to True will create a text file with X and Y arrays used to create plot
- save_plot: set to True will save the plot of the measured line
- window_size: same as above

4.6.6 Output Measurements

This method writes the measured EWs to a file in the format accepted by MOOG.

Spectrum_Data.make_ew_doc(name,doc_title='STARNAME, PROJECT, YEAR; ')

- name: name of the file; saved as .txt
- doc_title: title placed at top of file

CHAPTER 5

Future Work

Future prospects point to expanding the current work with detailed chemical abundances to further explore the stellar life cycle in specific environments. My work developing the semi-automatic equivalent width (EW) measurement code, XSpect - EW, has enabled the rapid, consistent, and accurate measurement of EWs, already doubling the number of our analyzed stars in the Praesepe Cluster (see Chapter 3). Our work with Praesepe has extended our aim to not only explore planet formation in open clusters but to test the chemical homogeneity among open clusters by improving current abundance measurements for nearby clusters. In the process of this analysis, we would create a gold standard of abundance measurements that can be used in future machine learning applications to abundance work.

Open clusters are important laboratories for understanding a broad range of astrophysical phenomena. They have been used to study Galactic chemical evolution Boesgaard et al. (2020); Anthony-Twarog et al. (2018), the structure and evolution of the Galactic disk Reddy et al. (2015); MacLean et al. (2015), stellar physics Davis et al. (2019); Schuler et al. (2009b), and light element abundances Boesgaard et al. (2016); François et al. (2013), to name a few. The basis of all these studies, and most studies concerning open clusters, is the assumption that open clusters are stellar conglomerates containing coeval stars that formed out of a well-mixed molecular cloud. This implies that the stars in a given open cluster are the same age, have the same primordial compositions, and are the same distance from the Sun. These properties allow for the systematic determination of their ages Maurya and Joshi (2020); Sandquist et al. (2016), detailed compositions Lum and Boesgaard (2019); Liu et al. (2016a), distances Monteiro and Dias (2019); González-Díaz et al. (2019), and kinematic properties Maurya and Joshi (2020); Geller et al. (2015).

There is significant support for the chemical homogeneity of open clusters in the literature, both from observations De Silva et al. (2006, 2007); Boesgaard et al. (2013) and simulations Feng and Krumholz (2014); Armillotta et al. (2018). However, studies both old and new have identified stars whose compositions deviate from their cluster means. One early study found two dwarfs in the Hyades with [Fe/H] a factor of four lower than the 10 other stars in their sample Cayrel et al. (1985). A study of 16 dwarfs in the Pleiades identified one star with [Fe/H] that is 0.1 dex higher than the cluster mean Wilden et al. (2002). Neither study definitively determined the cause of the anomalous abundances, but the Pleiades star was tagged as a candidate for having accreted hydrogen-depleted material from a disk and thus a potential planetary host Wilden et al. (2002). More recent analyses have also identified open cluster stars with compositions that deviate from their cluster means. One study of five Pleiades dwarfs found that two have anomalous compositions Spina

et al. (2018). The derived abundance patterns were shown to be consistent with expectations of planetary accretion. Abundance variations consistent with the effects of atomic diffusion have also been found in the solar-age open cluster M67 Souto et al. (2019); Liu et al. (2019). The abundances of numerous elements for red clump stars are higher than those on the main sequence (MS) turnoff, which are higher than those of subgiant stars, as predicted by atomic diffusion models Choi et al. (2016). Thus planet formation and atomic diffusion can be added to the list of physical processes—a list that includes rotational mixing Deliyannis et al. (2019), first dredge-up Böcek Topcu et al. (2020), and mass transfer Milliman et al. (2015)—that can change the compositions of stars in open clusters. None of them belie the inference that open clusters formed out of well-mixed molecular clouds; they do mean, though, that the composition of individual stars may be inhomogeneous when compared to other stars in the cluster.

Intrinsic inhomogeneities resulting from physical processes affecting the star forming cloud have also been reported. A study of 16 solar-type dwarfs in the Hyades cluster revealed an intrinsic abundance dispersion of 0.021 ± 0.003 dex in the 19 elements derived for each star Liu et al. (2016b). Three possible sources of the dispersion were considered: 1) inhomogeneous chemical evolution of the star-forming molecular cloud, 2) mixing of supernova ejecta within the cloud, and 3) dilution of the cloud with metal-poor or -rich gas. Only the third possibility was found to be a plausible explanation for the observed abundance spreads. A similar level of dispersion of the abundances of 20 elements has also been reported for 100 stars spread across the Hyades, Praesepe (Beehive), and Ruprecht 147 open clusters (Casamiquela et al., 2020). Indeed, the dispersion seen in the Hyades is in good agreement between the two studies, and both are consistent with derived limits on possible intrinsic abundance dispersions in open clusters (Bovy, 2016), suggesting that most stars in a given cluster formed before the cloud was polluted by core collapse supernovae, and implying the cloud was well but not perfectly mixed during the star formation episode. Studying open clusters with a higher level of precision and consistency across clusters will enable us to answer some of these and new mysteries.

References

Abazajian, K. N., Adelman-McCarthy, J. K., Agüeros, M. A., Allam, S. S., Prieto, C. A., An, D., Anderson, K. S. J., Anderson, S. F., Annis, J., Bahcall, N. A., Bailer-Jones, C. A. L., Barentine, J. C., Bassett, B. A., Becker, A. C., Beers, T. C., Bell, E. F., Belokurov, V., Berlind, A. A., Berman, E. F., Bernardi, M., Bickerton, S. J., Bizyaev, D., Blakeslee, J. P., Blanton, M. R., Bochanski, J. J., Boroski, W. N., Brewington, H. J., Brinchmann, J., Brinkmann, J., Brunner, R. J., Budavári, T., Carey, L. N., Carliles, S., Carr, M. A., Castander, F. J., Cinabro, D., Connolly, A. J., Csabai, I., Cunha, C. E., Czarapata, P. C., Davenport, J. R. A., de Haas, E., Dilday, B., Doi, M., Eisenstein, D. J., Evans, M. L., Evans, N. W., Fan, X., Friedman, S. D., Frieman, J. A., Fukugita, M., Gänsicke, B. T., Gates, E., Gillespie, B., Gilmore, G., Gonzalez, B., Gonzalez, C. F., Grebel, E. K., Gunn, J. E., Györy, Z., Hall, P. B., Harding, P., Harris, F. H., Harvanek, M., Hawley, S. L., Hayes, J. J. E., Heckman, T. M., Hendry, J. S., Hennessy, G. S., Hindsley, R. B., Hoblitt, J., Hogan, C. J., Hogg, D. W., Holtzman, J. A., Hyde, J. B., Ichikawa, S.-i., Ichikawa, T., Im, M., Ivezić, , Jester, S., Jiang, L., Johnson, J. A., Jorgensen, A. M., Jurić, M., Kent, S. M., Kessler, R., Kleinman, S. J., Knapp, G. R., Konishi, K., Kron, R. G., Krzesinski, J., Kuropatkin, N., Lampeitl, H., Lebedeva, S., Lee, M. G., Lee, Y. S., Leger, R. F., Lépine, S., Li, N., Lima, M., Lin, H., Long, D. C., Loomis, C. P., Loveday, J., Lupton, R. H., Magnier, E., Malanushenko, O., Malanushenko, V., Mandelbaum, R., Margon, B., Marriner, J. P., Martínez-Delgado, D., Matsubara, T., McGehee, P. M., McKay, T. A., Meiksin, A., Morrison, H. L., Mullally, F., Munn, J. A., Murphy, T., Nash, T., Nebot, A., Neilsen, E. H., Newberg, H. J., Newman, P. R., Nichol, R. C., Nicinski, T., Nieto-Santisteban, M., Nitta, A., Okamura, S., Oravetz, D. J., Ostriker, J. P., Owen, R., Padmanabhan, N., Pan, K., Park, C., Pauls, G., Peoples, J., Percival, W. J., Pier, J. R., Pope, A. C., Pourbaix, D., Price, P. A., Purger, N., Quinn, T., Raddick, M. J., Fiorentin, P. R., Richards, G. T., Richmond, M. W., Riess, A. G., Rix, H.-W., Rockosi, C. M., Sako, M., Schlegel, D. J., Schneider, D. P., Scholz, R.-D., Schreiber, M. R., Schwope, A. D., Seljak, U., Sesar, B., Sheldon, E., Shimasaku, K., Sibley, V. C., Simmons, A. E., Sivarani, T., Smith, J. A., Smith, M. C., Smolčić, V., Snedden, S. A., Stebbins, A., Steinmetz, M., Stoughton, C., Strauss, M. A., SubbaRao, M., Suto, Y., Szalay, A. S., Szapudi, I., Szkody, P., Tanaka, M., Tegmark, M., Teodoro, L. F. A., Thakar, A. R., Tremonti, C. A., Tucker, D. L., Uomoto, A., Vanden Berk, D. E., Vandenberg, J., Vidrih, S., Vogeley, M. S., Voges, W., Vogt, N. P., Wadadekar, Y., Watters, S., Weinberg, D. H., West, A. A., White, S. D. M., Wilhite, B. C., Wonders, A. C., Yanny, B., Yocum, D. R., York, D. G., Zehavi, I., Zibetti, S., and Zucker, D. B. (2009). THE SEVENTH DATA RELEASE OF THE SLOAN DIGITAL SKY SURVEY. *The Astrophysical Journal Supplement Series*, 182(2):543–558.

Abolfathi, B., Aguado, D. S., Aguilar, G., Prieto, C. A., Almeida, A., Ananna, T. T., Anders, F., Anderson, S. F., Andrews, B. H., Anguiano, B., Aragón-Salamanca, A., Argudo-Fernández, M., Armengaud, E., Ata, M., Aubourg, E., Avila-Reese, V., Badenes, C., Bailey, S., Balland, C., Barger, K. A., Barrera-Ballesteros, J., Bartosz, C., Bastien, F., Bates, D., Baumgarten, F., Bautista, J., Beaton, R., Beers, T. C., Belfiore, F., Bender, C. F., Bernardi, M., Bershady, M. A., Beutler, F., Bird, J. C., Bizyaev, D., Blanc, G. A., Blanton, M. R., Blomqvist, M., Bolton, A. S., Boquien, M., Borissova, J., Bovy, J., Bradna Diaz, C. A., Nielsen Brandt, W., Brinkmann, J., Brownstein, J. R., Bundy, K., Burgasser, A. J., Burtin, E., Busca, N. G., Cañas, C. I., Cano-Díaz, M., Cappellari, M., Carrera, R., Casey, A. R., Sodi, B. C., Chen, Y., Cherinka, B., Chiappini, C., Choi, P. D., Chojnowski, D., Chuang, C.-H., Chung, H., Clerc, N., Cohen, R. E., Comerford, J. M., Comparat, J., do Nascimento, J. C., da Costa, L., Cousinou, M.-C., Covey, K., Crane, J. D., Cruz-Gonzalez, I., Cunha, K., Ilha, G. d. S., Damke, G. J., Darling, J., Davidson, J. W., Dawson, K., de Icaza Lizaola, M. A. C., Macorra, A. d. l., de la Torre, S., De Lee, N., Sainte Agathe, V. d., Deconto Machado, A., Dell'Agli, F., Delubac, T., Diamond-Stanic, A. M., Donor, J., Downes, J. J., Drory, N., Mas des Bourboux, H. d., Duckworth, C. J., Dwelly, T., Dyer, J., Ebelke, G., Eigenbrot, A. D., Eisenstein, D. J., Elsworth, Y. P., Emsellem, E., Eracleous, M., Erfanianfar, G., Escoffier, S., Fan, X., Alvar, E. F., Fernandez-Trincado, J. G., Cirolini, R. F., Feuillet, D., Finoguenov, A., Fleming, S. W., Font-Ribera, A., Freischlad, G., Frinchaboy, P., Fu, H., Chew, Y. G. M., Galbany, L., García Pérez, A. E., Garcia-Dias, R., García-Hernández, D. A., Garma Oehmichen, L. A., Gaulme, P., Gelfand, J., Gil-Marín, H., Gillespie, B. A., Goddard, D., González Hernández, J. I., Gonzalez-Perez, V., Grabowski, K., Green, P. J., Grier, C. J., Gueguen, A., Guo, H., Guy, J., Hagen, A., Hall, P., Harding, P., Hasselquist, S., Hawley,

S., Hayes, C. R., Hearty, F., Hekker, S., Hernandez, J., Hernandez Toledo, H., Hogg, D. W., Holley-Bockelmann, K., Holtzman, J. A., Hou, J., Hsieh, B.-C., Hunt, J. A. S., Hutchinson, T. A., Hwang, H. S., Jimenez Angel, C. E., Johnson, J. A., Jones, A., Jönsson, H., Jullo, E., Sakil Khan, F., Kinemuchi, K., Kirkby, D., Kirkpatrick IV, C. C., Kitaura, F.-S., Knapp, G. R., Kneib, J.-P., Kollmeier, J. A., Lacerna, I., Lane, R. R., Lang, D., Law, D. R., Le Goff, J.-M., Lee, Y.-B., Li, H., Li, C., Lian, J., Liang, Y., Lima, M., Lin, L., Long, D., Lucatello, S., Lundgren, B., Mackereth, J. T., MacLeod, C. L., Mahadevan, S., Geimba Maia, M. A., Majewski, S., Manchado, A., Maraston, C., Mariappan, V., Marques-Chaves, R., Masseron, T., Masters, K. L., McDermid, R. M., McGreer, I. D., Melendez, M., Meneses-Goytia, S., Merloni, A., Merrifield, M. R., Meszaros, S., Meza, A., Minchev, I., Minniti, D., Mueller, E.-M., Muller-Sanchez, F., Muna, D., Muñoz, R. R., Myers, A. D., Nair, P., Nandra, K., Ness, M., Newman, J. A., Nichol, R. C., Nidever, D. L., Nitschelm, C., Noterdaeme, P., O'Connell, J., Oelkers, R. J., Oravetz, A., Oravetz, D., Ortíz, E. A., Osorio, Y., Pace, Z., Padilla, N., Palanque-Delabrouille, N., Palicio, P. A., Pan, H.-A., Pan, K., Parikh, T., Pâris, I., Park, C., Peirani, S., Pellejero-Ibanez, M., Penny, S., Percival, W. J., Perez-Fournon, I., Petitjean, P., Pieri, M. M., Pinsonneault, M., Pisani, A., Prada, F., Prakash, A., de Andrade Queiroz, A. B., Raddick, M. J., Raichoor, A., Rembold, S. B., Richstein, H., Riffel, R. A., Riffel, R., Rix, H.-W., Robin, A. C., Torres, S. R., Román-Zúñiga, C., Ross, A. J., Rossi, G., Ruan, J., Ruggeri, R., Ruiz, J., Salvato, M., Sánchez, A. G., Sánchez, S. F., Almeida, J. S., Sánchez-Gallego, J. R., Rojas, F. A. S., Santiago, B. X., Schiavon, R. P., Schimoia, J. S., Schlafly, E., Schlegel, D., Schneider, D. P., Schuster, W. J., Schwope, A., Seo, H.-J., Serenelli, A., Shen, S., Shen, Y., Shetrone, M., Shull, M., Aguirre, V. S., Simon, J. D., Skrutskie, M., Slosar, A., Smethurst, R., Smith, V., Sobeck, J., Somers, G., Souter, B. J., Souto, D., Spindler, A., Stark, D. V., Stassun, K., Steinmetz, M., Stello, D., Storchi-Bergmann, T., Streblyanska, A., Stringfellow, G. S., Suárez, G., Sun, J., Szigeti, L., Taghizadeh-Popp, M., Talbot, M. S., Tang, B., Tao, C., Tayar, J., Tembe, M., Teske, J., Thakar, A. R., Thomas, D., Tissera, P., Tojeiro, R., Tremonti, C., Troup, N. W., Urry, M., Valenzuela, O., Bosch, R. v. d., Vargas-González, J., Vargas-Magaña, M., Vazquez, J. A., Villanova, S., Vogt, N., Wake, D., Wang, Y., Weaver, B. A., Weijmans, A.-M., Weinberg, D. H., Westfall, K. B., Whelan, D. G., Wilcots, E., Wild, V., Williams, R. A., Wilson, J., Wood-Vasey, W. M., Wylezalek, D., Xiao, T., Yan, R., Yang, M., Ybarra, J. E., Yèche, C., Zakamska, N., Zamora, O., Zarrouk, P., Zasowski, G., Zhang, K., Zhao, C., Zhao, G.-B., Zheng, Z., Zheng, Z., Zhou, Z.-M., Zhu, G., Zinn, J. C., and Zou, H. (2018). The Fourteenth Data Release of the Sloan Digital Sky Survey: First Spectroscopic Data from the Extended Baryon Oscillation Spectroscopic Survey and from the Second Phase of the Apache Point Observatory Galactic Evolution Experiment. *The Astrophysical Journal Supplement Series*, 235(2):42.

Abramowitz, M. (1974). *Handbook of Mathematical Functions, With Formulas, Graphs, and Mathematical Tables,*. Dover Publications, Inc., USA.

Adams, J. D., Stauffer, J. R., Skrutskie, M. F., Monet, D. G., Portegies Zwart, S. F., Janes, K. A., and Beichman, C. A. (2002). Structure of the Praesepe Star Cluster. , 124(3):1570–1584.

Allende Prieto, C., Lambert, D. L., and Asplund, M. (2001). The [ITAL]Forbidden[/ITAL] Abundance of Oxygen in the Sun. *The Astrophysical Journal*, 556(1):L63–L66.

Allende Prieto, C., Lambert, D. L., and Asplund, M. (2002). A Reappraisal of the Solar Photospheric C/O Ratio. *Astrophys. J.*, 573(2):L137–L140.

Aller, L. H. and Czyzak, S. J. (1983). Chemical compositions of planetary nebulae. *The Astrophysical Journal Supplement Series*, 51:211.

Ambikasaran, S., Foreman-Mackey, D., Greengard, L., Hogg, D. W., and O'Neil, M. (2015). Fast Direct Methods for Gaussian Processes. *IEEE Transactions on Pattern Analysis and Machine Intelligence*, 38:252.

An, D., Terndrup, D. M., Pinsonneault, M. H., Paulson, D. B., Hanson, R. B., and Stauffer, J. R. (2007). The Distances to Open Clusters from Main-Sequence Fitting. III. Improved Accuracy with Empirically Calibrated Isochrones. , 655(1):233–260.

Anderson, K. R., Adams, F. C., and Calvet, N. (2013). Viscous Evolution and Photoevaporation of Circumstellar Disks Due to External Far Ultraviolet Radiation Fields. , 774(1):9.

Anthony-Twarog, B. J., Lee-Brown, D. B., Deliyannis, C. P., and Twarog, B. A. (2018). WIYN Open Cluster Study. LXXVI. Li Evolution Among Stars of Low/Intermediate Mass: The Metal-deficient Open Cluster NGC 2506. , 155(3):138.

Armillotta, L., Krumholz, M. R., and Fujimoto, Y. (2018). Mixing of metals during star cluster formation: statistics and implications for chemical tagging. , 481(4):5000–5013.

Asplund, M., Grevesse, N., Sauval, A. J., and Scott, P. (2009). The Chemical Composition of the Sun. , 47(1):481–522.

Astropy Collaboration, Robitaille, T. P., Tollerud, E. J., Greenfield, P., Droettboom, M., Bray, E., Aldcroft, T., Davis, M., Ginsburg, A., Price-Whelan, A. M., Kerzendorf, W. E., Conley, A., Crighton, N., Barbary, K., Muna, D., Ferguson, H., Grollier, F., Parikh, M. M., Nair, P. H., Günther, H. M., Deil, C., Woillez, J., Conseil, S., Kramer, R., Turner, J. E. H., Singer, L., Fox, R., Weaver, B. A., Zabalza, V., Edwards, Z. I., Azalee Bostroem, K., Burke, D. J., Casey, A. R., Crawford, S. M., Dencheva, N., Ely, J., Jenness, T., Labrie, K., Lim, P. L., Pierfederici, F., Pontzen, A., Ptak, A., Refsdal, B., Servillat, M., and Streicher, O. (2013). Astropy: A community Python package for astronomy. *Astronomy & Astrophysics*, 558:A33.

Bachelet, E., Shin, I. G., Han, C., Fouqué, P., Gould, A., Menzies, J. W., Beaulieu, J. P., Bennett, D. P., Bond, I. A., Dong, S., Heyrovský, D., Marquette, J. B., Marshall, J., Skowron, J., Street, R. A., Sumi, T., Udalski, A., Abe, L., Agabi, K., Albrow, M. D., Allen, W., Bertin, E., Bos, M., Bramich, D. M., Chavez, J., Christie, G. W., Cole, A. A., Crouzet, N., Dieters, S., Dominik, M., Drummond, J., Greenhill, J., Guillot, T., Henderson, C. B., Hessman, F. V., Horne, K., Hundertmark, M., Johnson, J. A., Jørgensen, U. G., Kandori, R., Liebig, C., Mékarnia, D., McCormick, J., Moorhouse, D., Nagayama, T., Nataf, D., Natusch, T., Nishiyama, S., Rivet, J. P., Sahu, K. C., Shvartzvald, Y., Thornley, G., Tomczak, A. R., Tsapras, Y., Yee, J. C., Batista, V., Bennett, C. S., Brillant, S., Caldwell, J. A. R., Cassan, A., Corrales, E., Coutures, C., Dominis Prester, D., Donatowicz, J., Kubas, D., Martin, R., Williams, A., Zub, M., PLANET Collaboration, de Almeida, L. A., DePoy, D. L., Gaudi, B. S., Hung, L. W., Jablonski, F., Kaspi, S., Klein, N., Lee, C. U., Lee, Y., Koo, J. R., Maoz, D., Muñoz, J. A., Pogge, R. W., Polishook, D., Shporer, A., μFUN Collaboration, Abe, F., Botzler, C. S., Chote, P., Freeman, M., Fukui, A., Furusawa, K., Harris, P., Itow, Y., Kobara, S., Ling, C. H., Masuda, K., Matsubara, Y., Miyake, N., Ohmori, K., Ohnishi, K., Rattenbury, N. J., Saito, T., Sullivan, D. J., Suzuki, D., Sweatman, W. L., Tristram, P. J., Wada, K., Yock, P. C. M., MOA Collaboration, Szymański, M. K., Soszyński, I., Kubiak, M., Poleski, R., Ulaczyk, K., Pietrzyński, G., Wyrzykowski, Ł., OGLE Collaboration, Kains, N., Snodgrass, C., Steele, I. A., RoboNet Collaboration, Alsubai, K. A., Bozza, V., Browne, P., Burgdorf, M. J., Calchi Novati, S., Dodds, P., Dreizler, S., Finet, F., Gerner, T., Hardis, S., Harpsøe, K., Hinse, T. C., Kerins, E., Mancini, L., Mathiasen, M., Penny, M. T., Proft, S., Rahvar, S., Ricci, D., Scarpetta, G., Schäfer, S., Schönebeck, F., Southworth, J., Surdej, J., Wambsganss, J., and MiNDSTEp Consortium (2012). MOA 2010-BLG-477Lb: Constraining the Mass of a Microlensing Planet from Microlensing Parallax, Orbital Motion, and Detection of Blended Light. , 754(1):73.

Ballard, S., Fabrycky, D., Fressin, F., Charbonneau, D., Desert, J.-M., Torres, G., Marcy, G., Burke, C. J., Isaacson, H., Henze, C., Steffen, J. H., Ciardi, D. R., Howell, S. B., Cochran, W. D., Endl, M., Bryson, S. T., Rowe, J. F., Holman, M. J., Lissauer, J. J., Jenkins, J. M., Still, M., Ford, E. B., Christiansen, J. L., Middour, C. K., Haas, M. R., Li, J., Hall, J. R., McCauliff, S., Batalha, N. M., Koch, D. G., and Borucki, W. J. (2011). The Kepler-19 System: A Transiting 2.2 R $_\oplus$ Planet and a Second Planet Detected via Transit Timing Variations. , 743(2):200.

Bennett, D. P., Anderson, J., Bond, I. A., Udalski, A., and Gould, A. (2006). Identification of the OGLE-2003-BLG-235/MOA-2003-BLG-53 Planetary Host Star. , 647(2):L171–L174.

Biazzo, K., Gratton, R., Desidera, S., Lucatello, S., Sozzetti, A., Bonomo, A. S., Damasso, M., Gandolfi, D., Affer, L., Boccato, C., Borsa, F., Claudi, R., Cosentino, R., Covino, E., Knapic, C., Lanza, A. F., Maldonado, J., Marzari, F., Micela, G., Molaro, P., Pagano, I., Pedani, M., Pillitteri, I., Piotto, G., Poretti, E., Rainer, M., Santos, N. C., Scandariato, G., and Zanmar Sanchez, R. (2015). The GAPS programme with HARPS-N at TNG. X. Differential abundances in the XO-2 planet-hosting binary. , 583:A135.

Blackman, E. G. (2004). Dynamo-Driven Outflows in Pre-Planetary Nebulae. In Meixner, M., Kastner, J. H., Balick, B., and Soker, N., editors, *Asymmetrical Planetary Nebulae III: Winds, Structure and the Thunderbird*, volume 313, page 401.

Blanco-Cuaresma, S., Soubiran, C., Heiter, U., and Jofré, P. (2014). Determining stellar atmospheric parameters and chemical abundances of FGK stars with iSpec. , 569:A111.

Bloecker, T. (1995). Stellar evolution of low- and intermediate-mass stars. II. Post-AGB evolution. *Astronomy and Astrophysics*, 299:755.

Böcek Topcu, G., Afşar, M., Sneden, C., Pilachowski, C. A., Denissenkov, P. A., Vand enBerg, D. A., Wright, D., Mace, G. N., Jaffe, D. T., Strickland, E., Kim, H., and Sokal, K. R. (2020). Chemical abundances of open clusters from high-resolution infrared spectra - II. NGC 752. , 491(1):544–559.

Boesgaard, A. M., Lum, M. G., and Deliyannis, C. P. (2020). Correlated Depletion and Dilution of Lithium and Beryllium Revealed by Subgiants in M67. , 888(1):28.

Boesgaard, A. M., Lum, M. G., Deliyannis, C. P., King, J. R., Pinsonneault, M. H., and Somers, G. (2016). Boron Abundances Across the "Li-Be Dip" in the Hyades Cluster. , 830(1):49.

Boesgaard, A. M., Roper, B. W., and Lum, M. G. (2013). The Chemical Composition of Praesepe (M44). , 775(1):58.

Bohn, A. J., Kenworthy, M. A., Ginski, C., Manara, C. F., Pecaut, M. J., de Boer, J., Keller, C. U., Mamajek, E. E., Meshkat, T., Reggiani, M., Todorov, K. O., and Snik, F. (2020). The Young Suns Exoplanet Survey: Detection of a wide-orbit planetary-mass companion to a solar-type Sco-Cen member. , 492(1):431–443.

Bond, I. A., Udalski, A., Jaroszyński, M., Rattenbury, N. J., Paczyński, B., Soszyński, I., Wyrzykowski, L., Szymański, M. K., Kubiak, M., Szewczyk, O., Żebruń, K., Pietrzyński, G., Abe, F., Bennett, D. P., Eguchi, S., Furuta, Y., Hearnshaw, J. B., Kamiya, K., Kilmartin, P. M., Kurata, Y., Masuda, K., Matsubara, Y., Muraki, Y., Noda, S., Okajima, K., Sako, T., Sekiguchi, T., Sullivan, D. J., Sumi, T., Tristram, P. J., Yanagisawa, T., Yock, P. C. M., and OGLE Collaboration (2004). OGLE 2003-BLG-235/MOA 2003-BLG-53: A Planetary Microlensing Event. , 606(2):L155–L158.

Bovy, J. (2016). The Chemical Homogeneity of Open Clusters. , 817(1):49.

Cai, M. X., Kouwenhoven, M. B. N., Portegies Zwart, S. F., and Spurzem, R. (2017). Stability of multiplanetary systems in star clusters. , 470(4):4337–4353.

Cai, M. X., Portegies Zwart, S., Kouwenhoven, M. B. N., and Spurzem, R. (2019). On the survivability of planets in young massive clusters and its implication of planet orbital architectures in globular clusters. , 489(3):4311–4321.

Cantat-Gaudin, T., Jordi, C., Vallenari, A., Bragaglia, A., Balaguer-Núñez, L., Soubiran, C., Bossini, D., Moitinho, A., Castro-Ginard, A., Krone-Martins, A., Casamiquela, L., Sordo, R., and Carrera, R. (2018). A Gaia DR2 view of the open cluster population in the Milky Way. , 618:A93.

Cardelli, J. A., Clayton, G. C., and Mathis, J. S. (1989). The relationship between infrared, optical, and ultraviolet extinction. *The Astrophysical Journal*, 345:245.

Carrera, R. and Pancino, E. (2011). Chemical abundance analysis of the open clusters Berkeley 32, NGC 752, Hyades, and Praesepe. , 535:A30.

Casamiquela, L., Tarricq, Y., Soubiran, C., Blanco-Cuaresma, S., Jofré, P., Heiter, U., and Tucci Maia, M. (2020). Differential abundances of open clusters and their tidal tails: Chemical tagging and chemical homogeneity. , 635:A8.

Cavichia, O., Costa, R. D., Maciel, W. J., and Mollandá, M. (2017). The population of planetary nebulae near the galactic centre: Chemical abundances. *Monthly Notices of the Royal Astronomical Society*, 468(1):272–290.

Cayrel, R., Cayrel de Strobel, G., and Campbell, B. (1985). Steps towards the abundance scale. I. The abundance of heavy elements in the Hyades cluster. , 146:249–259.

Chabrier, G. (2003). Galactic Stellar and Substellar Initial Mass Function. , 115(809):763–795.

Charpinet, S., Fontaine, G., Brassard, P., Green, E. M., Van Grootel, V., Randall, S. K., Silvotti, R., Baran, A. S., Østensen, R. H., Kawaler, S. D., and Telting, J. H. (2011). A compact system of small planets around a former red-giant star. , 480(7378):496–499.

Chauvin, G., Lagrange, A. M., Dumas, C., Zuckerman, B., Mouillet, D., Song, I., Beuzit, J. L., and Lowrance, P. (2004). A giant planet candidate near a young brown dwarf. Direct VLT/NACO observations using IR wavefront sensing. , 425:L29–L32.

Choi, J., Dotter, A., Conroy, C., Cantiello, M., Paxton, B., and Johnson, B. D. (2016). Mesa Isochrones and Stellar Tracks (MIST). I. Solar-scaled Models. , 823(2):102.

Ciardullo, R. (2003). Distances from Planetary Nebulae. *Stellar Candles for the Extragalactic Distance Scale*, 635:243–263.

Coccato, L. and Coccato (2016). Planetary nebulae as kinematic tracers of galaxy halos. *Proceedings of the International Astronomical Union*, 11(A29B):20–25.

Corgan, A., Smith, N., Andrews, J., Filippenko, A. V., and Van Dyk, S. D. (2022). Massive stars dying alone: the remote environment of supernova 2010jp and its associated late-time source. , 510(1):1–10.

Corradi, R. L. M., Rodríguez–Flores, E. R., Mampaso, A., Greimel, R., Viironen, K., Drew, J. E., Lennon, D. J., Mikolajewska, J., Sabin, L., and Sokoloski, J. L. (2008). IPHAS and the symbiotic stars. *Astronomy & Astrophysics*, 480(2):409–419.

Corradi, R. L. M., Valentini, M., Munari, U., Drew, J. E., Rodríguez-Flores, E. R., Viironen, K., Greimel, R., Santander-García, M., Sabin, L., Mampaso, A., Parker, Q., De Pew, K., Sale, S. E., Unruh, Y. C., Vink, J. S., Rodríguez-Gil, P., Barlow, M. J., Lennon, D. J., Groot, P. J., Giammanco, C., Zijlstra, A. A., and Walton, N. A. (2010). IPHAS and the symbiotic stars. *Astronomy and Astrophysics*, 509:A41.

Dalcanton, J. J., Fouesneau, M., Hogg, D. W., Lang, D., Leroy, A. K., Gordon, K. D., Sandstrom, K., Weisz, D. R., Williams, B. F., Bell, E. F., Dong, H., Gilbert, K. M., Gouliermis, D. A., Guhathakurta, P., Lauer, T. R., Schruba, A., Seth, A. C., and Skillman, E. D. (2015). The panchromatic hubble andromeda treasury. VIII. A wide-area, high-resolution map of dust extinction in M31. *Astrophysical Journal*, 814(1):3.

Davis, B. D., Bond, H. E., Ciardullo, R., and Jacoby, G. H. (2019). Hubble Space Telescope Spectroscopy of a Planetary Nebula in an M31 Open Cluster: Hot-bottom Burning at 3.4 M . , 884(2):115.

De Marco, O. (2005). Common Envelope Evolution through Planetary Nebula Eyes. In Szczerba, R., Stasińska, G., and Gorny, S. K., editors, *AIP Conference Proceedings*, volume 804, pages 169–172. AIP.

De Marco, O. (2009). The Origin and Shaping of Planetary Nebulae: Putting the Binary Hypothesis to the Test. *Publications of the Astronomical Society of the Pacific*, 121(878):316–342.

De Silva, G. M., Freeman, K. C., Asplund, M., Bland-Hawthorn, J., Bessell, M. S., and Collet, R. (2007). Chemical Homogeneity in Collinder 261 and Implications for Chemical Tagging. , 133(3):1161–1175.

De Silva, G. M., Sneden, C., Paulson, D. B., Asplund, M., Bland-Hawthorn, J., Bessell, M. S., and Freeman, K. C. (2006). Chemical Homogeneity in the Hyades. , 131(1):455–460.

Deliyannis, C. P., Anthony-Twarog, B. J., Lee-Brown, D. B., and Twarog, B. A. (2019). Li Evolution and the Open Cluster NGC 6819: A Correlation between Li Depletion and Spindown in Dwarfs More Massive Than the F-Dwarf Li-Dip. , 158(4):163.

Delorme, P., Cameron, A. C., Hebb, L., Rostron, J., Lister, T. A., Norton, A. J., Pollacco, D., and West, R. G. (2011). Stellar Rotation in the Hyades and Praesepe: Gyrochronology and Braking Timescale. In Johns-Krull, C., Browning, M. K., and West, A. A., editors, *16th Cambridge Workshop on Cool Stars, Stellar Systems, and the Sun*, volume 448 of *Astronomical Society of the Pacific Conference Series*, page 841.

D'Orazi, V., Oliva, E., Bragaglia, A., Frasca, A., Sanna, N., Biazzo, K., Casali, G., Desidera, S., Lucatello, S., Magrini, L., and Origlia, L. (2020). Stellar population astrophysics (SPA) with the TNG. Revisiting the metallicity of Praesepe (M 44). , 633:A38.

Drew, J. E., Gonzalez-solares, E., Greimel, R., Irwin, M. J., Küpcü Yoldas, A., Lewis, J., Barentsen, G., Eislöffel, J., Farnhill, H. J., Martin, W. E., Walsh, J. R., Walton, N. A., Mohr-Smith, M., Raddi, R., Sale, S. E., Wright, N. J., Groot, P., Barlow, M. J., Corradi, R. L., Drake, J. J., Fabregat, J., Frew, D. J., Gänsicke, B. T., Knigge, C., Mampaso, A., Morris, R. A., Naylor, T., Parker, Q. A., Phillipps, S., Ruhland, C., Steeghs, D., Unruh, Y. C., Vink, J. S., Wesson, R., and Zijlstra, A. A. (2014). The VST photometric hα survey of the Southern Galactic Plane and Bulge (VPHAS+). *Monthly Notices of the Royal Astronomical Society*, 440(3):2036–2058.

Drew, J. E., Greimel, R., Irwin, M. J., Aungwerojwit, A., Barlow, M. J., Corradi, R. L. M., Drake, J. J., Gansicke, B. T., Groot, P., Hales, A., Hopewell, E. C., Irwin, J., Knigge, C., Leisy, P., Lennon, D. J., Mampaso, A., Masheder, M. R. W., Matsuura, M., Morales-Rueda, L., Morris, R. A. H., Parker, Q. A., Phillipps, S., Rodriguez-Gil, P., Roelofs, G., Skillen, I., Sokoloski, J. L., Steeghs, D., Unruh, Y. C., Viironen, K., Vink, J. S., Walton, N. A., Witham, A., Wright, N., Zijlstra, A. A., and Zurita, A. (2005). The INT Photometric H Survey of the Northern Galactic Plane (IPHAS). *Monthly Notices of the Royal Astronomical Society*, 362(3):753–776.

Fabian, A. C. and Hansen, C. J. (1979). Unravelling the 'Helix' nebula. *Monthly Notices of the Royal Astronomical Society*, 187(2):283–286.

Feng, Y. and Krumholz, M. R. (2014). Early turbulent mixing as the origin of chemical homogeneity in open star clusters. , 513(7519):523–525.

Ferland, G. J., Porter, R. L., van Hoof, P. A. M., Williams, R. J. R., Abel, N. P., Lykins, M. L., Shaw, G., Henney, W. J., and Stancil, P. C. (2013). The 2013 Release of Cloudy. *Revista Mexicana de Astronomia y Astrofisica*, 49(1):137–163.

Fragkou, V., Parker, Q. A., Bojicic, I. S., and Aksaker, N. (2018). New Galactic Planetary Nebulae selected by radio and multi-wavelength characteristics. *Monthly Notices of the Royal Astronomical Society*, 480(3):2916–2928.

François, P., Pasquini, L., Biazzo, K., Bonifacio, P., and Palsa, R. (2013). Lithium abundance in the metal-poor open cluster NGC 2243. , 552:A136.

Frew, D. J. (2008). *Planetary Nebulae in the Solar Neighbourhood: Statistics, Distance Scale and Luminosity Function*. PhD thesis, Department of Physics, Macquarie University, NSW 2109, Australia.

Frew, D. J., Bojičić, I. S., Parker, Q. A., Pierce, M. J., Gunawardhana, M. L., and Reid, W. A. (2014). Flux calibration of the AAO/UKST superCOSMOS Hα survey. *Monthly Notices of the Royal Astronomical Society*, 440(2):1080–1094.

Frew, D. J. and Parker, Q. A. (2010). Planetary Nebulae: Observational Properties, Mimics, and Diagnostics. *Publications of the Astronomical Society of the Australia*, 27(2):129–148.

Frew, D. J., Parker, Q. A., and Bojičić, I. S. (2016). The Hα surface brightness-radius relation: a robust statistical distance indicator for planetary nebulae. , 455(2):1459–1488.

Fujii, M. S. and Hori, Y. (2019). Survival rates of planets in open clusters: the Pleiades, Hyades, and Praesepe clusters. , 624:A110.

Gaia Collaboration, Brown, A. G. A., Vallenari, A., Prusti, T., de Bruijne, J. H. J., Babusiaux, C., Bailer-Jones, C. A. L., Biermann, M., Evans, D. W., Eyer, L., Jansen, F., Jordi, C., Klioner, S. A., Lammers, U., Lindegren, L., Luri, X., Mignard, F., Panem, C., Pourbaix, D., Randich, S., Sartoretti, P., Siddiqui, H. I., Soubiran, C., van Leeuwen, F., Walton, N. A., Arenou, F., Bastian, U., Cropper, M., Drimmel, R., Katz, D., Lattanzi, M. G., Bakker, J., Cacciari, C., Castañeda, J., Chaoul, L., Cheek, N., De Angeli, F., Fabricius, C., Guerra, R., Holl, B., Masana, E., Messineo, R., Mowlavi, N., Nienartowicz, K., Panuzzo, P., Portell, J., Riello, M., Seabroke, G. M., Tanga, P., Thévenin, F., Gracia-Abril, G., Comoretto, G., Garcia-Reinaldos, M., Teyssier, D., Altmann, M., Andrae, R., Audard, M., Bellas-Velidis, I., Benson, K., Berthier, J., Blomme, R., Burgess, P., Busso, G., Carry, B., Cellino, A., Clementini, G., Clotet, M., Creevey, O., Davidson, M., De Ridder, J., Delchambre, L., Dell'Oro, A., Ducourant, C., Fernández-Hernández, J., Fouesneau, M., Frémat, Y., Galluccio, L., García-Torres, M., González-Núñez, J., González-Vidal, J. J., Gosset, E., Guy, L. P., Halbwachs, J. L., Hambly, N. C., Harrison, D. L., Hernández, J., Hestroffer, D., Hodgkin, S. T., Hutton, A., Jasniewicz, G., Jean-Antoine-Piccolo, A., Jordan, S., Korn, A. J., Krone-Martins, A., Lanzafame, A. C., Lebzelter, T., Löffler, W., Manteiga, M., Marrese, P. M., Martín-Fleitas, J. M., Moitinho, A., Mora, A., Muinonen, K., Osinde, J., Pancino, E., Pauwels, T., Petit, J. M., Recio-Blanco, A., Richards, P. J., Rimoldini, L., Robin, A. C., Sarro, L. M., Siopis, C., Smith, M., Sozzetti, A., Süveges, M., Torra, J., van Reeven, W., Abbas, U., Abreu Aramburu, A., Accart, S., Aerts, C., Altavilla, G., Álvarez, M. A., Alvarez, R., Alves, J., Anderson, R. I., Andrei, A. H., Anglada Varela, E., Antiche, E., Antoja, T., Arcay, B., Astraatmadja, T. L., Bach, N., Baker, S. G., Balaguer-Núñez, L., Balm, P., Barache, C., Barata, C., Barbato, D., Barblan, F., Barklem, P. S., Barrado, D., Barros, M., Barstow, M. A., Bartholomé Muñoz, S., Bassilana, J. L., Becciani, U., Bellazzini, M., Berihuete, A., Bertone, S., Bianchi, L., Bienaymé, O., Blanco-Cuaresma, S., Boch, T., Boeche, C., Bombrun, A., Borrachero, R., Bossini, D., Bouquillon, S., Bourda, G., Bragaglia, A., Bramante, L., Breddels, M. A., Bressan, A., Brouillet, N., Brüsemeister, T., Brugaletta, E., Bucciarelli, B., Burlacu, A., Busonero, D., Butkevich, A. G., Buzzi, R., Caffau, E., Cancelliere, R., Cannizzaro, G., Cantat-Gaudin, T., Carballo, R., Carlucci, T., Carrasco, J. M., Casamiquela, L., Castellani, M., Castro-Ginard, A., Charlot, P., Chemin, L., Chiavassa, A., Cocozza, G., Costigan, G., Cowell, S., Crifo, F., Crosta, M., Crowley, C., Cuypers, J., Dafonte, C., Damerdji, Y., Dapergolas, A., David, P., David, M., de Laverny, P., De Luise, F., De March, R., de Martino, D., de Souza, R., de Torres, A., Debosscher, J., del Pozo, E., Delbo, M., Delgado, A., Delgado, H. E., Di Matteo, P., Diakite, S., Diener, C., Distefano, E., Dolding, C., Drazinos, P., Durán, J., Edvardsson, B., Enke, H., Eriksson, K., Esquej, P., Eynard Bontemps, G., Fabre, C., Fabrizio, M., Faigler, S., Falcão, A. J., Farràs Casas, M., Federici, L., Fedorets, G., Fernique, P., Figueras, F., Filippi, F., Findeisen, K., Fonti, A., Fraile, E., Fraser, M., Frézouls, B., Gai, M., Galleti, S., Garabato, D., García-Sedano, F., Garofalo, A., Garralda, N., Gavel, A., Gavras, P., Gerssen, J., Geyer, R., Giacobbe, P., Gilmore, G., Girona, S., Giuffrida, G., Glass, F., Gomes, M., Granvik, M., Gueguen, A., Guerrier, A., Guiraud, J., Gutiérrez-Sánchez, R., Haigron, R., Hatzidimitriou, D., Hauser, M., Haywood, M., Heiter, U., Helmi, A., Heu, J., Hilger, T., Hobbs, D., Hofmann, W., Holland, G., Huckle, H. E., Hypki, A., Icardi, V., Janßen, K., Jevardat de Fombelle, G., Jonker, P. G., Juhász, Á. L., Julbe, F., Karampelas, A., Kewley, A., Klar, J., Kochoska, A., Kohley, R., Kolenberg, K., Kontizas, M., Kontizas, E., Koposov, S. E., Kordopatis, G., Kostrzewa-Rutkowska, Z., Koubsky, P., Lambert, S., Lanza, A. F., Lasne, Y., Lavigne, J. B., Le Fustec, Y., Le Poncin-Lafitte, C., Lebreton, Y., Leccia, S., Leclerc, N., Lecoeur-Taibi, I., Lenhardt, H., Leroux, F., Liao, S., Licata, E., Lindstrøm, H. E. P., Lister, T. A., Livanou, E., Lobel, A., López, M., Managau, S., Mann, R. G., Mantelet, G., Marchal, O., Marchant, J. M., Marconi, M., Marinoni, S., Marschalkó, G., Marshall, D. J., Martino, M., Marton, G., Mary, N., Massari, D., Matijevič, G., Mazeh, T., McMillan, P. J., Messina, S., Michalik, D., Millar, N. R., Molina, D., Molinaro, R., Molnár, L., Montegriffo, P., Mor, R., Morbidelli, R., Morel, T., Morris, D., Mulone, A. F., Muraveva, T., Musella, I., Nelemans, G., Nicastro, L., Noval, L., O'Mullane, W., Ordénovic, C., Ordóñez-Blanco, D., Osborne, P., Pagani, C., Pagano, I., Pailler, F., Palacin, H., Palaversa, L., Panahi, A., Pawlak, M., Piersimoni, A. M., Pineau, F. X., Plachy, E., Plum, G., Poggio, E., Poujoulet, E., Prša, A., Pulone, L., Racero, E., Ragaini, S., Rambaux, N., Ramos-Lerate, M., Regibo, S., Reylé, C., Riclet, F., Ripepi, V., Riva, A., Rivard, A., Rixon, G., Roegiers, T., Roelens, M., Romero-Gómez, M., Rowell, N., Royer, F., Ruiz-Dern, L., Sadowski, G., Sagristà Sellés, T., Sahlmann, J., Salgado, J., Salguero, E., Sanna, N., Santana-Ros, T., Sarasso, M., Savietto, H., Schultheis, M., Sciacca, E., Segol, M., Segovia, J. C., Ségransan, D., Shih, I. C., Siltala, L., Silva, A. F., Smart, R. L., Smith, K. W., Solano, E., Solitro, F., Sordo, R., Soria Nieto, S., Souchay, J., Spagna, A., Spoto, F., Stampa, U., Steele, I. A., Steidelmüller, H.,

Stephenson, C. A., Stoev, H., Suess, F. F., Surdej, J., Szabados, L., Szegedi-Elek, E., Tapiador, D., Taris, F., Tauran, G., Taylor, M. B., Teixeira, R., Terrett, D., Teyssandier, P., Thuillot, W., Titarenko, A., Torra Clotet, F., Turon, C., Ulla, A., Utrilla, E., Uzzi, S., Vaillant, M., Valentini, G., Valette, V., van Elteren, A., Van Hemelryck, E., van Leeuwen, M., Vaschetto, M., Vecchiato, A., Veljanoski, J., Viala, Y., Vicente, D., Vogt, S., von Essen, C., Voss, H., Votruba, V., Voutsinas, S., Walmsley, G., Weiler, M., Wertz, O., Wevers, T., Wyrzykowski, Ł., Yoldas, A., Žerjal, M., Ziaeepour, H., Zorec, J., Zschocke, S., Zucker, S., Zurbach, C., and Zwitter, T. (2018). Gaia Data Release 2. Summary of the contents and survey properties. , 616:A1.

Galarza, J. Y., López-Valdivia, R., Meléndez, J., and Lorenzo-Oliveira, D. (2021). Evidence of Rocky Planet Engulfment in the Wide Binary System HIP 71726/HIP 71737. , 922(2):129.

Garcia-Segura, G., Langer, N., Rożyczka, M., and Franco, J. (1999). Shaping Bipolar and Elliptical Planetary Nebulae: Effects of Stellar Rotation, Photoionization Heating, and Magnetic Fields. *The Astrophysical Journal*, 517(2):767–781.

Garcia-Segura, G., Lopez, J. A., and Franco, J. (2005). Magnetically Driven Winds from Post–Asymptotic Giant Branch Stars: Solutions for High-Speed Winds and Extreme Collimation. *The Astrophysical Journal*, 618(2):919–925.

Gebran, M., Agüeros, M. A., Hawkins, K., Schuler, S. C., and Morris, B. M. (2019). Pushing Automated Abundance Derivations into the Cool Dwarf Regime: A Test Using Three G and Two K Stars in Praesepe. , 871(2):142.

Geller, A. M., Latham, D. W., and Mathieu, R. D. (2015). Stellar Radial Velocities in the Old Open Cluster M67 (NGC 2682). I. Memberships, Binaries, and Kinematics. , 150(3):97.

Gesicki, K., Zijlstra, A. A., and Miller Bertolami, M. M. (2018). The mysterious age invariance of the planetary nebula luminosity function bright cut-off. *Nature Astronomy*, 2(7):580–584.

Gledhill, T. M., Froebrich, D., Campbell-White, J., and Jones, A. M. (2018). Planetary nebulae in the UWISH2 survey. *Monthly Notices of the Royal Astronomical Society*, 479(3):3759–3777.

González-Díaz, D., Moni Bidin, C., Silva-Villa, E., Carraro, G., Majaess, D., Moitinho, A., Orquera-Rojas, C., Morales Marín, C. A. L., and Morales-Campaña, E. (2019). Solving the distance discrepancy for the open cluster NGC 2453. The planetary nebula NGC 2452 is not a cluster member. , 626:A10.

Gould, A., Ryu, Y.-H., Calchi Novati, S., Zang, W., Albrow, M. D., Chung, S.-J., Han, C., Hwang, K.-H., Jung, Y. K., Shin, I.-G., Shvartzvald, Y., Yee, J. C., Cha, S.-M., Kim, D.-J., Kim, H.-W., Kim, S.-L., Lee, C.-U., Lee, D.-J., Lee, Y., Park, B.-G., Pogge, R. W., Beichman, C., Bryden, G., Carey, S., Gaudi, B. S., Henderson, C. B., Zhu, W., Fouque, P., Penny, M. T., Petric, A., Burdullis, T., and Mao, S. (2020). KMT-2018-BLG-0029Lb: A Very Low Mass-Ratio Spitzer Microlens Planet. *Journal of Korean Astronomical Society*, 53:9–26.

Graczyk, D., Pietrzyński, G., Thompson, I. B., Gieren, W., Pilecki, B., Konorski, P., Udalski, A., Soszyński, I., Villanova, S., Górski, M., Suchomska, K., Karczmarek, P., Kudritzki, R. P., Bresolin, F., and Gallenne, A. (2014). The araucaria project. the distance to the small magellanic cloud from late-type eclipsing binaries. *Astrophysical Journal*, 780(1):59.

Grevesse, N. and Sauval, A. J. (1998). Standard Solar Composition. *Space Science Reviews*, 85(1):161–174.

Gurzadian, G. A. (1962). The magnetic fields in planetary nebulae. *Vistas in Astronomy*, 5(C):40–57.

Gustafsson, B. (1998). Is the Sun a Sun-Like Star? , 85:419–428.

Haworth, T. J., Clarke, C. J., Rahman, W., Winter, A. J., and Facchini, S. (2018). The FRIED grid of mass-loss rates for externally irradiated protoplanetary discs. , 481(1):452–466.

Henden, A. A., Welch, D. L., Terrell, D., and Levine, S. E. (2009). The AAVSO Photometric All-Sky Survey (APASS). In *American Astronomical Society Meeting Abstracts #214*, volume 214 of *American Astronomical Society Meeting Abstracts*, page 407.02.

Holweger, H. (2001). Photospheric abundances: Problems, updates, implications. In Wimmer-Schweingruber, R. F., editor, *AIP Conference Proceedings*, volume 598, pages 23–30.

Hunter, J. D., Asnicar, F., Manghi, P., Pasolli, E., Tett, A., and Segata, N. (2007). Matplotlib: A 2D Graphics Environment. *Computing in Science & Engineering*, 9(3):90–95.

Hurley-Keller, D. and Morrison, H. L. (2004). Planetary Nebula Kinematics in M31. *The Astrophysical Journal*, 616(Freeman 1996):804–820.

Iben, I. (1995). Planetary nebulae and their central stars — origin and evolution. *Physics Reports*, 250(1-2):1–94.

Iłkiewicz, K. and Mikołajewska, J. (2017). Distinguishing between symbiotic stars and planetary nebulae. *Astronomy & Astrophysics*, 606:A110.

Jacob, R., Schönberner, D., and Steffen, M. (2013). The evolution of planetary nebulae. VIII. True expansion rates and visibility times. *Astronomy & Astrophysics*, 558:A78.

Jacoby, G. H. and Ford, H. C. (1986). Chemical abundances of planetary nebulae in M31. *The Astrophysical Journal*, 304:490.

Johansen, A., Davies, M. B., Church, R. P., and Holmelin, V. (2012). Can Planetary Instability Explain the Kepler Dichotomy? , 758(1):39.

Johnson, J. A., Aller, K. M., Howard, A. W., and Crepp, J. R. (2010). Giant Planet Occurrence in the Stellar Mass-Metallicity Plane. , 122(894):905.

Johnson, J. A., Ivans, I. I., and Stetson, P. B. (2006). Chemical Compositions of Red Giant Stars in Old Large Magellanic Cloud Globular Clusters. , 640(2):801–822.

Jones, E., Oliphant, T., Peterson, P., and Others (2001). SciPy: Open source scientific tools for Python.

Kang, W. and Lee, S.-G. (2012). Tool for Automatic Measurement of Equivalent width (TAME). , 425(4):3162–3171.

Khromov, G. S. (1989). Planetary nebulae. *Space Science Reviews*, 51(3-4):339–423.

Kniazev, A. Y., Grebel, E. K., Zucker, D. B., Rix, H. W., Martínez-Delgado, D., and Snedden, S. A. (2014). A search for planetary nebulae with the sloan digital sky survey: The outer regions of M31. *Astronomical Journal*, 147(1):16.

Kniazev, A. Y., Zijlstra, A. A., Grebel, E. K., Pilyugin, L. S., Pustilnik, S., Väisänen, P., Buckley, D., Hashimoto, Y., Loaring, N., Romero, E., Still, M., Burgh, E. B., and Nordsieck, K. (2008). The metallicity extremes of the Sagittarius dSph: SALT spectroscopy of PNe. *Monthly Notices of the Royal Astronomical Society*, 388(4):1667–1678.

Konopacky, Q. M., Ghez, A. M., Barman, T. S., Rice, E. L., Bailey, J. I., I., White, R. J., McLean, I. S., and Duchêne, G. (2010). High-precision Dynamical Masses of Very Low Mass Binaries. , 711(2):1087–1122.

Kovalev, M., Bergemann, M., Ting, Y.-S., and Rix, H.-W. (2019). Non-LTE chemical abundances in Galactic open and globular clusters. , 628:A54.

Kroupa, P. (2001). On the variation of the initial mass function. , 322(2):231–246.

Kupka, F., Piskunov, N., Ryabchikova, T. A., Stempels, H. C., and Weiss, W. W. (1999). VALD-2: Progress of the Vienna Atomic Line Data Base. , 138:119–133.

Kurucz, R. (1993). ATLAS9 Stellar Atmosphere Programs and 2 km/s grid. *ATLAS9 Stellar Atmosphere Programs and 2 km/s grid. Kurucz CD-ROM No. 13. Cambridge*, 13.

Kwitter, K. B., Lehman, E. M., Balick, B., and Henry, R. B. (2012). Abundances of planetary nebulae in the outer disk of M31. *Astrophysical Journal*, 753(1):12.

Kwok, S., Purton, C. R., and Fitzgerald, P. M. (1978). On the origin of planetary nebulae. *The Astrophysical Journal*, 219:L125.

Lin, D. N. C., Bodenheimer, P., and Richardson, D. C. (1996). Orbital migration of the planetary companion of 51 Pegasi to its present location. , 380(6575):606–607.

Liu, F., Asplund, M., Yong, D., Feltzing, S., Dotter, A., Meléndez, J., and Ramírez, I. (2019). Chemical (in)homogeneity and atomic diffusion in the open cluster M 67. , 627:A117.

Liu, F., Asplund, M., Yong, D., Meléndez, J., Ramírez, I., Karakas, A. I., Carlos, M., and Marino, A. F. (2016a). The chemical compositions of solar twins in the open cluster M67. , 463(1):696–704.

Liu, F., Yong, D., Asplund, M., Ramírez, I., and Meléndez, J. (2016b). The Hyades open cluster is chemically inhomogeneous. , 457(4):3934–3948.

LSST Science Collaboration, Abell, P. A., Allison, J., Anderson, S. F., Andrew, J. R., Angel, J. R. P., Armus, L., Arnett, D., Asztalos, S. J., Axelrod, T. S., Bailey, S., Ballantyne, D. R., Bankert, J. R., Barkhouse, W. A., Barr, J. D., Barrientos, L. F., Barth, A. J., Bartlett, J. G., Becker, A. C., Becla, J., Beers, T. C., Bernstein, J. P., Biswas, R., Blanton, M. R., Bloom, J. S., Bochanski, J. J., Boeshaar, P., Borne, K. D., Bradac, M., Brandt, W. N., Bridge, C. R., Brown, M. E., Brunner, R. J., Bullock, J. S., Burgasser, A. J., Burge, J. H., Burke, D. L., Cargile, P. A., Chandrasekharan, S., Chartas, G., Chesley, S. R., Chu, Y.-H., Cinabro, D., Claire, M. W., Claver, C. F., Clowe, D., Connolly, A. J., Cook, K. H., Cooke, J., Cooray, A., Covey, K. R., Culliton, C. S., de Jong, R., de Vries, W. H., Debattista, V. P., Delgado, F., Dell'Antonio, I. P., Dhital, S., Di Stefano, R., Dickinson, M., Dilday, B., Djorgovski, S. G., Dobler, G., Donalek, C., Dubois-Felsmann, G., Durech, J., Eliasdottir, A., Eracleous, M., Eyer, L., Falco, E. E., Fan, X., Fassnacht, C. D., Ferguson, H. C., Fernandez, Y. R., Fields, B. D., Finkbeiner, D., Figueroa, E. E., Fox, D. B., Francke, H., Frank, J. S., Frieman, J., Fromenteau, S., Furqan, M., Galaz, G., Gal-Yam, A., Garnavich, P., Gawiser, E., Geary, J., Gee, P., Gibson, R. R., Gilmore, K., Grace, E. A., Green, R. F., Gressler, W. J., Grillmair, C. J., Habib, S., Haggerty, J. S., Hamuy, M., Harris, A. W., Hawley, S. L., Heavens, A. F., Hebb, L., Henry, T. J., Hileman, E., Hilton, E. J., Hoadley, K., Holberg, J. B., Holman, M. J., Howell, S. B., Infante, L., Ivezic, Z., Jacoby, S. H., Jain, B., R, Jedicke, Jee, M. J., Jernigan, J. G., Jha, S. W., Johnston, K. V., Jones, R. L., Juric, M., Kaasalainen, M., Styliani, Kafka, Kahn, S. M., Kaib, N. A., Kalirai, J., Kantor, J., Kasliwal, M. M., Keeton, C. R., Kessler, R., Knezevic, Z., Kowalski, A., Krabbendam, V. L., Krughoff, K. S., Kulkarni, S., Kuhlman, S., Lacy, M., Lepine, S., Liang, M., Lien, A., Lira, P., Long, K. S., Lorenz, S., Lotz, J. M., Lupton, R. H., Lutz, J., Macri, L. M., Mahabal, A. A., Mandelbaum, R., Marshall, P., May, M., McGehee, P. M., Meadows, B. T., Meert, A., Milani, A., Miller, C. J., Miller, M., Mills, D., Minniti, D., Monet, D., Mukadam, A. S., Nakar, E., Neill, D. R., Newman, J. A., Nikolaev, S., Nordby, M., O'Connor, P., Oguri, M., Oliver, J., Olivier, S. S., Olsen, J. K., Olsen, K., Olszewski, E. W., Oluseyi, H., Padilla, N. D., Parker, A., Pepper, J., Peterson, J. R., Petry, C., Pinto, P. A., Pizagno, J. L., Popescu, B., Prsa, A., Radcka, V., Raddick, M. J., Rasmussen, A., Rau, A., Rho, J., Rhoads, J. E., Richards, G. T., Ridgway, S. T., Robertson, B. E., Roskar, R., Saha, A., Sarajedini, A., Scannapieco, E., Schalk, T., Schindler, R., Schmidt, S., Schmidt, S., Schneider, D. P., Schumacher, G., Scranton, R., Sebag, J., Seppala, L. G., Shemmer, O., Simon, J. D., Sivertz, M., Smith, H. A., Smith, J. A., Smith, N., Spitz, A. H., Stanford, A., Stassun, K. G., Strader, J., Strauss, M. A., Stubbs, C. W., Sweeney, D. W., Szalay, A., Szkody, P., Takada, M., Thorman, P., Trilling, D. E., Trimble, V., Tyson, A., Van Berg, R., Berk, D. V., VanderPlas, J., Verde, L., Vrsnak, B., Walkowicz, L. M., Wandelt, B. D., Wang, S., Wang, Y., Warner, M., Wechsler, R. H., West, A. A., Wiecha, O., Williams, B. F., Willman, B., Wittman, D., Wolff, S. C., Wood-Vasey, W. M., Wozniak, P., Young, P., Zentner, A., and Zhan, H. (2009). LSST Science Book, Version 2.0. *LSST Corporation*.

Lum, M. G. and Boesgaard, A. M. (2019). A Comparison of the Chemical Composition of Main-sequence and Giant Stars in the Open Cluster NCC 752. , 878(2):99.

Macintosh, B., Graham, J. R., Barman, T., De Rosa, R. J., Konopacky, Q., Marley, M. S., Marois, C., Nielsen, E. L., Pueyo, L., Rajan, A., Rameau, J., Saumon, D., Wang, J. J., Patience, J., Ammons, M., Arriaga, P., Artigau, E., Beckwith, S., Brewster, J., Bruzzone, S., Bulger, J., Burningham, B., Burrows, A. S., Chen, C., Chiang, E., Chilcote, J. K., Dawson, R. I., Dong, R., Doyon, R., Draper, Z. H., Duchêne, G., Esposito, T. M., Fabrycky, D., Fitzgerald, M. P., Follette, K. B., Fortney, J. J., Gerard, B., Goodsell,

S., Greenbaum, A. Z., Hibon, P., Hinkley, S., Cotten, T. H., Hung, L. W., Ingraham, P., Johnson-Groh, M., Kalas, P., Lafreniere, D., Larkin, J. E., Lee, J., Line, M., Long, D., Maire, J., Marchis, F., Matthews, B. C., Max, C. E., Metchev, S., Millar-Blanchaer, M. A., Mittal, T., Morley, C. V., Morzinski, K. M., Murray-Clay, R., Oppenheimer, R., Palmer, D. W., Patel, R., Perrin, M. D., Poyneer, L. A., Rafikov, R. R., Rantakyrö, F. T., Rice, E. L., Rojo, P., Rudy, A. R., Ruffio, J. B., Ruiz, M. T., Sadakuni, N., Saddlemyer, L., Salama, M., Savransky, D., Schneider, A. C., Sivaramakrishnan, A., Song, I., Soummer, R., Thomas, S., Vasisht, G., Wallace, J. K., Ward-Duong, K., Wiktorowicz, S. J., Wolff, S. G., and Zuckerman, B. (2015). Discovery and spectroscopy of the young jovian planet 51 Eri b with the Gemini Planet Imager. *Science*, 350(6256):64–67.

Mack, C. E., Schuler, S. C., Stassun, K. G., and Norris, J. (2014). Detailed abundances of planet-hosting wide binaries. I. Did planet formation imprint chemical signatures in the atmospheres of HD 20782/81? *Astrophysical Journal*, 787(2):98.

Mack, Claude E., I., Schuler, S. C., Stassun, K. G., and Norris, J. (2014). Detailed Abundances of Planet-hosting Wide Binaries. I. Did Planet Formation Imprint Chemical Signatures in the Atmospheres of HD 20782/81? , 787(2):98.

Mack, Claude E., I., Stassun, K. G., Schuler, S. C., Hebb, L., and Pepper, J. A. (2016). Detailed Abundances of Planet-hosting Wide Binaries. II. HD80606+HD80607. , 818(1):54.

Mack III, C. E., Stassun, K. G., Schuler, S. C., Hebb, L., and Pepper, J. A. (2016). Detailed Abundances of Planet-Hosting Wide Binaries. Ii. Hd 80606+Hd 80607. *The Astrophysical Journal*, 818(1):54.

MacLean, B. T., De Silva, G. M., and Lattanzio, J. (2015). O, Na, Ba and Eu abundance patterns in open clusters. , 446(4):3556–3561.

Magrini, L. and Gonçalves, D. R. (2009). IC10: The history of the nearest starburst galaxy through its Planetary Nebula and H ii region populations. *Monthly Notices of the Royal Astronomical Society*, 398(1):280–292.

Majaess, D., Dékány, I., Hajdu, G., Minniti, D., Turner, D., and Gieren, W. (2018). Establishing the Galactic Centre distance using VVV Bulge RR Lyrae variables. *Astrophysics and Space Science*, 363(6):127.

Martin, C., Barlow, T., Barnhart, W., Bianchi, L., Blakkolb, B. K., Bruno, D., Bushman, J., Byun, Y.-I., Chiville, M., Conrow, T., Cooke, B., Donas, J., Fanson, J. L., Forster, K., Friedman, P. G., Grange, R., Griffiths, D., Heckman, T., Lee, J., Jelinsky, P. N., Kim, S.-W., Lee, S.-C., Lee, Y.-W., Liu, D., Madore, B. F., Malina, R., Mazer, A., McLean, R., Milliard, B., Mitchell, W., Morais, M., Morrissey, P. F., Neff, S. G., Raison, F., Randall, D., Rich, M., Schiminovich, D., Schmitigal, W., Sen, A., Siegmund, O. H. W., Small, T., Stock, J. M., Surber, F., Szalay, A., Vaughan, A. H., Weigand, T., Welsh, B. Y., Wu, P., Wyder, T., Xu, C. K., and Zsoldas, J. (2003). The Galaxy Evolution Explorer. In Blades, J. C. and Siegmund, O. H. W., editors, *Future EUV/UV and Visible Space Astrophysics Missions and Instrumentation.*, volume 4854 of *Society of Photo-Optical Instrumentation Engineers (SPIE) Conference Series*, pages 336–350.

Matt, S., Ls, C., Frank, A., and Blackman, E. (2004). The Last Hurrah : PPN Formation by a Magnetic Explosion. In Meixner, M., Kastner, J. H., Balick, B., and Soker, N., editors, *Asymmetrical Planetary Nebulae III: Winds, Structure and the Thunderbird*, volume 313, pages 449–455.

Maurya, J. and Joshi, Y. C. (2020). Photometric and kinematic study of the three intermediate age open clusters NGC 381, NGC 2360, and Berkeley 68. , 494(4):4713–4729.

Mayor, M. and Queloz, D. (1995). A Jupiter-mass companion to a solar-type star. , 378(6555):355–359.

McDonough, W. F. (2001). The Composition of the Earth's Core. In *Lunar and Planetary Science Conference*, Lunar and Planetary Science Conference, page 2005.

Meibom, S., Torres, G., Fressin, F., Latham, D. W., Rowe, J. F., Ciardi, D. R., Bryson, S. T., Rogers, L. A., Henze, C. E., Janes, K., Barnes, S. A., Marcy, G. W., Isaacson, H., Fischer, D. A., Howell, S. B., Horch, E. P., Jenkins, J. M., Schuler, S. C., and Crepp, J. (2013). The same frequency of planets inside and outside open clusters of stars. , 499(7456):55–58.

Meléndez, J., Asplund, M., Gustafsson, B., and Yong, D. (2009). The peculiar solar composition and its possible relation to planet formation. *Astrophysical Journal*, 704(1 PART 2):L66–L70.

Meléndez, J., Asplund, M., Gustafsson, B., and Yong, D. (2009). The Peculiar Solar Composition and Its Possible Relation to Planet Formation. , 704(1):L66–L70.

Merrett, H. R., Merrifield, M. R., Douglas, N. G., Kuijken, K., Romanowsky, A. J., Napolitano, N. R., Arnaboldi, M., Capaccioli, M., Freeman, K. C., Gerhard, O., Coccato, L., Carter, D., Evans, N. W., Wilkinson, M. I., Halliday, C., and Bridges, T. J. (2006). A deep kinematic survey of planetary nebulae in the Andromeda galaxy using the Planetary Nebula Spectrograph. *Monthly Notices of the Royal Astronomical Society*, 369(1):120–142.

Miller Bertolami, M. M. (2016). New models for the evolution of post-asymptotic giant branch stars and central stars of planetary nebulae. *Astronomy & Astrophysics*, 588:A25.

Milliman, K. E., Mathieu, R. D., and Schuler, S. C. (2015). Barium Surface Abundances of Blue Stragglers in the Open Cluster NGC 6819. , 150(3):84.

Moe, M. and De Marco, O. (2006). Do Most Planetary Nebulae Derive from Binaries? I. Population Synthesis Model of the Galactic Planetary Nebula Population Produced by Single Stars and Binaries. *The Astrophysical Journal*, 650(2):916–932.

Monteiro, H. and Dias, W. S. (2019). Distances and ages from isochrone fits of 150 open clusters using Gaia DR2 data. , 487(2):2385–2406.

Morisset, C. (2013). pyCloudy: Tools to manage astronomical Cloudy photoionization. Astrophysics Source Code Library.

Morris, M. and Montez, R. (2015). Exploring the Late Evolutionary Stages of Sun-like Stars with LSST. In *American Astronomical Society Meeting Abstracts #225*, volume 225 of *American Astronomical Society Meeting Abstracts*, page 139.07.

Naoz, S. (2016). The Eccentric Kozai-Lidov Effect and Its Applications. , 54:441–489.

Nolthenius, R. and Ford, H. C. (1987). Dynamics of the outer disk and halo of M31. *The Astrophysical Journal*, 317:62.

Nordhaus, J., Blackman, E. G., and Frank, A. (2007). Isolated versus common envelope dynamos in planetary nebula progenitors. *Monthly Notices of the Royal Astronomical Society*, 376(2):599–608.

Oke, J. B. and Gunn, J. E. (1983). Secondary standard stars for absolute spectrophotometry. *The Astrophysical Journal*, 266:713.

Pace, G., Pasquini, L., and François, P. (2008). Abundances of four open clusters from solar stars. , 489(1):403–412.

Pacucci, F., Ferrara, A., and D'Onghia, E. (2013). Detectability of Free Floating Planets in Open Clusters with the James Webb Space Telescope. , 778(2):L42.

Parker, Q. A., Bojičić, I. S., and Frew, D. J. (2016). HASH: the Hong Kong/AAO/Strasbourg H{\ensuremath{\alpha}} planetary nebula database. In *Journal of Physics Conference Series*, volume 728 of *Journal of Physics Conference Series*, page 32008.

Parker, Q. A., Phillipps, S., Pierce, M. J., Hartley, M., Hambly, N. C., Read, M. A., MacGillivray, H. T., Tritton, S. B., Cass, C. P., Cannon, R. D., Cohen, M., Drew, J. E., Frew, D. J., Hopewell, E., Mader, S., Malin, D. F., Masheder, M. R., Morgan, D. H., Morris, R. A., Russeil, D., Russell, K. S., and Walker, R. N. (2005). The AAO/UKST SuperCOSMOS Hα survey. *Monthly Notices of the Royal Astronomical Society*, 362(2):689–710.

Pastorello, N., Sarzi, M., Cappellari, M., Emsellem, E., Mamon, G. A., Bacon, R., Davies, R. L., and Tim de Zeeuw, P. (2013). The planetary nebulae population in the nuclear regions of M31: The SAURON view. *Monthly Notices of the Royal Astronomical Society*, 430(2):1219–1229.

Peng, E. W., Ford, H. C., and Freeman, K. C. (2004). The Globular Cluster System of NGC 5128. II. Ages, Metallicities, Kinematics, and Formation. *The Astrophysical Journal*, 602(2):705–722.

Pérez, F. and Granger, B. E. (2007). IPython: A system for interactive scientific computing. *Computing in Science and Engineering*, 9(3):21–29.

Perinotto, M., Schönberner, D., Steffen, M., and Calonaci, C. (2004). The evolution of planetary nebulae. I. A radiation-hydrodynamics parameter study. *Astronomy & Astrophysics*, 414(3):993–1015.

Pfalzner, S., Bhandare, A., and Vincke, K. (2018). Did a stellar fly-by shape the planetary system around Pr 0211 in the cluster M44? , 610:A33.

Pfalzner, S. and Vincke, K. (2020). Cradle(s) of the Sun. , 897(1):60.

Phillips, J. P. (2007). Density gradients in Galactic planetary nebulae. *Monthly Notices of the Royal Astronomical Society*, 378(1):231–238.

Pietrzyński, G., Graczyk, D., Gieren, W., Thompson, I. B., Pilecki, B., Udalski, A., Soszyński, I., Kozłowski, S., Konorski, P., Suchomska, K., Bono, G., Moroni, P. G., Villanova, S., Nardetto, N., Bresolin, F., Kudritzki, R. P., Storm, J., Gallenne, A., Smolec, R., Minniti, D., Kubiak, M., Szymański, M. K., Poleski, R., Wyrzykowski, Ulaczyk, K., Pietrukowicz, P., Górski, M., and Karczmarek, P. (2013). An eclipsing-binary distance to the large magellanic cloud accurate to two per cent. *Nature*, 495(7439):76–79.

Pinsonneault, M. H., DePoy, D. L., and Coffee, M. (2001). The Mass of the Convective Zone in FGK Main-Sequence Stars and the Effect of Accreted Planetary Material on Apparent Metallicity Determinations. , 556(1):L59–L62.

Piskunov, N. E., Kupka, F., Ryabchikova, T. A., Weiss, W. W., and Jeffery, C. S. (1995). VALD: The Vienna Atomic Line Data Base. , 112:525.

Prochaska, J. X. and McWilliam, A. (2000). On the Perils of Hyperfine Splitting: A Reanalysis of MN and SC Abundance Trends. , 537(1):L57–L60.

Quinn, S. N., White, R. J., Latham, D. W., Buchhave, L. A., Cantrell, J. R., Dahm, S. E., Fűrész, G., Szentgyorgyi, A. H., Geary, J. C., Torres, G., Bieryla, A., Berlind, P., Calkins, M. C., Esquerdo, G. A., and Stefanik, R. P. (2012). Two "b"s in the Beehive: The Discovery of the First Hot Jupiters in an Open Cluster. , 756(2):L33.

Ramírez, I., Khanal, S., Aleo, P., Sobotka, A., Liu, F., Casagrande, L., Meléndez, J., Yong, D., Lambert, D. L., and Asplund, M. (2015). The Dissimilar Chemical Composition of the Planet-hosting Stars of the XO-2 Binary System. , 808(1):13.

Ramírez, I., Khanal, S., Lichon, S. J., Chanamé, J., Endl, M., Meléndez, J., and Lambert, D. L. (2019). The chemical composition of HIP 34407/HIP 34426 and other twin-star comoving pairs. , 490(2):2448–2457.

Ramírez, I., Meléndez, J., and Asplund, M. (2009). Accurate abundance patterns of solar twins and analogs. *Astronomy & Astrophysics*, 508(1):L17–L20.

Ramírez, I., Meléndez, J., and Asplund, M. (2009). Accurate abundance patterns of solar twins and analogs. Does the anomalous solar chemical composition come from planet formation? , 508(1):L17–L20.

Ramírez, I., Meléndez, J., Cornejo, D., Roederer, I. U., and Fish, J. R. (2011). Elemental Abundance Differences in the 16 Cygni Binary System: A Signature of Gas Giant Planet Formation? , 740(2):76.

Reddy, A. B. S., Giridhar, S., and Lambert, D. L. (2015). Comprehensive abundance analysis of red giants in the open clusters NGC 1342, 1662, 1912, 2354 and 2447. , 450(4):4301–4322.

Richer, M., McCall, M. L., and Stasińska, G. (1998). The chemical evolution of dynamically hot galaxies. *Astronomy and Astrophysics*, 340:67–76.

Rodríguez-Flores, E. R., Corradi, R. L. M., Mampaso, A., García-Alvarez, D., Munari, U., Greimel, R., Rubio-Díez, M. M., and Santander-García, M. (2014). IPHAS and the symbiotic stars. III. New discoveries and their IR spectral energy distributions. *Astronomy and Astrophysics*, 567:A49.

Saffe, C., Flores, M., and Buccino, A. (2015). HD 80606: searching for the chemical signature of planet formation. , 582:A17.

Saffe, C., Jofré, E., Martioli, E., Flores, M., Petrucci, R., and Jaque Arancibia, M. (2017). Signatures of rocky planet engulfment in HAT-P-4. Implications for chemical tagging studies. , 604:L4.

Sahlmann, J., Lazorenko, P. F., Ségransan, D., Martín, E. L., Queloz, D., Mayor, M., and Udry, S. (2013). Astrometric orbit of a low-mass companion to an ultracool dwarf. , 556:A133.

Salpeter, E. E. (1955). The Luminosity Function and Stellar Evolution. , 121:161.

Sanders, N. E., Caldwell, N., McDowell, J., and Harding, P. (2012). The metallicity profile of M31 from spectroscopy of hundreds of H II regions and PNe. *Astrophysical Journal*, 758(2):133.

Sandquist, E. L., Jessen-Hansen, J., Shetrone, M. D., Brogaard, K., Meibom, S., Leitner, M., Stello, D., Bruntt, H., Antoci, V., Orosz, J. A., Grundahl, F., and Frandsen, S. (2016). The Age and Distance of the Kepler Open Cluster NGC 6811 from an Eclipsing Binary, Turnoff Star Pulsation, and Giant Asteroseismology. , 831(1):11.

Saviane, I., Exter, K., Tsamis, Y., Gallart, C., and Péquignot, D. (2009). VLT/FORS1 spectrophotometry of the first planetary nebula discovered in the Phoenix dwarf galaxy. *Astronomy & Astrophysics*, 494(2):515–525.

Schiller, M., Connelly, J. N., Glad, A. C., Mikouchi, T., and Bizzarro, M. (2015). Early accretion of protoplanets inferred from a reduced inner solar system ^{26}Al inventory. *Earth and Planetary Science Letters*, 420:45–54.

Schmeja, S. and Kimeswenger, S. (2001). Planetary nebula or symbiotic Mira? Near infrared colours mark the difference. *Astronomy & Astrophysics*, 377(2):L18–L21.

Schönberner, D., Jacob, R., and Steffen, M. (2005). The evolution of planetary nebulae III. Internal kinematics and expansion parallaxes. *Astronomy & Astrophysics*, 441(2):573–588.

Schuler, S. C., Cunha, K., Smith, V. V., Ghezzi, L., King, J. R., Deliyannis, C. P., and Boesgaard, A. M. (2011a). Detailed Abundances of the Solar Twins 16 Cygni A and B: Constraining Planet Formation Models. , 737(2):L32.

Schuler, S. C., Cunha, K., Smith, V. V., Ghezzi, L., King, J. R., Deliyannis, C. P., and Boesgaard, A. M. (2011b). Detailed Abundances of the Solar Twins 16 Cygni A and B: Constraining Planet Formation Models. , 737(2):L32.

Schuler, S. C., Flateau, D., Cunha, K., King, J. R., Ghezzi, L., and Smith, V. V. (2011c). Abundances of Stars with Planets: Trends with Condensation Temperature. , 732(1):55.

Schuler, S. C., King, J. R., and The, L.-S. (2009a). Stellar Nucleosynthesis in the Hyades Open Cluster. , 701(1):837–849.

Schuler, S. C., King, J. R., and The, L.-S. (2009b). Stellar Nucleosynthesis in the Hyades Open Cluster. , 701(1):837–849.

Schuler, S. C., Vaz, Z. A., Katime Santrich, O. J., Cunha, K., Smith, V. V., King, J. R., Teske, J. K., Ghezzi, L., Howell, S. B., and Isaacson, H. (2015). Detailed Abundances of Stars with Small Planets Discovered by Kepler. I. The First Sample. , 815(1):5.

Skrutskie, M. F., Cutri, R. M., Stiening, R., Weinberg, M. D., Schneider, S., Carpenter, J. M., Beichman, C., Capps, R., Chester, T., Elias, J., Huchra, J., Liebert, J., Lonsdale, C., Monet, D. G., Price, S., Seitzer, P., Jarrett, T., Kirkpatrick, J. D., Gizis, J. E., Howard, E., Evans, T., Fowler, J., Fullmer, L., Hurt, R., Light, R., Kopan, E. L., Marsh, K. A., McCallon, H. L., Tam, R., Van Dyk, S., and Wheelock, S. (2006). The Two Micron All Sky Survey (2MASS). , 131(2):1163–1183.

Sneden, C., Uomoto, A., Cottrell, P., and Fitzpatrick, M. (2012). SPECTRE: Manipulation of single-order spectra.

Sneden, C. A. (1973). *Carbon and Nitrogen Abundances in Metal-Poor Stars.* PhD thesis, THE UNIVERSITY OF TEXAS AT AUSTIN.

Soker, N. (1997). Properties that Cannot Be Explained by the Progenitors of Planetary Nebulae. *The Astrophysical Journal Supplement Series*, 112(2):487–505.

Soker, N. (2006). Why Magnetic Fields Cannot Be the Main Agent Shaping Planetary Nebulae. *Publications of the Astronomical Society of the Pacific*, 118(840):260–269.

Sousa, S. A. G., Santos, N. C., Monteiro, M. J. P. F. G., Israelian, G., and Mayor, M. (2007). A New Code for Automatic Determination of Equivalent Widths: Automatic Routine for Line Equivalent Widths in Stellar Spectra (ARES). In *JENAM-2007, "Our Non-Stable Universe"*, pages 9–9.

Sousa, S. G., Santos, N. C., Adibekyan, V., Delgado-Mena, E., and Israelian, G. (2015). ARES v2: new features and improved performance. , 577:A67.

Souto, D., Allende Prieto, C., Cunha, K., Pinsonneault, M., Smith, V. V., Garcia-Dias, R., Bovy, J., García-Hernández, D. A., Holtzman, J., Johnson, J. A., Jönsson, H., Majewski, S. R., Shetrone, M., Sobeck, J., Zamora, O., Pan, K., and Nitschelm, C. (2019). Chemical Abundances of Main-sequence, Turnoff, Subgiant, and Red Giant Stars from APOGEE Spectra. II. Atomic Diffusion in M67 Stars. , 874(1):97.

Spina, L., Meléndez, J., Casey, A. R., Karakas, A. I., and Tucci-Maia, M. (2018). Chemical Inhomogeneities in the Pleiades: Signatures of Rocky-forming Material in Stellar Atmospheres. , 863(2):179.

Stassun, K. G. and Torres, G. (2016). Eclipsing Binaries as Benchmarks for Trigonometric Parallaxes in the Gaia Era. , 152(6):180.

Stetson, P. B. and Pancino, E. (2008). DAOSPEC: An Automatic Code for Measuring Equivalent Widths in High-Resolution Stellar Spectra. , 120(874):1332.

Suárez, O., García-Lario, P., Manchado, A., Manteiga, M., Ulla, A., and Pottasch, S. R. (2006). A spectroscopic atlas of post-AGB stars and planetary nebulae selected from the IRAS point source catalogue. *Astronomy & Astrophysics*, 458(1):173–180.

Teske, J. K., Ghezzi, L., Cunha, K., Smith, V. V., Schuler, S. C., and Bergemann, M. (2015). Abundance Differences between Exoplanet Binary Host Stars XO-2N and XO-2S—Dependence on Stellar Parameters. , 801(1):L10.

Toalá, J. A. and Arthur, S. J. (2014). Formation and X-ray emission from hot bubbles in planetary nebulae – I. Hot bubble formation. *Monthly Notices of the Royal Astronomical Society*, 443(4):3486–3505.

Tucci Maia, M., Meléndez, J., and Ramírez, I. (2014). High Precision Abundances in the 16 Cyg Binary System: A Signature of the Rocky Core in the Giant Planet. , 790(2):L25.

van den Bergh, S. (1999). The local group of galaxies. *Astronomy and Astrophysics Review*, 9(3-4):273–318.

Van Der Walt, S., Colbert, S. C., and Varoquaux, G. (2011). The NumPy array: A structure for efficient numerical computation. *Computing in Science and Engineering*.

van Elteren, A., Portegies Zwart, S., Pelupessy, I., Cai, M. X., and McMillan, S. L. W. (2019). Survivability of planetary systems in young and dense star clusters. , 624:A120.

Vassiliadis, E. and Wood, P. R. (1994). Post-asymptotic giant branch evolution of low- to intermediate-mass stars. *The Astrophysical Journal Supplement Series*, 92:125.

Vejar, G., Schuler, S. C., and Stassun, K. G. (2021). Detailed Abundances of Planet-hosting Open Clusters. The Praesepe (Beehive) Cluster. , 919(2):100.

Veyette, M. J., Williams, B. F., Dalcanton, J. J., Balick, B., Caldwell, N., Fouesneau, M., Girardi, L., Gordon, K. D., Kalirai, J., Rosenfield, P., and Seth, A. C. (2014). PANCHROMATIC HUBBLE ANDROMEDA TREASURY. IX. A PHOTOMETRIC SURVEY OF PLANETARY NEBULAE IN M31. *The Astrophysical Journal*, 792(2):121.

Vogt, S. S., Allen, S. L., Bigelow, B. C., Bresee, L., Brown, B., Cantrall, T., Conrad, A., Couture, M., Delaney, C., Epps, H. W., Hilyard, D., Hilyard, D. F., Horn, E., Jern, N., Kanto, D., Keane, M. J., Kibrick, R. I., Lewis, J. W., Osborne, J., Pardeilhan, G. H., Pfister, T., Ricketts, T., Robinson, L. B., Stover, R. J., Tucker, D., Ward, J., and Wei, M. Z. (1994). HIRES: the high-resolution echelle spectrometer on the Keck 10-m Telescope. In Crawford, D. L. and Craine, E. R., editors, *Instrumentation in Astronomy VIII*, volume 2198 of *Society of Photo-Optical Instrumentation Engineers (SPIE) Conference Series*, page 362.

Walsh, J. R., Dudziak, G., Minniti, D., and Zijlstra, A. A. (1997). Chemical Abundances of Planetary Nebulae in the Sagittarius Dwarf Elliptical Galaxy. *The Astrophysical Journal*, 487(2):651–662.

Weisz, D. R., Johnson, L. C., Foreman-Mackey, D., Dolphin, A. E., Beerman, L. C., Williams, B. F., Dalcanton, J. J., Rix, H.-W., Hogg, D. W., Fouesneau, M., Johnson, B. D., Bell, E. F., Boyer, M. L., Gouliermis, D., Guhathakurta, P., Kalirai, J. S., Lewis, A. R., Seth, A. C., and Skillman, E. D. (2015). The High-mass Stellar Initial Mass Function in M31 Clusters. , 806(2):198.

Weston, S., Napiwotzki, R., and Sale, S. (2009). Central stars of Planetary Nebulae in SDSS and IPHAS. *Journal of Physics: Conference Series*, 172:012033.

Wilden, B. S., Jones, B. F., Lin, D. N. C., and Soderblom, D. R. (2002). Evolution of the Lithium Abundance of Solar-Type Stars. X. Does Accretion Affect the Lithium Dispersion in the Pleiades? , 124(5):2799–2812.

Winter, A. J., Clarke, C. J., Rosotti, G., Ih, J., Facchini, S., and Haworth, T. J. (2018). Protoplanetary disc truncation mechanisms in stellar clusters: comparing external photoevaporation and tidal encounters. , 478(2):2700–2722.

Wright, E. L., Eisenhardt, P. R. M., Mainzer, A. K., Ressler, M. E., Cutri, R. M., Jarrett, T., Kirkpatrick, J. D., Padgett, D., McMillan, R. S., Skrutskie, M., Stanford, S. A., Cohen, M., Walker, R. G., Mather, J. C., Leisawitz, D., Gautier, Thomas N., I., McLean, I., Benford, D., Lonsdale, C. J., Blain, A., Mendez, B., Irace, W. R., Duval, V., Liu, F., Royer, D., Heinrichsen, I., Howard, J., Shannon, M., Kendall, M., Walsh, A. L., Larsen, M., Cardon, J. G., Schick, S., Schwalm, M., Abid, M., Fabinsky, B., Naes, L., and Tsai, C.-W. (2010). The Wide-field Infrared Survey Explorer (WISE): Mission Description and Initial On-orbit Performance. , 140(6):1868–1881.

Yuan, H. B. and Liu, X. W. (2013). Hunting for extremely faint planetary nebulae in the SDSS spectroscopic database. *Monthly Notices of the Royal Astronomical Society*, 436(1):718–739.

Zheng, X., Kouwenhoven, M. B. N., and Wang, L. (2015). The dynamical fate of planetary systems in young star clusters. , 453(3):2759–2770.